Journal of Hydrology 585 (2020) 124826

Contents lists available at ScienceDirect

Journal of Hydrology

journal homepage: www.elsevier.com/locate/jhydrol

Research papers

A review of remote sensing applications for water security: Quantity, quality, and extremes

Ila Chawla[a], L. Karthikeyan[b,c], Ashok K. Mishra[c,*]

[a] Interdisciplinary Centre for Water Research (ICWaR), Indian Institute of Science, Bangalore, India
[b] Centre of Studies in Resources Engineering, IIT Bombay, Powai, Mumbai, India
[c] Department of Civil Engineering, Clemson University, SC, USA

ARTICLE INFO

Keywords:
Water security
Remote sensing
Water quality
Streamflow
Terrestrial water storage
Floods
Droughts
Reservoir monitoring

ABSTRACT

Water resources are critical to the sustainability of life on Earth. With a growing population and climate change, it is imperative to assess the security of these resources. Over the past five decades, satellite remote sensing has become indispensable in understanding the Earth and atmospheric processes. Satellite sensors have the capability of providing data at global scales, which is economical compared to the ground or airborne sensor acquisitions. The science community made significant advances over recent years with the help of satellite remote sensing. In view of these efforts, the current review aims to present a comprehensive review of the role of remote sensing in assessing water security. This review highlights the role of remote sensing applications to assess water quality, quantity, and hydroclimatic extreme events that play an important role in improving water security. Four water quality parameters, namely, chlorophyll-a, turbidity and Total Suspended Solids (TSS), Secchi Disk Depth (SDD), and Colored Dissolved Organic Matter (CDOM), are considered. Under water quantity assessment, we review three aspects, streamflow estimation, terrestrial water storage, and reservoir operations. Remote sensing applications in quantifying floods and droughts extremes are reviewed in this work. We present how satellite sensor information acquired from different spectral bands, including optical, thermal, and microwave ranges, along with gravity field measurements, have contributed towards the applications in the above areas. We also assess the role of physical models, empirical models, and data assimilation strategies, among others, in the above areas. Finally, possible future research pathways needed to address the issues faced by the science community are discussed. This work is the second of the two-part review series, wherein the first part deals with the applications of satellite remote sensing for agriculture management.

1. Introduction

From the available water resources, only about 2.5% of the total amount of water on the Earth constitutes the freshwater, 1.5% of which can be accessed for various biophysical processes. The sustainable management of water resources and ensuring water security is vitally important for creating responsible policies to maintain both; ecological and economic health of a region (Mishra and Singh, 2010). According to the recent UN report (World Population Prospects, 2019), the world population is projected to increase to 9.7 billion by 2050 and 11 billion by 2100. Under a growing population and economy, an increase in water demand and global water scarcity is inevitable (IPCC, 2019). The per capita consumption of water has increased substantially, causing an increase in the extraction and use of freshwater resources from 500 km^3/year to 3800 km^3/year over the last 100 years (Oki and Kanae, 2006). Further, to attain food security, there has been a rapid expansion in the crop land areas, which is causing over-exploitation of groundwater resources for irrigation. The use of fertilizers to enhance crop productivity is affecting water quality, harming marine, and freshwater ecosystems (Vitousek et al., 1997). The increase in industrial water use without proper policies for managing industrial effluents and water recycling, especially in developing countries, (Rajaram and Das, 2008) is raising concerns for maintaining water quality and minimizing water-related health problems (Vörösmarty et al., 2010).

An imbalance between the development and utility of resources is posing a major challenge to manage water resources. The extensive water use has negatively impacted the ecosystem by over-exploiting the groundwater reserves and decreasing the drainage areas of lakes, rivers, and wetlands (Parry et al., 2007). The situation is likely to get worse under the climate change scenario, which is expected to influence the

* Corresponding author.
E-mail address: ashokm@g.clemson.edu (A.K. Mishra).

https://doi.org/10.1016/j.jhydrol.2020.124826

Available online 13 March 2020

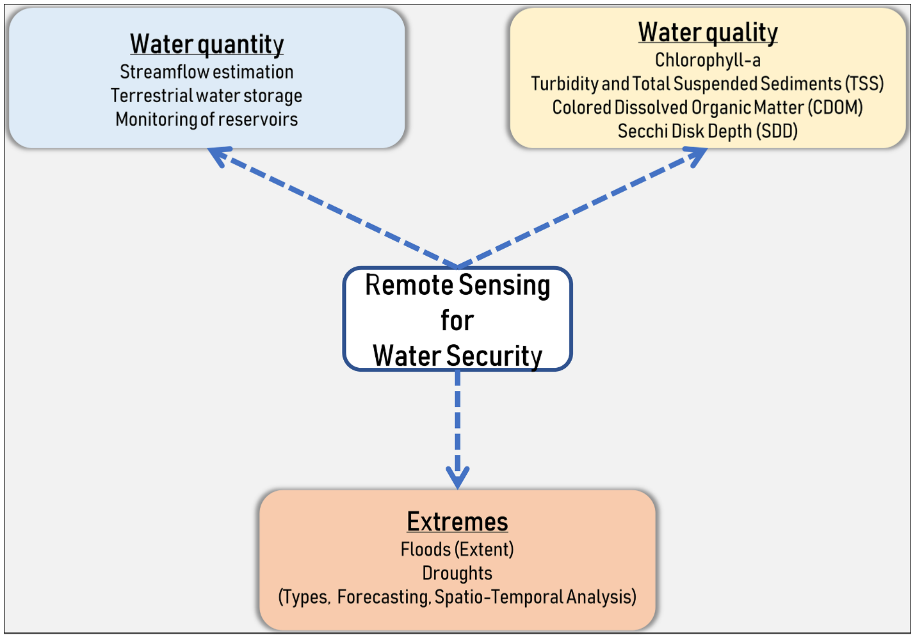

Fig. 1. Schematic diagram of the review of role of remote sensing applications for water security.

freshwater system through an increase in temperature, sea-level rise, rainfall variability, and an increase in extreme events (Parry et al., 2007). According to the IPCC (IPCC, 2019), at 1.5 °C rise in temperature 178 million people from the dryland population are vulnerable to water stress. This number is estimated to increase to 220 and 270 million people with 2 °C and 3 °C rise in temperature, respectively. An increase in the global average surface air temperature during the 20th century (Houghton et al., 2001) is likely to turn some part of snowfall into rainfall and snowmelt season is expected to commence earlier, causing change in the timing and volume of snowmelt generated runoff (Huss and Hock, 2018; Parry et al., 2007). The temperature increase and the associated melting of polar ice are 'very likely' to cause a rise in the sea levels, resulting in the intrusion of saltwater into groundwater aquifers, rendering the groundwater unusable and consequently decreasing the availability of groundwater resources (Oki and Kanae, 2006).

Although there is considerable uncertainty associated with the impact of climate change on the global water cycle (Chawla and Mujumdar, 2017), most of the studies indicate its intensification due to an increase in evaporation and, consequently, precipitation. The intensified hydrologic cycle may result in frequent occurrences of extreme events such as drought, floods, and cyclones, which are likely to cause catastrophic damage. This may have greater detrimental effects in developing countries due to limited resources for mitigation and adaptation strategies (Huntington, 2006). In addition to the anticipated effects of climate change on the water sector (Chawla and Mujumdar, 2015), the increase in water demand, along with lack of effective governance, is adding to the challenge of maintaining water quality and efficient use of water resources (O'Connell, 2017; Sheffield et al., 2018).

1.1. Role of remote sensing in water security

Considering the role of water security in global development, the United Nations has recognized the provision of clean water and sanitation as one of the Sustainable Development Goals (SDGs; SDG 6 in particular). To achieve the SDGs, integrated management of water resources has become the scientific paradigm. The management of the availability of water resources under ongoing global-scale changes requires continuous monitoring of water availability and its vulnerabilities with space and time (Mishra and Coulibaly, 2009). Hydro-meteorological information (e.g., precipitation, streamflow, and soil moisture) plays a vital role to improve water resource management and to quantify the extreme events. However, accurate measurement and monitoring of hydro-meteorologic variables through in situ observations is challenging because of outdated or non-existing socioeconomic data and deteriorating observation network (Mishra and Coulibaly, 2009). Several studies report a global decline in hydrometric stations (Rodda et al., 1993; Shiklomanov et al., 2002; Mishra and Coulibaly, 2009), impeding the ability to monitor the availability of resources, predict droughts, and forecast floods. The in-situ observation stations are non-uniformly distributed and also operate intermittently due to insufficient investment in infrastructure, inadequate institutional framework, lack of government interest, and inability to comprehend the need of long-term records leading to a lack of continuous time series of different hydro-meteorologic variables (Pearson, 1998; Mishra and Coulibaly, 2009; Sheffield et al., 2018). In situ hydro-climate data observed by gauges provides valuable information for water resources management; however, these data have key limitations, for example, lack of spatial coverage and missing data sets in most parts of the globe (except in a few developed countries). Also, the existence of a political situation or transboundary water sharing condition may hinder the procurement of data for several important rivers (Kim et al., 2019).

Due to limitations in ground-based observations, the availability of remote sensing products has served as an important source for researchers, water resources managers, and related stakeholders in their endeavors. Remote sensing is a cost-effective method for viewing large water bodies with high temporal coverage and reasonable accuracy, which is physically not possible through in-situ measurements. The large-scale coverage of areas by the satellite data helps in understanding the evolution of hazards, which is critical for managing resources (van Dijk and Renzullo, 2011). This paper (Part 2 of the two-paper series) provides a review on the applications of remote sensing data for water security. In this regard, three important areas are considered in this review, 1) water quality assessment, 2) water quantity, which includes streamflows, terrestrial water storage, and reservoir monitoring, and 3) extreme events, which include floods and droughts. Fig. 1 presents a detailed schematic diagram of various areas and subtopics selected for review in this paper.

Table 1
List of satellites with optical/thermal sensors and their configurations. Note that the table is not exhaustive. We present only the sensors that are included as a part of this review.

Satellite	Sensor	Duration	Frequency Range (Number of Bands)	Spatial Resolution	Temporal Resolution
Landsat	Multispectral Scanner System (MSS)	1972 – present	500 nm – 1.1 µm (4 for Landsat 1,2,3, 4, and 5)	57 m, or 60 m	18 days, 16 days
	Thematic Mapper (TM) and Enhanced Thematic Mapper (ETM)	1972 – present	450 nm – 2.35 µm; 10.4 – 12.5 µm (7 for Landsat 4, and 5; 8 for Landsat 7)	30 m, 120 m	16 days
Geostationary Operational Environmental Satellite (GOES)	GOES Imager	1975 - present	450 nm – 13.6 µm (16)	1 km; 4 km	–
NIMBUS-7	Coastal Zone Color Scanner (CZCS)	1978 – 1995	433 nm – 12.5 µm (6)	825 m	6 days
Satellite pour l'Observation de la Terre (SPOT)	High Resolution Visible (HRV)	1986–2009	500 nm – 900 nm (4)	20 m	26 days
	High Resolution Visible and Infra-red (HRVIR)	1998 – 2013	500 nm – 1.75 µm (4)	20 m; 10 m	26 days
	Vegetation	1998 – 2015	430 nm – 1.75 µm (4)	1 km	26 days
Indian Remote Sensing (IRS)	Linear Imaging Self-Scanning System I (LISS-I)	1988–2003	450–860 nm (4)	72.5 m	22 days
	Linear Imaging Self-Scanning System II (LISS-II)	1991 – 2003	450–860 nm (4)	36.25 m	22 days
	Linear Imaging Self-Scanning System III (LISS-III)	1995–2010	520 nm – 1.7 µm (5)	70.5 m; 23.5 m; 5.8 m	25 days
Japan Earth Resources Satellite (JERS-1)	Optical Sensor (OPS)	1992 – 1998	520 nm – 2.4 µm (8)	18.3 m; 24.2 m	44 days
OrbView-2	Sea viewing Wide Field Sensor (SeaWiFS)	1997 – 2010	400 nm – 900 nm (8)	1.1 km; 4.5 km	1 day
IKONOS	Multispectral Sensor; Panchromatic Sensor	1999–2015	445 – 900 nm (5)	3.2 m, 0.82 m	3 days
Terra	Advanced Spaceborne Thermal Emission and Reflection Radiometer (ASTER)	1999 – present	520 nm-11.65 µm (14)	15 m, 30 m, 90 m	16 days
Terra, Aqua	Moderate Resolution Imaging Spectroradiometer (MODIS)	2000 – present	400 nm – 14.4 µm (36)	250 m, 500 m, and 1 km	16 days
Earth Observatory-1	Hyperion	2000–2017	390 nm – 2.5 µm (2 2 0)	30 m	16 days
	Advanced Land Imager (ALI)	2001–2017	400 nm – 2.4 µm (10)	10 m; 30 m	16 days
QuickBird	Multispectral Sensor; Panchromatic Sensor	2001–2015	450 – 900 nm	2.62 m, 0.65 m	1 – 3.5 days
ENVISAT	Medium Resolution Imaging Specrometer Instrument (MERIS)	2002 – 2012	390 – 1040 nm (15)	300 m; 1200 m	35 days
Ice, Cloud, and land Elevation Satellite (ICESat)	Geoscience Laser Altimeter System (GLAS)	2003 – 2010	532 nm; 1064 nm (2)	~ 65 m	91 days
	Advanced Topographic Laser Altimeter System (ATLAS)	2018 – present	532 nm (1)	< 17.5 m	91 days
WorldView-1/2/3/4	Panchromatic, multispectral, SWIR sensors	2007 – present	450–800 nm (panchromatic) 400–1040 nm (8; multispectral) 1195–2365 nm (8; SWIR)	0.31 m (panchromatic), 1.24 m (multispectral), 3.7 m (SWIR)	< 1 day
National Oceanic and Atmospheric Administration's (NOAA's) Polar Orbiting Environmental Satellites (POES)	Advanced Very High Resolution Radiometer (AVHRR)	2009 and 2012 – present	580 nm – 12.5 µm (6)	1.1 km; 4 km	1 day
NOAA-20	Visible Infrared Imaging Radiometer Suite (VIIRS)	2011-present	412 nm – 12.01 µm (22)	375 m, 750 m	16 days
Ziyuan 3	Multispectral Camera	2012 – present	450–890 nm (4)	5.8 m	4–5 days
RapidEye	Multi-spectral imager	2008 – present	440–850 nm (5)	6.5 m	daily
Sentinel 2A and 2B	Multi-Spectral Imager (MSI)	2015 and 2017 – present	440 nm – 2.19 µm (12)	60 m, 20 m and 10 m	5 days

Table 2
List of satellites with active microwave sensors and their configurations. Note that the table is not exhaustive. We present only the sensors that are included as a part of this review.

Satellite	Sensor	Duration	Frequency Range (Number of Bands)	Spatial Resolution	Temporal Resolution
Geophysical Satellite (GeoSat)	GeoSat Radar Altimeter (GRA)	1985 – 1990; 1998 – 2008	13.5 GHz (1)	5 km*	17 days
European Remote Sensing satellite (ERS-1/2)	Radar Altimeter	1991 – 2000; 1995 – 2011	13.8 GHz	16–20 km*	35 days
TOPography EXperiment (TOPEX)/ Poseidon	Dual Frequency Radar Altimeter (ALT)	1992 – 2005	5.3 GHz; 13.6 GHz (2)	11.2 (along) × 5.1 (across) km	10 days
JASON	Poseidon-2 (JASON-1); Poseidon-3 (JASON-2); and Poseidon-3B (JASON-3) (Altimeter)	2001 – 2013; 2008–2019; 2016 – present	5.3 GHz; 13.575 GHz (2)	11.2 × 5.1 km	10 days
ENVISAT	Radar Altimeter	2002 – 2012	3.2 GHz; 13.575 GHz	20 km*	35 days; 30 days (from 2010)
Cryosat-2	SAR/Interferometric Radar Altimeter-2 (SIRAL-2)	2010 - present	13.575 GHz (1)	15 km*	369 days (30-day pseudo subcycle)
SAtellite for Argos and ALtiKa (SARAL)	Altika	2013 – present	35.75 GHz (1)	8 km*	35 days
Sentinel 3A and 3B	SAR Radar Altimeter (SRAL)	2016 – present	13.575 GHz; 5.41 GHz (2)	300 m × 1.64 km (SAR C-band); 1.64 km × 1.64 km (Low resolution mode)	27 days
ERS-1/2	Synthetic Aperture Radar (SAR)	1991–2011	5.3 GHz (1)	50 km	2–7 days
Japan Earth Resources Satellite (JERS-1)	L-band SAR	1992 – 1998	1.275 GHz (1)	18 m	44 days
Tropical Rainfall Measurement Mission (TRMM)	Precipitation Radar (PR)	1997–2015	13.796 GHz; 13.802 GHz (2)	0.25°	0.5 days
QuikSCAT	Ku-band scatterometer	1999–2018	13.4 GHz (1)	25 km	1–2 days
Shuttle Radar Topography Mission (SRTM)	Spaceborne Imaging Radar-C (SIR-C); SAR-X	2000	5.3 GHz; 9.6 GHz (2)	30 m; 90 m	–
ENVISAT	Advanced Synthetic Aperture Radar (ASAR)	2002 – 2012	5.3 GHz (1)	30 m	35 days; 30 days (from 2010)
COSMO-SkyMed	SAR 2000	2007 - present	9.60 GHz (1)	1 m (SPOTLIGHT); 5 m (STRIPMAP-HIMAGE); 15 m (STRIPMAP-PINGPONG); 30 m (SCANSAR-WIDEREGION); 100 m (SCANSAR-HUGEREGION)	16 days
MetOp-A/B	Advanced SCATterometer (ASCAT)	2007 – present	5.225 GHz (1)	25 km	1–2 days
RADARSAT-2	Synthetic Aperture Radar (C-band)	2007 – present	5.405 GHz (1)	3–100 m	24 days
TerraSAR-XS	SAR-X	2007 – present	9.65 GHz (1)	1.1 m (SPOTLIGHT); 3.3 m (STRIPMAP); 18.5 m (SCANSAR)	11 days
RISAT-1	C Band Synthetic Aperture Radar (SAR)	2012–2017	5.35 GHz (1)	1 – 50 m	25 days
ALOS-2	Phased Array L-band Synthetic Aperture Radar (PALSAR-2)	2014 – present	1.257 GHz (1)	1 × 3 m (Spotlight mode); 1,6 6 or 10 m (Strip map mode); 60 or 100 m (ScanSAR mode)	14 days
Sentinel 1A and 1B	C-band Synthetic Aperture Radar	2014 and 2016 – present	5.405 GHz	5 m × 5 m (stripmap mode), 5 m × 20 m (interferometric wide swath mode), and 25 m × 100 m (extra-wide swath mode); 5 m × 20 m (wave mode)	12 days
SAtélite Argentino de Observación COn Microondas (SAOCOM-1A)	L-band SAR	2018 – present	1.275 GHz (1)	10–100 m	16 days (expected to be 8 days with lauch of SAOCOM-1B)

* indicates footprint.

Table 3
List of satellites with passive microwave sensors and their configurations. Note that the table is not exhaustive. We present only the sensors that are included as a part of this review.

Satellite	Sensor	Duration	Frequency Range (Number of Bands)	Spatial Resolution	Temporal Resolution
Aqua	Advanced Microwave Scanning Radiometer-Earth Observing System (EOS) (AMSR-E)	2002–2011	6.925 GHz; 10.65 GHz; 18.7 GHz; 23.8 GHz; 36.5 GHz; 89.0 GHz (6)	56 km (6.925 GHz); 38 km (10.65 GHz); 21 km (18.7 GHz); 24 km (23.8 GHz); 12 km (36.5 GHz);5.4 km (89 GHz)	1–2 days
Microwave Imaging Radiometer using Aperture Synthesis (MIRAS)	Soil Moisture Ocean Salinity (SMOS) L-band radiometer	2010 – present	1.4 GHz (1)	< 50 km	2.5–3 days
GCOM-W	Advanced Microwave Scanning Radiometer 2 (AMSR2)	2012 – present	6.93 GHz; 7.3 GHz; 10.65 GHz; 18.7 GHz; 23.8 GHz; 36.5 GHz; 89 GHz	62 × 35 km (6.93 GHz); 62 × 35 km (7.3 GHz); 42 × 24 km (10.65 GHz); 22 × 14 km (18.7 GHz); 19 × 11 km (23.8 GHz); 12 × 7 km (36.5 GHz); 5 × 3 km (89 GHz)	1–2 days
Soil Moisture Active Passive (SMAP)	SMAP L-band radiometer	2015 – present	1.4 GHz (1)	47 × 39 km	1–3 days

Table 4
List of satellites that measure gravity field and their configurations. Note that the table is not exhaustive. We present only the sensors that are included as a part of this review.

Satellite	Sensor	Duration	Frequency Range (Number of Bands)	Spatial Resolution	Temporal Resolution
Gravity Recovery and Climate Experiment (GRACE)	K-Band Ranging (KBR) twin-satellite system	2002 – 2017	24 GHz; 32 GHz	400 km	30 days
GRACE-Follow-On (FO)	K-Band Ranging (KBR) twin-satellite system	2018 – present	24 GHz; 32 GHz	400 km	30 days

2. Overview of remote sensing satellites

An overview of satellite sensors mentioned in this review is highlighted in this section. Table 1 presents a list of optical/thermal sensors, and Tables 2 and 3 present the list of active and passive microwave sensors. In addition to sensors that measure signals in the electromagnetic spectrum, missions such as Gravity Recovery and Climate Experiment (GRACE) and its follow-on (GRACE-Follow-On), measure the gravity field through a pair of satellites, which essentially "look" at each other instead of the Earth surface (Table 4). We also provide the information of operation duration, spatial and temporal resolution of each of the sensors.

3. Remote sensing for assessing water security

3.1. Water quality

The rapid and continuous growth in the population and industries has led to an increase in the point and non-point sources of pollution to water bodies. While point sources can be traced to a single source, non-point sources are diffused in nature and are difficult to track. These polluting sources deteriorate the quality of water and affect unique ecosystems of both inland waters (such as rivers, lakes, and reservoirs) as well as coastal waters, which supports a wide variety of aquatic flora and fauna (Dekker et al., 1995). Therefore, monitoring water quality is crucial to ascertain the sustainability and usability of water resources.

The physical, chemical and biological properties of water determine the quality of water. Traditionally, these properties were quantified through field and laboratory analysis, which can be time-consuming and labor-intensive (Bierman et al., 2011; Glasgow et al., 2004). Also, spatio-temporal characteristics of water properties are influenced by several factors, such as the location of sampling, urbanization, land-use transitions, deforestation, and climate change (temperature change, in particular) (Delpla et al., 2009). So, in-situ surveys over large demographic areas, spanning long durations, may turn out to be infeasible. In this context, satellite and airborne sensors can provide information, which can be used to efficiently monitor certain water quality parameters such as chlorophyll-a, suspended sediments, turbidity, total phosphorus, dissolved organic content, temperature, Secchi disk depth, heavy metal pollution, among others over a large scale. Since the advent of Landsat missions in the 1970s, satellite remote sensing information is being increasingly used to assess water quality parameters (Alparslan et al., 2007; Bhavsar, 1984; Dekker and Peters, 1993).

The spectral characteristics of a clear water surface are significantly different from water mixed with impurities or pollutants. A clear water body absorbs around 97–99% of the incident energy and reflects only 1–3% of incident radiations (Büttner et al., 1987). This proportion alters with the change in the quality of water, with polluted water having higher reflectance. Further, the dominant reflected wavelength changes with change in the constituents of water. Therefore, the presence of different substances in the water body results in unique spectral signatures, which are measured by various optical and thermal sensors mounted on different satellites and airborne platforms. To monitor water quality, a relationship between spectral reflectance and water quality parameters needs to be established (Büttner et al., 1987; Ritchie et al., 2003), wherein the general form of the relationship is given by Eq. (1).

$$Y = A + BX \text{ (or) } Y = AB^X \tag{1}$$

where Y is the spectral reflectance measured by the remote sensors; X is the water quality parameter of interest, and A and B are the empirical factors.

Ritchie et al. (1976) showed that water with low sediment concentration has a maximum reflection at 0.55 μm compared to 0.6 μm by water with high sediment concentration. The ultraviolet radiations (0.25–0.39 μm) get reflected from the water surface and usually contain the information on the presence of oil slicks on water bodies (Seyhan and Dekker, 1986). Within the visible region, due to differences in the absorption and reflection patterns, various water quality parameters such as Chlorophyll-a, suspended sediments, dissolved organic content, among others, can be identified (Büttner et al., 1987). Beyond the visible range, most of the energy is absorbed by the water body. This indicates that sensor selection is critical for monitoring water quality as reflected irradiance depends on the parameter to be examined and its concentration (Ritchie et al., 2003).

Information from Landsat (Alparslan et al., 2007; Brezonik et al., 2005; Brivio et al., 2001; Büttner et al., 1987; Ritchie et al., 1990); MODIS (Binding et al., 2012; Härmä et al., 2001; Lesht et al., 2013; Swain and Sahoo, 2017); OrbView-2 (SeaWiFS) (Gohin et al., 2019; Vos et al., 2003) satellites have often been used to detect quality of water bodies. Recently, Sentinel-2 datasets are also being employed for the study of water quality (Bonansea et al., 2019; Sòria-Perpinyà et al., 2020). Besides, hyperspectral images from sensors such as Hyperion are also increasingly used due to their better ability to detect suspended sediments, dissolved organic matter, and chlorophyll content in water bodies (Hakvoort et al., 2002; Thiemann and Kaufmann, 2002). During recent years, attempts are being made to merge hyperspectral sensor data with multispectral sensor data to map water quality (Gohin et al., 2019; Östlund et al., 2001). The merging of datasets helps in attaining good spectral as well as spatial resolutions, which is necessary to determine the quality of water accurately. For further details regarding different satellite sensors used for obtaining water quality parameters, readers are encouraged to refer to Gholizadeh et al. (2016).

Literature suggests that optical remote sensing is widely used to monitor water quality parameters. To the best of our knowledge, there are limited studies that incorporate other bands of the spectrum, such as microwave frequencies for this purpose (Zhang et al., 2002, 2003a; Zhang et al., 2003b). Hence, we limit this review to satellite optical sensors. In this section, we review the role of satellite remote sensing towards estimating four important water quality parameters, a) Chlorophyll-a, b) Turbidity and Total Suspended Sediments (TSS), c) Secchi Disk Depth (SDD), and d) Colored Dissolved Organic Matter (CDOM).

3.1.1. Chlorophyll-a

Among different water quality parameters, Chlorophyll-a (Chl-a) is one of the most widely examined parameters using remote sensing information. It is a photosynthesis pigment that is responsible for causing green color (reflect green wavelength while absorbing energy from other wavelengths) in plants, algae, and cyanobacteria. Its occurrence in water bodies is linked directly to the presence of algal bloom and, therefore, indicates the extent of eutrophication in water bodies. Nitrogen and phosphorous are the two compounds, sourced from fertilizer runoff and burning fossil fuels, that act as catalysts for the growth of algae and causing eutrophication of water bodies. Although eutrophication is a natural process, nutrient loading increases its rate and accelerate the degradation of water bodies (Li and Li, 2004).

The presence of different Chl-a concentration in water results in spectral reflectance curve with absorption in the blue (~0.4 μm) and red (~0.7 μm) bands, and reflectance in green (~0.5 μm) and near-infrared (~0.8 μm) bands. This property is used by various sensors to retrieve the Chl-a information from water. Although in most of the studies visible range bands from multispectral sensors are used to estimate Chl-a (Brivio et al., 2001; Dekker and Peters, 1993; Ritchie et al., 1990); Dekker and Peters (1993) and Härmä et al. (2001) found that it is challenging to determine Chl-a concentration using multispectral data in water bodies with high suspended sediments. Therefore, narrow bandwidth imageries are necessary to measure Chl-a concentrations. Most of the literature suggests that optimum bandwidth to quantify Chl-a levels is around 675 nm and 700 nm (Gholizadeh et al., 2016). During recent years, merged satellite datasets are also being used to monitor

Table 5
Different satellite datasets used for measuring various water quality parameters.

Water Quality Parameter	Satellite-Sensor	References
Chlorophyll -a (Chl-a)	Landsat	Alparslan et al. (2009); Brezonik et al. (2005); Brivio et al. (2001); Kloiber et al. (2002a); Lathrop and Lillesand (1986); Lillesand et al. (1983); Ritchie et al. (1990); Rundquist et al. (1996); Wang et al. (2006)
	ObrView-2 (SeaWIFS)	Gohin et al. (2019); Kahru and Mitchell (2001); Vos et al. (2003)
	Sentinel-2	Sòria-Perpinyà et al. (2020)
	EO-1 Hyperion	Brando and Dekker (2003); Giardino et al. (2007); Hakvoort et al. (2002); Thiemann and Kaufmann (2002)
	MODIS	Binding et al. (2012); Hunter et al. (2010); Menken et al. (2006); Qi et al. (2014)
	MERIS	Gons et al. (2005); Hunter et al. (2010); Koponen et al. (2002); Le et al. (2013)
	IRS LISS III	Somvanshi et al. (2012)
Total suspended sediments	Landsat	Alparslan et al. (2009); Braga et al. (1993); Bustamante et al. (2009); Cai et al. (2019); Gan et al. (2004); Huovinen et al. (2019); Lathrop (1992); Lathrop and Lillesand (1986); Peterson et al. (2018); Ritchie et al. (1976); Wang et al. (2006)
	Sentinel	Huovinen et al. (2019)
	MODIS	Chen et al. (2007); Feng et al. (2012)
	SPOT HRV	Doxaran et al. (2002); Goodin et al. (1996)
	MERIS	Koponen et al. (2002); Ouillon et al. (2008)
	AVHRR	Aguirre-Gomez (2000); Woodruff et al. (1999)
	MERIS	Juhls et al. (2019)
	EO-1 ALI	Kutser et al. (2005)
	OrbView-2 (SeaWiFS)	D'Sa (2008); Kahru and Mitchell (2001); O'Reilly et al. (1998); Siegel et al. (2002)
	EO-1 Hyperion	Brando and Dekker (2003)
Secchi Disk Depth (SDD)	Landsat	Allee and Johnson (1999); Alparslan et al. (2007); Braga et al. (1993); Chipman et al., 2004; Giardino et al. (2001); Kloiber et al. (2002a); Lathrop (1992); Lathrop and Lillesand (1986); Nelson et al. (2003); Olmanson et al. (2008); Sawaya et al. (2003); Wang et al. (2006); Wu et al. (2008)
	MODIS	Wu et al. (2008)
	MERIS	Koponen et al. (2002)
	AVHRR	Woodruff et al. (1999)
	IKONOS	Sawaya et al. (2003)
	IRS-1A LISS-I	Choubey (1998)
Colored Dissolved Organic Matter (CDOM)	Landsat	Chen et al. (2019); Hirtle and Rencz (2003); Kutser et al. (2005); Li et al. (2018)
	MODIS	Al Shehhi et al. (2019); Carder et al. (1989); Menken et al. (2006)
	IKONOS	Kutser et al. (2005)
	CZCS	Hoge et al. (1995)
	MERIS	Juhls et al. (2019)
	EO-1 ALI	Kutser et al. (2005)
	OrbView-2 (SeaWiFS)	D'Sa (2008); Kahru and Mitchell (2001); O'Reilly et al. (1998); Siegel et al. (2002)
	EO-1 Hyperion	Brando and Dekker (2003)

Chl-a (Gohin et al., 2019). Other relevant literature wherein different sensors are used to determine the Chl-a parameter is summarized in Table 5. Among various satellite sensors, Landsat TM and ETM + are found to be most widely used to assess Chl-a due to high spatio-temporal coverage and free availability.

Eq. (1) presents a general empirical model that relates water quality parameter with spectral bands. Dekker and Peters (1993) noted that Chl-a concentrations could be well monitored if more than one spectral band is used. Subsequently, several studies used band ratios, which can substantially reduce the effect of atmosphere and increase the signal to noise ratio (Bhattf et al., 2010; Dekker and Peters, 1993; Hoogenboom et al., 1998; Kim et al., 2014; Lim and Choi, 2015; Thiemann and Kaufmann, 2002). Harding et al. (1995) developed the following equation (Eq. (2)) to determine Chl-a content empirically using band ratio.

$$log_{10}[Chl - a] = A + B(-log_{10}G) \tag{2}$$

with $G = \frac{(R_2)^2}{R_1 \times R_3}$

where A and B are constants derived from in situ measurements, R_1, R_2 and R_3 are the spectral reflectance at 460 nm, 490 nm and 520 nm, respectively.

In addition, several other empirical algorithms that employ multiple spectral bands have been developed, which include two band algorithm (2BDA) (Dall'Olmo and Gitelson, 2005), three band algorithm (3BDA) (Gitelson et al., 2003; Dall'Olmo and Gitelson, 2005), normalized difference chlorophyll index algorithm (NDCI, Mishra and Mishra, 2012), maximum chlorophyll index (MCI) algorithm (Binding et al., 2013), surface algal bloom index algorithm (SABI) (Alawadi, 2010), fluorescence line height (FLH) algorithm (Zhao et al., 2010), and normalized green-red difference index (NGRDI) (Feng et al., 2015).

The 3BDA is found to be useful in quantifying Chl-a in turbid waters with a wide range of optical complexity (Moses et al., 2009). However, it is based on several assumptions such as (i) absorption by suspended solids beyond 700 nm is same as that of 665–675 nm and can be ignored; (ii) absorption beyond 730 nm is nearly zero; and (iii) backscattering coefficient of Chl-a is spectrally invariant (Mishra and Mishra, 2012). The MCI algorithm was found to work well when Chl-a concentrations range from 10 to 300 mg m^{-3}, it failed in high biomass conditions and with variations in optical properties of water. The NDCI could work well in turbid productive waters and could also be transferred to other geographical locations without adding any significant uncertainties, making it superior to the 2BDA, 3BDA, and MCI. The SABI was found to accurately delineate spatial distributions of algal bloom without getting affected by environmental conditions like aerosol and sun glaze. The NGRDI is noticed to perform reasonable in water bodies with extreme turbidity and can also help in delineating potential eutrophication areas.

Furthermore, attempts are being made to incorporate Empirical Orthogonal Function (EOF) to measure Chl-a levels in surface water (Qi et al., 2014). The EOF approach considers spectral variance of normalized Rayleigh-corrected reflectance data at 469, 555, 645, and 859 nm and relates the observed variance with Chl-a levels. The authors found this method to be useful for Chl-a concentrations ranging from 3 to 100 μg/L. However, the empirical nature of the algorithm, along with limited spectral bands for the aforementioned wavelengths led to significant uncertainties in the results. It highlights the need for further improvement in the remotely sensed data. Besides, one of the prime concerns with all the empirical models is that they require accurate parameterization, which may vary with the optical properties of the water body (Mishra and Mishra, 2012).

3.1.2. Turbidity and Total Suspended Sediments (TSS)

The monitoring of Total Suspended Sediments (TSS) is critical for analyzing river dynamics as it serves as an indicator for water quality and also used in sediment discharge and transport applications (Peterson et al., 2018). The suspended sediments affect water quality by blocking the transmission of light, altering the nutrient concentration, obstructing channels, and reducing dissolved oxygen (He et al., 2017). The presence of suspended particles causes turbidity in the water body. The turbidity of water is directly linked to suspended particles – higher the turbidity, more the concentration of suspended particles. Therefore, the measurement of turbidity is often considered as a proxy for sediment concentration in the water body (Rügner et al., 2013; Wass et al., 1997). Further, TSS and turbidity can also be used to indirectly monitor heavy metal concentration in water bodies (Nasrabadi et al., 2016).

The presence of TSS and consequently turbidity in water bodies increases reflectance from red and NIR regions of the electromagnetic spectrum (Dogliotti et al., 2015; Feng et al., 2012; Ritchie et al., 1976; Ritchie and Cooper, 1988). This property is used to monitor turbidity and TSS parameters. Different sensors are used to measure different levels of turbidity in the water body. The red bands of Landsat TM (630–690 nm) and SPOT (610–680 nm) sensors, and MODIS 645 nm band are found to be useful in monitoring low turbidity levels ranging from 0.9 to 15 NTU (Nephelometric Turbidity Unit) (Bustamante et al., 2009; Chen et al., 2007; Goodin et al., 1996). MERIS dataset at 681 nm can measure turbidity in the range 1 – 25 NTU (Ouillon et al., 2008). Apart from single bands, different band ratios are also used to quantify TSS and turbidity. The ratio of green (560 nm) and blue (413 nm) bands from the MERIS dataset is used to map turbidity in the range of 1–60 NTU (Potes et al., 2012). The ratio of red (630–690 nm) and blue (400–500 nm) bands from the Landsat dataset is used to monitor high turbidity concentrations ranging from 2 to 997 NTU (Liversedge, 2007). Ritchie et al. (1976) found out that, in general, the optimum wavelength to quantify suspended material in water bodies is 700–800 nm.

Several empirical models have been developed to relate spectral reflectance with the concentration of suspended material in water bodies. Schiebe et al. (1992) and Harrington et al. (1992) developed an empirical model given by Eq. (3).

$$R_i = B_i[1 - e^{(c/S_i)}] \tag{3}$$

where R_i is the reflectance corresponding to band i, c is the concentration of TSS, B_i represents the reflectance saturation of band i at high TSS level, and S_i gives the TSS concentration at 63% saturation reflectance of band i.B_i and S_i are coefficients that are statistically determined. Due to a lack of generality in empirical models, analytical models based on Radiation Transfer Equations (RTEs) are developed. For instance, Volpe et al. (2011) developed Eqs. (4) and (5) using RTE to retrieve TSS concentration from the reflectance measured by the sensors.

$$R = \frac{0.5r}{1 - 1.5r} \tag{4}$$

$$r = r^{dp}\left[1 - e^{-(K_d + K_u^C)H}\right] + \frac{\rho_b}{\Pi}e^{-(K_d + K_u^B)H} \tag{5}$$

where, R is water surface reflectance and is related to other controlling factors such as r which is subsurface reflectance; r^{dp} is reflectance for optically deep water; K_d is vertically averaged diffuse attenuation coefficient for downwelling irradiance; K_u^C is vertically averaged diffuse attenuation coefficient for upwelling radiance from water-column scattering; K_u^B is vertically averaged diffuse attenuation coefficient for upwelling radiance from water-column scattering; ρ_b represent the bottom albedo; H is the water depth; and $u = b/(a + b)$, where b is backscattering coefficient and a represents the absorption coefficient. The RTE based model helps in addressing the issues commonly faced in the empirical model such as (i) interference from the reflection from the bottom of the water body; (ii) accurately knowing the optical properties of water bodies; and (iii) uncertainties in retrieved estimates (Volpe et al., 2011). Table 5 summarizes the widely used satellite sensors for quantifying turbidity and TSS levels in water bodies. From the literature survey, it is noticed that Landsat TM is the most commonly used dataset for estimating turbidity and TSS.

3.1.3. Secchi Disk Depth (SDD)

Clarity of water body is considered generally as a visual measure for water quality (Li and Li, 2004). Secchi Disk Depth (SDD) is a measure for the water clarity index (Davies-Colley and Smith, 2001. In this method, a black-and-white disk called Secchi disk, invented by an Italian astronomer Pietro Angelo Secchi in 1865 (having a diameter ranging from 30 to 100 cm, marked with graduated lines), is inserted into the water body and noted to the point of disappearance (Davies-Colley and Smith, 2001). The depth of disappearance is known as SDD and is inversely related to turbidity and TSS concentration in water bodies. The SDD measurement is based on light attenuation principle, wherein Tyler (1968) and Preisendorfer (1986) found that SDD is inversely related to the sum of two light attenuation coefficients, c, and K as indicated in Eq. (6)

$$SDD = \frac{G}{(c + K)} \tag{6}$$

where G depends on visible reflectance from the Secchi disk, and it varies within the range of 6–9 (Tyler, 1968).

Although SDD is an inexpensive way of monitoring water clarity, it is highly subjective and depends on the visual accuracy of the observer. SDD is also affected by tides on the water surface (Heddam, 2016). Since SDD is related to turbidity and TSS concentration in the water body, several empirical models have been developed to associate these two parameters. Some of the relationships are listed in Eq. (7)–(9). (Brezonik, 1978) (Gikas et al., 2009) (USGS, 2014)

$$log(SDD) = 0.48 -- 0.72\ log(tur) \tag{7}$$

$$log(SDD) = 2.11\ log\ (TSS)^{-0.16} \tag{8}$$

$$SDD = 11.123\ (tur)^{-0.637} \tag{9}$$

where, tur indicates turbidity in Formazin Nephelometric Unit (FNU); and TSS represents Total Suspended Sediments in the water body.

Apart from empirical relationships, spectral bands from different satellite data are also used directly to measure SDD. Due to easy monitoring of turbidity and TSS levels in the visible range, red and blue bands are found to be useful in mapping SDD. Hellweger et al. (2004) used the red band, whereas Lathrop and Lillesand (1986) used the green band from the Landsat TM to determine SDD. Ekercin (2007) found blue, green, and red bands of the IKONOS to explain 98.93% of the variance in SDD. According to Allee and Johnson (1999), the Landsat TM red band is most useful in determining the SDD. Choubey (1998) demonstrated the use of spectral bands of IRS-1A LISS-I satellite data in determining SDD in the Tawa reservoir, Narmada basin, India. They inferred that concentration and grain size of suspended solids are the main factors that influence SDD. Wu et al. (2008) developed a relationship between SDD and spectral reflectance from Landsat TM and MODIS datasets, as indicated in Eqs. (10) and (11) respectively.

$$ln(SDD) = 1.133 - 10.533(Landsat\ TM^{blue}) - 13.805(Landsat\ TM^{red}) \tag{10}$$

$$ln(SDD) = 0.474 + 15.24(MODIS^{blue}) - 21.130\,(MODIS^{red}) \tag{11}$$

In addition to single bands, the ratio between different spectral bands is found to be useful in computing SDD in highly turbid water bodies with low SDD (Lathrop, 1992). Giardino et al. (2001) found the ratio between blue and green Landsat TM bands to be suitable in estimating SDD. Studies found the ratio of blue and red Landsat TM bands, as indicated in the general form in Eq. (12), to be efficient in mapping water clarity in a lake (Kloiber et al., 2002b; Sawaya et al., 2003; Chipman et al., 2004). Similarly, Nelson et al. (2003) found blue to red band ratio from Landsat TM to be useful in estimating SDD across 93 lakes in Michigan, USA. While the above works used Landsat data, Sawaya et al. (2003) noticed the ratio of IKONOS blue and red bands to be better than Landsat data for mapping SDD (Eq. (12)).

$$ln(SDD) = a(Landsat^{blue}/Landsat^{red}) + b(Landsat^{blue}) + c \tag{12}$$

Furthermore, several works found strong correlation between Chl-a and SDD (Al Shehhi et al., 2019; Allee and Johnson, 1999; Brezonik, 1978; Carlson, 1977; Dekker and Peters, 1993; Doña et al., 2015; Doña et al., 2014; Gikas et al., 2009; Gikas et al., 2006; Stadelmann et al., 2001). Different satellite datasets used to measure SDD are enlisted in Table 5. Among all the datasets, Landsat TM, due to its low-cost, and high spatial and temporal coverage is most frequently used in estimating SDD.

3.1.4. Colored dissolved organic Matter (CDOM)

Colored Dissolved Organic Matter (CDOM) also referred to as aquatic humus, limnohumic acid, gelbstoff, or gilvin, is composed of macromolecules with aromatic, carboxylic, fulvic, and humic acids, derived from decomposition of plant material in soils and wetlands, bacterial activity, algal growth, and sediment loading (Brezonik et al., 2005; Carder et al., 1989; Twardowski and Donaghay, 2001). These compounds impart yellow-brown color to the water body, when present in high concentrations (Branco and Kremer, 2005; Gholizadeh et al., 2016). An increase in CDOM loading affects the physical, chemical, and biological properties of water bodies. Higher CDOM levels cause attenuation to the penetration of light into water bodies and also support the growth of phytoplankton, making water bodies more eutrophic (Stedmon et al., 2011). Therefore, the presence of CDOM influences the structure and functioning of the riverine ecosystem (Kutser et al., 2005).

CDOM is found to be strongly correlated to other water quality parameters such as Chl-a, TSS and turbidity levels (Brezonik et al., 2005); therefore, visible spectral bands are found to be relevant in monitoring CDOM concentration in water bodies. Further, the presence of CDOM is noticed to cause absorption in the ultraviolet range and blue-green bands (Chen et al., 2004; Green and Blough, 1994). Brezonik et al. (2005) found that maximum energy absorbance occurs in 440 nm band due to the presence of CDOM, which coincides with the Chl-a absorption band (Carder et al., 1989). Therefore, it becomes extremely difficult to segregate CDOM levels from Chl-a concentration.

CDOM level is usually obtained by determining the wavelength absorption coefficient using different datasets. In this regard, several analytical models have been developed. Hoge et al. (1995) developed a two-band radiance model inversion technique to demonstrate the CDOM absorption coefficient using the coastal zone color scanner (CZCS) spectral bands. However, the accuracy of the method depends on the presence of chlorophyll in the water body. Hirtle and Rencz (2003) found a strong correlation between dissolved organic matter and Landsat TM blue and green bands for the Kejimkujik National Park lake. Brezonik et al. (2005) used the Landsat TM data and identified that the presence of CDOM decreases brightness in blue and green bands. Kutser et al. (2005) used both Landsat and IKONOS datasets to determine the absorption coefficient in boreal lakes to monitor CDOM levels. The authors found that in comparison to 8-bit Landsat data, 11-bit IKONOS data is more suitable for estimating the amount of CDOM in boreal lakes due to higher digital resolution. They further noticed that the ratio of 565 nm and 660 nm bands from the16-bit Advanced land Imager (ALI) data is best in estimating CDOM.

Due to difficulty in retrieving CDOM concentrations in the presence of suspended solids and chlorophyll content, the use of hyperspectral remote sensing datasets is gaining importance in determining CDOM levels. Menken et al. (2006) identified that the ratio of 670 nm to 571 nm MODIS bands could best estimate CDOM levels. Brando and Dekker (2003) developed a matrix inversion technique to retrieve CDOM concentrations using the EO-1 Hyperion hyperspectral dataset, which was noted to show sufficient sensitivity to detect concentrations of CDOM, Chl-a, and TSS in complex waters. Zhu et al. (2011) proposed a method for inversion of hyperspectral remote sensing to determine the absorption coefficient for CDOM. Inversion algorithms, in general, are found to be efficient in estimating CDOM over a large spatio-temporal scale. Karaska et al. (2004) used the AVIRIS dataset to monitor dissolved organic content along with other water quality parameters in the Neuse River, North Carolina. Tehrani et al. (2013) used three datasets – SeaWiFS, MODIS, and MERIS to estimate CDOM concentrations and found that the ratio of 510 nm and 560 nm bands from MERIS dataset gives the most accurate results. Recently, Juhls et al. (2019) used the MERIS dataset to determine the absorption coefficient of CDOM in the Arctic shelf region. The proposed retrieval algorithm was found to perform well in extreme-absorbing and high-scattering waters with high optical complexity that cover the fluvial–marine transition. The other datasets that are used in CDOM measurements are summarized in Table 5.

3.2. Surface and sub-surface water resources

3.2.1. Streamflow estimation

Streamflow or discharge in the river is a dominant process of the hydrologic cycle by which water from the land surface is transported to the oceans. River discharge is the volume of water flowing through the river cross-section per unit of time and is expressed generally as cubic meter per second or cubic feet per second. The measurement of river discharge provides information on water availability and is, therefore, necessary for water resource management and managing flood hazards (Mishra and Coulibaly, 2009; Vörösmarty et al., 2010). Despite being a critical component for understanding surface water balance, river discharges are understood poorly due to limited in-situ networks (Shiklomanov et al., 2002; Mishra and Coulibaly, 2009). Traditionally, the in-situ measurement of discharge involves the use of an already established stage-discharge relationship or rating curve to estimate discharge corresponding to the stream stage or water level height recorded by stream gauges. The in-situ discharge measurement has several limitations, such as stream gauges are located on a few large-sized rivers and are not spatially distributed (Tang et al., 2009). Most of the globally significant rivers are sparsely gauged (Alsdorf et al., 2003).

Further, stream gauges are difficult to install in complex topography regions. Also, there is a global decrease in the number of stream gauges due to a reduction in government funds for monitoring of stream gauges (Shiklomanov et al., 2002; Mishra and Coulibaly, 2009). The existence of a political situation or transboundary water sharing condition may further hinder the procurement of discharge data for several important rivers (Kim et al., 2019). The measurement of water level by stream gauge is based on the assumption that runoff generated upstream of the catchment flows to a single downstream outlet. This assumption might not hold in basins, which are dominated by wetlands and floodplains, where water from upstream reaches is diffused and then reach the channel (Alsdorf and Lettenmaier, 2003). Also, braided rivers, characterized by several intertwined channels, which keeps on changing the shapes, pose an additional challenge for discharge measurement (Alsdorf and Lettenmaier, 2003).

Satellite remote sensing can circumvent these issues while estimating discharge and water storage (Alsdorf et al., 2003; Alsdorf and Lettenmaier, 2003). Remote sensing datasets have the potential of providing frequent global coverage of discharge estimates, which may offer an opportunity to improve the global streamflow network. However, streamflow discharge cannot be measured directly by satellite sensors. Therefore, other hydraulic variables, such as water level height, velocity, river cross-section area, river width, and surface water slope, among others, are also measured by sensors. The accuracy of discharge measurement depends on the efficiency with which the aforementioned hydraulic variables are estimated by remotely sensed data (Kim et al., 2019). We find from the literature that a substantial amount of work is carried out using the altimeter datasets. Further, there is a progression in the way altimeter datasets are used to estimate discharge. Therefore, to keep the review concise, we focus on scientific developments in streamflow estimation using the altimetric data.

Radar altimeters are demonstrated to be useful in estimating water level variations in inaccessible areas (Leon et al., 2006). The use of altimetry came into limelight with 1969 NASA's Skylab S-193 radar altimeter experiment (Brown, 1977). Altimeters measure the time taken by the nadir-directed radar pulse to cover a round trip from satellite to water surface and use it to determine the distance from satellite to water surface. The water level is determined by computing differences in the satellite's position with respect to the reference ellipsoid and distance from the satellite to the water surface (Tang et al., 2009). The general equation to measure the height of the water surface from the satellite is given by Eq. (13).

$$H = h - R + corr \tag{13}$$

where, H is the water surface height; h is the height of satellite orbit; R is the altimeter range measurement; and $corr$ represents the various corrections pertaining to Tropospheric Correction (TC, both dry and wet), Ionospheric Correction (IC), and Tidal correction (T) that need to be applied (Eq. (14)).

$$corr = TC + IC + T \tag{14}$$

Radar altimetry was initially intended to monitor sea surface height variations due to its large footprint. With the launch of Geosat (1985–1990), TOPEX/POSEIDON (1992–2005), ERS-1 (1991–2000), ERS-2 (1995–2011), Geosat Follow On (GFO, 1998–2008), Jason-1 (2001–2013), Jason-2 (2008–2016), ENVIronmental SATellite, ENVISAT (2002–2012), Jason-3 (2016-present), Sentinel-3(2016-present), and Saral/ALtika (2013-present) satellites, usage of altimeter was extended to inland waters (Berry et al., 2005; Birkett 1995a). Together, available global altimetry datasets provide approximately three-decade-long information on water levels of large lakes and global rivers. This information finds applications in the areas of predictions in ungauged basins, climate change detection, monitoring river water availability, and executing hydrologic models.

3.2.1.1. Using altimeters. Some of the pioneering works by Birkett (1994) and Mason et al. (1994) involve the use of radar altimetry for mapping changes in lake levels. Mason et al. (1994) used ESA's ERS-1 radar altimeter along with an infra-red radiometer, ATSR, to monitor volumes of lakes. Morris and Gill (1994) successfully demonstrated the use of Geosat altimetry data to monitor variations in the water level of five Great Lakes of the United States and Lake St. Clair. Birkett (1995a) assessed the potential of TOPEX/Poseidon (T/P) to map global lake levels. Apart from great lakes, altimeter data is often used to measure water levels in large global rivers. In one of the initial works, Koblinsky et al. (1993) demonstrated the ability of Geosat altimeter data to estimate the Amazon river level or stage at four locations. They concluded that the Geosat altimeter based water level estimates are prone to errors, which may be overcome by other missions such as ERS-1 and T/P. Birkett (1995b) monitored the Caspian Sea, the Sudd wetlands, and the Amazon river using the T/P dataset and noticed that seasonal and annual trends could be observed. However, the accuracy of the estimates was unknown, which make the results unreliable. From Geosat to ERS-1 and T/P, there is a reduction in the satellite orbital errors, making radar altimetry a routine method to monitor inland water surfaces (Smith, 1997).

Birkett (1998) identified that the T/P data could successfully monitor rivers with a width greater than 1 km. Birkett (2000) used the T/P data in conjugation with near-infrared imagery from the AVHRR dataset to obtain levels of rivers merging with Lake Chad and also determine permanent and seasonal lake levels. Coe and Birkett (2004) extended this work to obtain mean monthly discharge estimates downstream of Lake Chad. Leon et al. (2006) used T/P and ENVISAT datasets to determine stage-discharge relationships between satellite-derived water level and river discharge at 21 virtual stations in the upper Negro basin, a sub-basin of Amazon River basin, from its source at Columbia and Venezuela borders to Manaus in Brazil. Birkett et al. (2002) evaluated the T/P data for all the major rivers and tributaries in the Amazon River basin. They successfully demonstrated that the altimeter data could be used to obtain water level information at ~10 days interval for rivers with a width of ~1 km. The authors further suggested that the inclusion of GRACE and JERS-1 datasets to the existing T/P dataset may provide more accurate variability in water levels. Da Silva et al. (2010) compared the performance of ERS-2 and ENVISAT for estimating water levels in the Amazon basin and found the latter to perform better. Sulistioadi et al. (2015) demonstrated the use of ENVISAT for small (4–200 m width) and medium (200–800 m width) rivers. Tarpanelli et al. (2014) combined velocity information from the MODIS dataset with water level data obtained from the ENVISAT altimeter to estimate discharge for the Po River, Italy. They found that the coupled dataset compares reasonably well with the in-situ data.

CryoSat-2 satellite was launched with the prime objective of monitoring the cryosphere. However, it has been used to map inland waters and is shown to have the potential to supplement the observations from ENVISAT and Jason-1 (Dibarboure et al., 2012). Villadsen et al. (2015) evaluated the performance of CryoSat-2 to monitor river levels in Ganges and Brahmaputra river basins. The authors found that despite a large revisit time of 369 days, the dataset could represent peak flows during summer due to monsoon and melting of snow in the Himalayas. Schneider et al. (2018) found accurate estimates, with an average error of 0.38 m, for water level observations from the CryoSat-2 data for the Po River, Italy, against the in-situ data.

Jason-2 mission, also known as the ocean surface topography mission (OSTM), was launched as a continuation to the T/P mission to measure the surface topography of oceans and continental surface waters (Lambin et al., 2010). Jason-2 was found to perform better than Jason-1 and T/P missions while monitoring lakes and reservoir systems (Birkett and Beckley, 2010). Kuo and Kao (2011) processed the Jason-2 altimeter data using waveform retracking and water detection algorithms to estimate the surface height of the Bajhang River in Taiwan having seasonal width ranging from 100 m to 1 km. Through this work, the use of altimeter data for monitoring small rivers with varying widths was successfully demonstrated. Jason-2 data was used successfully to estimate instantaneous discharge (Papa et al., 2012), simulate flood events (Jarihani et al., 2013), and also for flood forecasting (Chang et al., 2019; Hossain et al., 2014) purposes. Further, the use of Jason-2 and Jason-3 altimeter datasets along with ancillary data of river width and the course are reported to improve river water level estimates. Biswas et al. (2019) combined the Landsat and SAR information with Jason-3 altimeter and applied an extent-based approach in two methods, (i) river mask based K-means clustering, and (ii) K-means clustering embedded with river mask to improve the satellite altimeter-derived river heights.

Saral/AltiKa mission is the only altimeter that works with a high-frequency microwave band of Ka (36.5 GHz), which results in an effective footprint of 1.3 km. Saral is designated to fill the gap between the ENVISAT and Sentinel-3 missions (Kumar et al., 2017). Since it operates on a high frequency, the signal was initially expected to suffer from higher attenuation. However, this shortcoming was utilized to detect heavy rainfall and flood wave conditions (Roy et al., 2015). Further, the potential of the Saral altimeter to monitor inland waters (Kumar et al., 2015), which include braided rivers, was successfully demonstrated (Dubey et al., 2015). Furthermore, Gupta et al. (2015) converted water levels retrieved from the SARAL/AltiKa into discharge for the Tapi river in India and used it to set up the HEC-RAS hydraulic model for flood inundation modeling. For further applications related to the SARAL/AltiKa mission, readers may refer to Kumar et al. (2017).

The Sentinel-3 is a recently launched satellite mission under the European Commission's Copernicus program. The mission comprises of four satellites, amongst which the two satellites – Satellites A and B were launched in 2016 and 2018, respectively. The Sentinel 3 satellites are equipped with dual-frequency SAR altimeter (SRAL), which is similar to the CryoSat altimeter with advancements. Although the primary purpose of the Sentinel-3 mission is to measure sea-surface topography and thickness of sea-ice, data can also be used to measure the height of rivers and lakes. Further details on the Sentinel-3 mission can be obtained from Donlon et al. (2012). The initial observations from the Sentinel-3 mission are found to be encouraging for water level and discharge monitoring (Bogning et al., 2018). Tarpanelli et al. (2019) demonstrated the potential of Sentinel-3 satellite with three on-board sensors to estimate river discharge.

The direct use of altimeter data for water level and consequently, river discharge is affected by low temporal resolution varying from 10 to 35 days and a large footprint of the data. Therefore, several works in recent years have combined the radar altimeter data with in-situ measurements in a data assimilation framework. Through data assimilation, different satellite products can be merged with the hydrologic/hydraulic model to estimate river discharge, while taking into account both data and model errors (McLaughlin, 1995). Neal et al. (2009) showed that discharge estimates in ungauged basins could be improved by assimilating combined ENVISAT SAR and LiDAR-derived DTM datasets into a coupled hydrologic and hydrodynamic model. Michailovsky et al. (2013) assimilated the ENVISAT data into a river routing model to obtain discharge along the main channel of the Brahmaputra River. Similar assimilation studies were carried out by Emery et al. (2017) and Paiva et al. (2013).

3.2.1.2. Using empirical equations and rating curve. Apart from water levels heights, discharge can also be estimated using other hydraulic variables such as water-surface area, channel slope, average channel width, and velocity of rivers. This information can be obtained from existing remote sensing datasets and used as an input in general hydraulic equations (Bjerklie et al., 2003). For further details, readers may refer to Bjerklie et al. (2003). There have been several works wherein the river stage, and consequently, discharge is indirectly estimated by correlating inundated area with ground measurements of stage or discharge. Smith et al. (1995) used the ERS-1 dataset to develop an area/discharge rating curve for a braided glacial river in British Columbia, Canada. Smith et al. (1996) further extended this work to estimate discharge in ungauged braided rivers. Although individual remote sensing datasets have been used to obtain information of flood inundation and discharge, Frappart et al. (2005) used the combined information from SAR, JERS-1, and T/P datasets to estimate both flood extent and water levels in the Negro River of the Amazon basin to determine the water volume stored in the floodplains. However, they observed that depending on the way floods inundate the area geographically; there can be very low to no difference in the flood plain and river level, making the measurements erroneous. Therefore, to overcome this problem, a combination of several radar altimeters may be useful. Frappart et al. (2006) extended this work and used altimetry data from ERS-2, ENVISAT, and T/P satellites to develop water level time series for the lower Mekong river basin and observed strong seasonality signals in various rivers in the catchment.

Furthermore, Xu et al. (2004) used the QuickBird-2 satellite data at a high spatial resolution of 0.61 m to estimate water-surface width and developed relationships between water-surface width and river width – stage and stage-discharge rating curves. The rating curves were used to estimate discharge in the Yangtze River, China. Similar work was carried out by Zhang et al. (2004) to determine river discharge in a non-trapezoidal open channel. Smith and Pavelsky (2008) used the MODIS data to determine channel geometry parameters to understand discharge and flow conveyance in inaccessible river systems. Birkinshaw et al. (2014) used the altimeter data from ERS-2 and ENVISAT to estimate river stage information. They combined the altimeter data with channel slope information and river channel width obtained from the Landsat to estimate discharge in the ungauged locations of Mekong and Ob rivers. Sichangi et al. (2016) combined altimetry data from several altimeter missions to improve the temporal resolution of the water level data. They further used this combined data with the MODIS data and DEM to obtain discharge estimates based on stage and both stage and width. The authors found that using both stage and width can significantly improve river discharge estimates.

3.2.1.3. Surface Water Ocean Topography (SWOT) mission. The success of altimeter data in mapping discharge is noted to depend on first, the accuracy of water level change estimates; second, frequency of obtaining water level estimates; and third, conversion of water level data to discharge estimates (Koblinsky et al., 1993). Besides, most of the studies reported earlier are for individual river reaches, and also depend on in-situ data based on which relationship between different variables is developed. Therefore, there is still a need for global monitoring of rivers. Several of the limitations associated with the existing radar altimetry are expected to be resolved by the planned Surface Water Ocean Topography (SWOT) mission (Alsdorf and Lettenmaier, 2003). The SWOT mission is designed to provide consistent and coherent information about river discharge and storage, which will improve the understanding of inaccessible and ungauged rivers (Biancamaria et al., 2016). The mission aims at measuring water surface elevation, top width, and free-surface slope enabling discharge estimation for rivers with a width greater than 50 m (Durand et al., 2016). Assimilating this information into the hydrodynamic models will allow extraction of information such as bathymetry, which is not directly observable, and may further assist in the estimation of river discharge (Andreadis et al., 2007). Pavelsky et al. (2014) explored the potential of SWOT mission to monitor global rivers and noted that the mission would significantly improve our hydrological database by updating the Global Runoff Data Centre (GRDC) observation network.

Several initial exploratory studies based on synthetic data have been conducted, which suggest that the SWOT measurements could allow accurate estimates of river discharge for many rivers without in situ calibration. Andreadis et al. (2007) assimilated water surface elevation information from the synthetic SWOT experiment to estimate river flow depth and discharge. Durand et al. (2008) estimated bathymetric depth and slope from water surface elevation measurements obtained from the synthetic SWOT experiments and assimilated into the LISFLOOD-FP model to estimate discharge. Further, uncertainty from river channel bathymetry, which is the main source of error in discharge estimates, is also quantified. Biancamaria et al. (2011) assimilated the synthetic SWOT observations corresponding to the Ob River to estimate changes in water depths, assuming river bathymetry, and quantified the errors due to uncertainties in atmospheric forcing fields and SWOT orbits. They found that the assimilation scheme at a nominal orbit of the mission has the least error in estimating river water depth. Most of the studies above assumed river bathymetry and neglected the associated errors. Yoon et al. (2012) assimilated water surface elevation information into the LISFLOOD-FP model to demonstrate river bathymetry estimation for obtaining river discharge from the SWOT mission for the Ohio river basin. Through the assimilation process, discharge and bathymetry errors were accurately modeled, and it is noticed that errors in bathymetry measurement can have a significant influence on river discharge estimates. Similar attempts are made over the recent years that assimilate synthetic SWOT observation into hydrodynamic models to improve discharge estimates (Andreadis and Schumann, 2014; Pedinotti et al. (2014); Munier et al. (2015); Domeneghetti et al., 2018)

Apart from data assimilation techniques, there are significant works that focused on the development of algorithms to estimate discharge using various hydraulic variables from the SWOT mission. Bjerklie (2007) developed an algorithm based on Manning's equation that uses variables such as channel width, channel slope, and meander length to estimate velocity and discharge of rivers. Gleason and Smith (2014) developed at-many-stations hydraulic geometry (AMHG) algorithm to reduce the number of parameters required to estimate river discharge using multiple satellite images. Durand et al. (2014) developed an algorithm based on the diffusive approximation of shallow water equations to estimate river bathymetry, roughness coefficient, and discharge using surface elevation and slope information. Garambois and Monnier (2015) proposed inverse models based on the Saint-Venant equations to invert effective low flow bathymetry and roughness coefficient to estimate discharge. Durand et al. (2016) presented an intercomparison of five discharge algorithms for 19 rivers with varying hydraulic and geomorphological conditions and suggested that incorporating ancillary data corresponding to elevation and bathymetry, and a combination of algorithms may improve discharge estimates. Although the initial results are encouraging, there is still scope for improvement in the algorithms to obtain accurate discharge estimates.

3.2.2. Terrestrial water storage

The Terrestrial Water Storage (TWS) accounts for all the water available above and below the surface of the Earth and forms an important component of the hydrologic cycle. However, it is difficult to measure TWS at a regional or global scale (Lettenmaier and Famiglietti, 2006). In this regard, the Gravity Recovery and Climate Experiment (GRACE) twin satellite mission, launched in March 2002, proves to be advantageous. The GRACE mission was primarily aimed at mapping temporal variability in Earth's gravitation field at 400 to 40,000 km spatial resolution and 30 days interval (Tapley et al., 2004b). GRACE has shown promising results in inferring trends in surface water mass anomalies (Crowley et al., 2006; Schmidt et al., 2006; Tapley et al., 2004a; Wahr et al., 2004). Changes in the TWS (ΔTWS) are estimated from the GRACE data using Eq. (15) and (16) (Frappart and Ramillien, 2018; Kuss et al., 2012):

$$\Delta TWS = \Delta SWS + \Delta SMS + \Delta SPS + \Delta GWS \tag{15}$$

wherein,

$$\Delta TWS = TWS_{GRACE}(t_2) - TWS_{GRACE}(t_1) \tag{16}$$

$TWS_{GRACE}(t_1)$ and $TWS_{GRACE}(t_2)$ indicate the total water storage obtained from the GRACE data at time 1 and time 2 respectively. Difference between $TWS_{GRACE}(t_2)$ and $TWS_{GRACE}(t_1)$ gives the TWS anomaly, as shown in Eq. (16). ΔSWS is the surface water storage anomaly, ΔSMS is soil moisture storage anomaly, ΔSPS is snowpack storage anomaly, and ΔGWS is groundwater storage anomaly. To determine ΔGWS, the Eq. (15) can be rewritten as Eq. (17).

$$\Delta GWS = \Delta TWS - (\Delta SWS + \Delta SMS + \Delta SPS) \tag{17}$$

wherein, ΔTWS can be obtained from the GRACE data (Eq. (16)) and the remaining variables can be obtained from other remote sensing sources or hydrologic model outputs.

Initial works demonstrated the use of GRACE data in monitoring groundwater storage changes (Rodell and Famiglietti, 2002; Rodell et al., 2007; Rodell et al., 2009). Crowley et al. (2006) showed the capability of GRACE data in estimating TWS for the Congo basin during 2002–2006. Syed et al. (2008) carried out a detailed analysis to show the use of GRACE data in understanding spatio-temporal variability in TWS changes at the continental scale. The GRACE data is also found to be useful in monitoring groundwater changes in groundwater-dependent irrigated areas (Famiglietti et al., 2011; Rodell et al., 2009; Tiwari et al., 2009) and groundwater depletion (Feng et al., 2013).

Apart from direct TWS measurements, the GRACE data is also assimilated into land surface models to improve simulations of hydrologic fluxes and water storage (Eicker et al., 2014; Khaki et al., 2018a; Khaki et al., 2018b; Li et al., 2019; Li et al., 2012; Tian et al., 2017; Zaitchik et al., 2008). GRACE data is also used in combination with other datasets to estimate floodplain storage (Alsdorf et al., 2010; Reager and Famiglietti, 2009), segregating TWS into surface water storage and land water storage (Forootan et al., 2014), terrestrial freshwater discharge (Li et al., 2016; Syed et al., 2009; Syed et al., 2010), and soil moisture and shallow groundwater estimation (Girotto et al., 2019). Since the GRACE data is available at coarse resolution, it is incompatible with other hydrological datasets. Landerer and Swenson (2012) showed the accuracy of various scaling techniques to estimate TWS observations at $1^{\circ} \times 1^{\circ}$ resolution. This enables the use of GRACE data for closing the water balance at a regional scale. Other studies related to the applications of the GRACE data in determining water storage changes include Cao et al. (2019a,b,c); Gonçalves et al. (2019); Jing et al. (2020); Meng et al. (2019); Van Dijk et al. (2011); Voss et al. (2013); and Wang et al. (2011).

The GRACE mission ended in 2017 and is continued through GRACE-Follow on (GRACE-FO) mission, which was launched in May 2018. The GRACE-FO carries a laser interferometry system to improve ranging precision between the two satellites (Sheard et al., 2012). The advancements in the GRACE-FO mission are likely to provide improvement in surface mass anomalies pertaining to terrestrial water storage, and ice sheets and adding further insights to the hydrological studies (Frappart and Ramillien, 2018).

3.2.3. Monitoring of reservoirs

Reservoirs play an important role in ensuring water security of a region, particularly during extreme drought events (Mishra and Singh, 2010). Reservoir monitoring is critical for the river basin management system as they regulate inter-seasonal and inter-annual fluctuations in streamflow (Gao et al., 2012). Reservoirs also help in flood control, hydroelectric power generation, facilitating continuous water supply, and other recreational activities. Despite their manifold importance, observations on water storage in reservoirs are either lacking or difficult to access. With the advent of radar altimetry, it has become possible to monitor the large reservoirs remotely. To estimate water storage in reservoirs, both surface water area and bathymetry measurements are required. With this intent, the data from multiple altimeters along with the MODIS data were used to create a time series of 34 global reservoir storages (Gao et al., 2012). Geoscience Laser Altimeter System (GLAS) of the Ice, Cloud, and land Elevation Satellite (ICESat) was used to extract storage information for 21 reservoirs in South Asia (Zhang et al., 2014). The Saral dataset was used to monitor the Maithon reservoir in Jharkhand, India (Ghosh et al., 2015). Bonnema and Hossain (2019) evaluated the ability of the SWOT mission to model changes in reservoir storage in the Mekong river basin. For lake and reservoir monitoring, Okeowo et al. (2017) developed an algorithm to directly extract water level information from the Jason-2 and ENVISAT radar altimeters to develop reservoir time series. This development may assist a large hydrologic community, which may have little knowledge in this field. In addition to directly using the altimeter data, the potential of assimilating altimeter data corresponding to reservoirs from different altimeter datasets for accurate river basin modeling is also explored (Cardenal et al., 2011; Michailovsky and Bauer-Gottwein, 2014).

3.3. Extreme events

3.3.1. Floods

Floods are one of the worst natural disasters that have the greatest impact on life, food, and water security. Globally, floods incurred economic losses up to USD 56 billion in 2016 (Wing et al., 2018). In March 2019 alone, global costs due to flooding are estimated to be around USD 8 billion (Podlaha et al., 2019). Some of the consequences of floods include anoutbreak of waterborne diseases (Kondo et al., 2002), crop damage (Rosenzweig et al., 2002), and drinking water contamination (Sirajul Islam et al., 2007), among others. These factors affect the sustainability of water resources. So, there is a need to develop strategies to monitor and manage floods in a basin. Some of the necessary steps include a) determining the vulnerable regions that get frequently affected due to floods in a region and subsequently establish appropriate legislation in terms of land-use planning and management, b) development of control and diversion structures that take shocks in the case of flash floods and extreme precipitation events and c) development of independent infrastructure to drain floodwaters in urban landscapes. These steps require continuous monitoring of water level, flood volume, and flood extent, which are the three factors that determine the severity of floodin a basin. It is important to note that insitu gauge sensors are expensive to monitor and are susceptible to damage during heavy flood events, which hinders the data acquisition process. Under these circumstances, there is a need to rely on satellite remote sensing information to monitor floods. Over the past two decades, there is an increased awareness among space agencies to utilize remote sensing information to monitor floods. Typically, optical, passive, and active microwave sensors are used to monitor floods. In this section, we review the role of satellite remote sensing for monitoring the flood extent. We review the remote sensing applications in streamflow detection, which includes water depth detection, in Section 4.2.1.

3.3.1.1. Flood extent using optical sensors. In the visible and thermal electromagnetic radiation spectrum, water has a relatively low reflectivity compared to other land cover types. This is the principle based on which flood monitoring is carried out using optical sensors. Details regarding some of the operational optical satellite sensors including AVHRR, VIIRS, MODIS, Sentinel, Landsat, SPOT, ASTER, IKONOS, Quickbird, Worldview, RapidEye, Ziyuan 3 (ZY-3), and Gaofen missions, among others, used for this purpose can be found in Table 1.

Typically, optical remote sensing signals include blue (0.45–0.52 μm for Landsat 4, 5, 7, and 8 missions; 0.45–0.48 μm for MODIS), green (0.50–0.57 μm), red (0.61–0.70 μm), near-infrared (NIR) (0.7–0.9 μm), and mid-infrared (MIR) (1.5–3 μm) bands. Several indices have been proposed in the past that evolved from using reflectance information from using band ratios to using a combination of multiple indices (Ma et al., 2019). These indices are useful in assessing the flood extent by classifying the areas of dry and inundated regions. Tasseled Cap Wetness (TCW) index (Crist, 1985; Crist and Cicone, 1984) is the earliest water index, which is derived as a combination of six bands of reflectance information sourced from Landsat. A threshold of 0 is set to identify water bodies. Normalized Difference Water Index (NDWI) proposed by McFeeters (1996) is one of the widely used water indices. It is expressed as a ratio of $\rho_{Green} - \rho_{NIR}$ and $\rho_{Green} + \rho_{NIR}$ (where ρ is surface reflectance). However, NDWI cannot separate the presence of water in built-up areas due to similar reflective characteristics of these two features in green and NIR bands (Zhou et al., 2017). Xu (2006) addressed this issue by replacing NIR with SWIR, resulting in the ratio between $\rho_{Green} - \rho_{SWIR}$ and $\rho_{Green} + \rho_{SWIR}$. However, this method cannot delineate water bodies in snow cover regions (Huang et al., 2018). Table 6 presents a summary of the water extraction indices proposed in the literature. Further information on the use of optical sensors in flood detection can be obtained from Huang et al. (2018), Ma et al. (2019), and Zhou et al. (2017). In the thermal spectrum, few studies have utilized the diurnal land surface temperature difference as an indicator to detect flood inundation (Ordoyne and Friedl, 2008; Parinussa et al., 2016).

Despite their ease of applicability, information from optical sensors is affected by the atmosphere in the form of clouds and particulate matter and vegetation. Besides, image acquisition can be carried out only during the daytime. In case of the presence of clouds or vegetation, the reflectance from these features can be so prominent that the image may not be useful to monitor floods in real-time. It is, therefore, necessary to use information from microwave sensors for the flood monitoring process.

3.3.1.2. Flood extent using active microwave sensors. Active microwave sensors emit their signals of electromagnetic radiations (in microwave frequencies) towards the Earth surface and measure the scattered signal (in the form of backscatter coefficient), which contains information about the surface's texture, shape and its dielectric properties (Woodhouse, 2017). Active microwave (radar) sensors can penetrate through clouds with less attenuation (Sanyal and Lu, 2004), and also provide information independent of solar illumination (Moreira et al., 2013). Their ability to acquire information in the order of ten to hundreds of meters provides an opportunity to monitor floods on rivers with a width of less than 1 km (Mason et al., 2011; Schumann et al., 2009). Some of the operational Synthetic Aperture Radar (SAR) microwave satellite missions include ALOS-2, SAOCOM-1A, RADARSAT-2, RISAT-1, COSMO-Skymed, and TerraSAR-X, among others. Details regarding these sensors can be found in Table 1.

The spatial and temporal resolutions of SAR imagery are critical factors for flood monitoring. There is an inherent tradeoff between these two resolutions. Generally, the spatial and temporal resolutions of SAR imagery will be in the order of 1–100 m and 11–46 days, respectively (Di Baldassarre et al., 2011; Schumann et al., 2009). To counteract the issue of low temporal resolution, space agencies are launching constellations of satellites, which work together. For example, the Sentinel-1 mission is a constellation of two satellites, which combinedly reduce the global revisit time to 6 days (Geudtner et al., 2014; Torres et al., 2012). The revisit time is reduced further to 5 days with the follow-up mission of Sentinel-2 (Drusch et al., 2012), which is launched in 2016. Besides, the COSMO-Skymed mission is also a constellation of four satellites, which can provide high-resolution SAR imagery with a revisit time as low as 2 h (Covello et al., 2010). The reduced revisit time will aid in flood monitoring as was implemented successfully in the past. The backscatter coefficient recorded in a SAR imagery is influenced by the characteristics of target and sensor such as a) surface roughness, and b) dielectric properties of target affect the backscatter coefficient, c) frequency of radiation, d) polarization, e) incidence angle, f) properties of atmosphere and g) meteorological conditions such as rainfall, wind speed, etc. The frequency of radiation has an inverse effect on the depth of penetration of the backscatter signal (Ulaby et al., 1982). Generally, backscatter coefficients from L-(0.5–1.5 GHz), C-(4–8 GHz), and X-(8–12 GHz) bands frequencies are found to be useful for flood monitoring studies with L-band having a greater ability to penetrate through vegetation and relatively lesser influence due to roughness (Grimaldi et al., 2016; Schumann et al., 2012). The sensitivity of the backscatter coefficient to surface roughness increases with increasing angles and vice versa (Ulaby et al., 1982). Water bodies generally appear darker with low backscatter signal unless affected by water surface roughness or wind stress (Bragg scatter) (Costa et al., 2006; Freeman and Durden, 1998).

Before analyzing the SAR data, it is important to pre-process the imageries in terms of geo-referencing (process of locating the image on the Earth), ortho-rectification (process of correcting the systematic sensor and platform induced geometry errors), and speckle removal (process of filtering the noise that persists in the backscatter signal) (Grimaldi et al., 2016). Several approaches have been developed in the past that map the flood extent using the SAR imageries. These methods can be called as image classification techniques since the prime objective is to differentiate the locations that are dry and wet (inundated). These methods can be broadly classified into a) visual interpretation, b) image thresholding, c) automatic image classification algorithms, d) active contour models, and e) change detection techniques. It has to be noted that each of these techniques has its advantages and disadvantages, and there is no optimal technique that applies to all case studies (Di Baldassarre et al., 2011; Grimaldi et al., 2016; Schumann et al., 2009).

The visual interpretation involves the examination of flood lines

Table 6
Summary of important optical water detection indices.

Index	Abbreviation	Equation	Satellite/Wavelengths (μm)	Reference
TCW	Tasseled Cap Wetness	$0.1509\rho_{Blue} + 0.1973\rho_{Green} + 0.3279\rho_{Red} + 0.3406\rho_{NIR} - 0.7112\rho_{SWIR-1} - 0.4572\rho_{SWIR-2}$	Landsat 5 Thematic Mapper (TM) and 7 ETM+ (Enhanced Thematic Mapper Plus); ρ_{Blue}: 0.45 − 0.52 ρ_{Green}: 0.52 − 0.60 ρ_{Red}: 0.63 − 0.69 ρ_{NIR}: 0.76 − 0.90 ρ_{SWIR1}: 1.55 − 1.75 ρ_{SWIR2}: 2.08 − 2.35	Crist (1985); Crist and Cicone (1984)
NDWI	Normalized Difference Wetness Index	$\frac{\rho_{Green} - \rho_{NIR}}{\rho_{Green} + \rho_{NIR}}$	Landsat 5 Multispectral Sensor (MSS); ρ_{Green}: 0.50 − 0.60 ρ_{NIR}: 0.80 − 1.10	McFeeters (1996)
mNDWI	modified Normalized Difference Wetness Index	$\frac{\rho_{Green} - \rho_{SWIR}}{\rho_{Green} + \rho_{SWIR}}$	Landsat 5 TM; ρ_{Green}: 0.50 − 0.60 ρ_{SWIR}: 1.55 − 1.75	Xu (2006)
OWI	Ouma Water Index	$f(TCW \pm k, NDWI_3)$, where k – constant; $NDWI_3 = \frac{\rho_{SWIR1} - \rho_{NIR}}{\rho_{SWIR1} + \rho_{NIR}}$	Landsat 5 TM, Landsat 7 ETM+	Ouma and Tateishi (2006)
OWL	Open Water Likelihood index	$f\begin{pmatrix} SWIR1, SWIR2, \\ NDWI_2, NDVI, MrVBF \end{pmatrix}$, where $NDWI_2 = \frac{\rho_{NIR} - \rho_{SWIR1}}{\rho_{NIR} + \rho_{SWIR1}}$, $NDVI = \frac{\rho_{NIR} - \rho_R}{\rho_{NIR} + \rho_R}$, $MrVBF = f(Elevation)$ ***MrVBF:*** multiresolution index of valley bottom flatness (Gallant and Dowling 2003)	Landsat 5 TM, Landsat 7 ETM+, Shuttle Radar Topography Mission (SRTM) Digital Elevation Model (DEM)	Guerschman et al. (2011)
AWEI	Automated Water Extraction Index	$AWEI_{nsh} = 4(\rho_{Green} - \rho_{SWIR1}) - (0.25\rho_{NIR} + 2.75\rho_{SWIR2})$ (for locations with no prominent shadow effect) $AWEI_{sh} = \rho_{Blue} + 2.5\rho_{Green} - 1.5(\rho_{NIR} + \rho_{SWIR1}) - 0.25\rho_{SWIR2}$ (for locations with prominent shadow effect)	Landsat 5 TM	Feyisa et al. (2014)
AMERL	Automated Method for Extracting Rivers and Lakes	$f\begin{pmatrix} NDWI, mNDWI, \\ AWEI_{nsh}, AEWEI_{sh} \end{pmatrix}$	Landsat 5 TM, Landsat 7 ETM+	Jiang et al. (2014)
WI_{2015}	Water Index	$1.7204 + 171\rho_{Green} + 3\rho_{Red} - 70\rho_{NIR} - 45\rho_{SWIR1} - 71\rho_{SWIR2}$	Landsat 5 TM, Landsat 7 ETM+	Fisher et al. (2016)
CWI	Combination Water Index	Combination of mNDWI and vegetation indices (NDVI and EVI)	Landsat 5 TM, Landsat 7 ETM+	Zou et al. (2017)

from imageries. Although this method is a straightforward way to map the flood extent, the outcome can be erroneous due to the influence of factors such as flooded regions appearing to be brighter due to roughness and wind effects. Some of the studies that implemented this technique include (Brivio et al., 2002; Giustarini et al., 2016; MacIntosh and Profeti, 1995; Oberstadler et al., 1997). Image thresholding is an efficient and simplest approach for image classification (Landuyt et al., 2018). In these techniques, a radiometric threshold value is determined to differentiate two classes (flood, non-flood areas) that have significantly different pixel distributions. Image thresholding techniques can be broadly classified as follows (Sezgin and Sankur, 2004):

(1) histogram shape-based methods – analyze the peaks and valleys among other properties of the smoothened histogram of image (Guo and Pandit, 1998; Martinis et al., 2009; Ramesh et al., 1995; Rosenfeld and De La Torre, 1983; Sezan, 1990),
(2) clustering-based methods – which separate the image into two clusters that correspond to water and non-water pixels (Chang et al., 2010; Cho et al., 1989; Jawahar et al., 1997; Otsu, 1979; Ridler and Calvard, 1978; Schumann et al., 2010),
(3) entropy-based methods – determine the entropy of the two clusters and the cross-entropy between the original and binarized images (Cheng et al., 1999; Kapur et al., 1985; Rajinikanth et al., 2018; Sahoo et al., 1997; Sarkar et al., 2016),
(4) object attribute-based methods – which assess the similarity between original and binarized images (Dasgupta et al., 2018; Hertz and Schafer, 1988; Martinis et al., 2009; Pikaz and Averbuch, 1996; Pulvirenti et al., 2011),
(5) spatial methods – which use probability distributions between the pixels (Brivio et al., 2002; Cao et al., a,b,c).

The threshold value obtained from the above-described techniques is dependent on satellite sensors, land surface, and environmental conditions. So, these techniques have to be applied on a scene-by-scene basis. Consequently, these techniques turn out to be time-consuming and are also prone to errors due to the subjectivity of the image in focus. Automatic thresholding techniques try to alleviate this problem by determining automatically the threshold gray value that separates the flood and non-flood values. These techniques vary according to the estimation of the threshold at a global scale (single threshold for the whole image) (Pal and Pal 1993) or local scale (threshold according to local conditions) (Sahoo et al., 1988). They also differ based on the involvement of parameters in the models (leading to parametric and nonparametric models). Some of the automated methods were proposed by Chini et al. (2017), Giustarini et al. (2012), Martinis et al. (2015), Martinis et al. (2009), Matgen et al. (2011), and Wan et al. (2019). For instance, Martinis et al. (2015)'s technique involves the division of SAR image into non-overlapping tiles, and an iterative procedure is adopted to select representative tiles that have a histogram with strong bimodality. This technique is implemented as an on-demand TerraSAR-X based flood determination service, which is extended to Sentinel-1C-band data (Twele et al., 2016).

Active Contour Models (ACM), also called as snakes are one of the widely used automatic techniques for flood extent delineation (Caselles et al., 1993; Chan and Vese, 2001; Cohen, 1991; Horritt, 1999; Horritt et al., 2001; Kass et al., 1988). ACMs involve a dynamic curvilinear contour, which evolves, subject to image constraints, to determine objects of the image. Contours are a set of nodes connected with straight lines. The objects in the context of floods can be land and flood-inundated areas. The contour is driven by an energy function, which attracts the contour towards the edges of the object. This energy function considers the changes in backscatter coefficients inside the region, the changes in backscatter coefficients outside the region, and an edge length parameter (Debusscher and Van Coillie, 2019). This search process continues until the flooded area is identified. Several studies implemented ACMs for the detection of flood inundation (Bates et al., 1997; Bates et al., 2006; De Roo et al., 1999; Debusscher and Van Coillie, 2019; Horritt, 1999; Horritt et al., 2001; Landuyt et al., 2018; Schumann et al., 2012).

The methods described above deal single image. Change detection methods, on the other hand, use two images, non-flooding and post-flooding of the same region of interest. Through these two images, the difference in the backscatter coefficients can be obtained, which can be used further for delineating the inundated areas. The difference in the two images is calculated generally as a ratio (Moser and Serpico, 2006) or log-ratio (Bazi et al., 2005; Chini et al., 2017) to counteract the multiplicative nature of speckle in the SAR data. Hostache et al. (2012) noticed that the selection of reference (non-flooding) images could significantly affect the output from change detection techniques. This is due to the high variability of backscatter coefficients as a result of atmospheric components, land surface processes such as soil moisture, evapotranspiration, seasonality in the vegetation characteristics, land-use changes, and the image acquisition characteristics. In this context, Moya et al. (2019) identified that change detection could cause false detection of floods in agricultural areas, and attempted to address this issue by proposing a new parameter that is helpful to determine if the detected change is attributed to either flooded or non-flooded area in the agricultural region.

Recently, Landuyt et al. (2018) compared a couple of thresholding techniques, ACM and change detection, using SAR images of several flood events that occurred in the UK and Ireland. They indicate that ACMs can produce flood maps at greater accuracy at the expense of computational resources, whereas (Martinis et al., 2015)'s automated thresholding technique is suitable for near-real-time flood detection and monitoring. Efforts are made to include multiple techniques in order to obtain much accurate flood maps. For example, Matgen et al. (2011) proposed an automated SAR flood monitoring system wherein they used both thresholding and change detection techniques. Long et al. (2014) proposed Change detection and thresholding (CDAT) method for flood extent delineation in Caprivi region of Namibia.

3.3.1.3. Flood extent using passive microwave sensors. Passive microwave radiometers capture the naturally emitted electromagnetic radiations from the Earth's surface in the form of brightness temperatures. Due to the differences in the thermal inertia and the emissivity of land and water, the brightness temperatures recorded by the satellite are colder over the water surface. This contrast in brightness temperatures is generally utilized for detecting flood inundated regions (Choudhury, 1989; Hamilton et al., 1996; Schmugge, 1987; Smith, 1997). In this context, Brakenridge et al. (2007) developed a technique that uses horizontal polarization Ka-band (~37 GHz) frequency information. In this work, the ratio between the brightness temperature of the target grid cell and a background/calibration/reference/dry grid cell is computed, which corresponds to the variations in the discharge and the water extent in the grid cell. Besides, Basist et al. (1998) proposed a method to determine water extent using the notion of a decrease in emissivity with increase in the fraction of water surface in a pixel. They related this emissivity with the difference in brightness temperature across multiple frequencies. In this process, they derived an index called Basin Water Index (BWI), which is demonstrated using vertically polarized SSM/I 19, 37, and 85 GHz frequencies. It is important to note that the brightness temperature measurements are only available in the order of tens of kilometers due to the low energy of microwave emissions. So, it will be possible to assess the flood extent only in the case of large catchments of areas greater than 1000 km^2 (Grimaldi et al., 2016). Also, the microwave signals have noticeable attenuation due to the atmosphere beyond X-band frequency (Prigent et al., 2016; Karthikeyan et al., 2017). So, these attenuations should also be accounted for during the retrieval process. Nevertheless, several global flood monitoring systems utilize information from passive microwave sensors. For instance, Global Flood Detection System - Version 2 (Kugler and De Groeve, 2007) coordinated by Global Disaster Alert and Coordination System (GDACS) in collaboration with Dartmouth Flood Observatory produces flood information using AMSR2 and Global Precipitation Mission (GPM) sensors (https://www.gdacs.org/flooddetection/overview.aspx).

There are certain merits and demerits associated with each of these optical, active, and passive microwave products. Recognizing the need to combine the strengths of each of these sensors to obtain flood information with improved accuracy, efforts have been to develop multi-satellite global flood monitoring systems. Prigent et al. (2001) developed Global Inundation Extent from Multi-satellites (GIEMS) (Prigent et al., 2016), which combines information from SSM/I (passive microwave sensor), ERS (European Remote Sensing satellite – active microwave sensor), and AVHRR (Advanced Very High-Resolution Radiometer – optical sensor) to provide monthly global inundation maps at 25 km resolution over the period 1993–2007. Furthermore, Schroeder et al. (2015) developed Surface Water Microwave Product Series (SWAMPS) by combining information from passive sensors – SSM/I, SSMIS (Special Sensor Microwave Imager/Sounder), active sensors – ERS, QuikSCAT, and ASCAT (Advanced SCATterometer), an optical sensor – MODIS. SWAMPS produced global scale surface water fraction maps at 25 km covering the period 1992–2013. Recently, Parrens et al. (2019) developed a 1 km inundation product at three days temporal resolution over the Amazon basin using information from Soil Moisture Ocean Salinity (SMOS), Landsat, and Shuttle Radar Topography Mission (SRTM) Digital Elevation Model (DEM) over the period 2010–2016.

3.3.2. Droughts

The demand for water has increased significantly due to the growth of population and expansion of agricultural, energy and industrial sectors, which resulted in frequent water scarcity in many parts of the world (Mishra and Singh, 2010). The water scarcity is aggravated by droughts that impact surface and groundwater resources leading to reduced water supply, deteriorated water quality, risk of wildfires (Taufik et al., 2017), livestock (Murray-Tortarolo and Jaramillo, 2019), food production (Cottrell et al., 2019), water stress (Pedro-Monzonís et al., 2015; Shah and Mathur, 2019) among others. Therefore, drought management related investigation (e.g., monitoring, forecasting, and risk assessment) is essential for the planning and management of water resources.

Droughts are triggered by the anomalous behavior in hydroclimatic variables, such as reduction in precipitation, increase in temperatures, low relative humidity, and distribution of rainy days (Mishra and Singh, 2010). With the advent of satellite remote sensing, it is now possible to track the anomalous behavior of such variables at different spatio-temporal scales. Droughts are classified broadly into meteorological, hydrological, agricultural, and socio-economic droughts (Mishra and Singh, 2010). Although there is no standard definition of drought (Mukherjee et al., 2018), it generally originates due to the deficit of water compared to normal conditions (Van Loon et al., 2016). Since droughts are associated with the movement of water in the hydrological cycle, the droughts mentioned above are intricately related to each other. In this context, several drought indices have been proposed in the past that assess the individual as well as the multivariate nature of droughts (Rajsekhar et al., 2015). The following sections present the applications of remote sensing towards assessing meteorological, hydrological, and agricultural droughts.

3.3.2.1. Meteorological drought. Meteorological drought is associated with the lack of occurrence of precipitation over a duration (Mishra and Singh, 2010). Traditionally, the meteorological drought analysis is carried out using in-situ precipitation information (Zuo et al., 2019). Palmer Drought Severity Index (PDSI) (Palmer, 1965) is used as a meteorological drought index, and it measures the departure of the moisture supply based on the supply-and-demand concept of the water balance equation. The PDSI is calculated by accounting precipitation and temperature data, as well as the local available water content of the soil. Several limitations of PDSI (Palmer, 1965; Mishra and Singh, 2010) are addressed through self-calibrating PDSI(sPDSI) (Wells et al., 2004). There are limited studies that incorporated remote sensing information to derive PDSI. For example, Yan et al. (2014) incorporated remotely sensed Global Inventory Modeling and Mapping Studies (GIMMS) Leaf Area Index (LAI) based ET in to sPDSI to carry out drought assessment at the global scale.

Standardized Precipitation Index (SPI) (McKee et al., 1993) is another meteorological drought index, which is calculated using long-term precipitation data at a given location. SPI involves fitting precipitation to an appropriate probability distribution and then transforming it to a normal distribution. Since the SPI requires only precipitation data, it is one of the widely used meteorological drought indices. However, there is a need for at least 30 years of precipitation data to obtain a reliable statistical fit while estimating the SPI. With the advent of long-term remote sensing based products such as CHIRPS (Climate Hazards Group InfraRed Precipitation with Station) (Funk et al., 2015) and MSWEP (Multi-Source Weighted-Ensemble Precipitation) (Beck et al., 2019), it is now possible to determine SPI using this information. For instance, Bayissa et al. (2017) used CHIRPS data to monitor meteorological drought in Ethiopia. Shrestha et al. (2017) assessed the accuracy of the SPI estimates of CHIRPS over the Koshi basin, Nepal, and observed that SPI values identified historical droughts. Recently, Golian et al. (2019) compared the SPI of CHIRPS and MSWEP along with reanalysis and gauge based precipitation datasets at global scale. They found that the drought indices are sensitive to the choice of precipitation dataset, its length, and spatial resolution.

In addition, some more drought indices are proposed that utilize remote sensing data. Anderson et al. (2011) and Anderson et al. (2007) developed remote sensing based Evaporative Stress Index (ESI), which represents the temporal anomalies in the ratio between actual evapotranspiration (AET) and potential evapotranspiration (PET). The ESI is computed using TIR and vegetation cover fraction imagery of Geostationary Operational Environmental Satellites (GOES). Kim and Rhee (2016) proposed Standardized Evapotranspiration Deficit Index (SEDI), a fully ET-based index that is derived using the complementary relationship between evaporative demand and AET. Vicente-Serrano et al. (2018) used GLEAM AET estimates to carry out drought assessment using SEDI at global scale. Since ESI and SEDI are independent of rainfall, they can be used as a reference to evaluate the precipitation based meteorological drought indices.

Recognizing the need to include evapotranspiration while characterizing meteorological drought, Vicente-Serrano et al. (2010) proposed a new multiscalar drought index named the Standardized Precipitation Evapotranspiration Index (SPEI). SPEI works similar to SPI, with the difference between precipitation and potential evapotranspiration (PET) as the random variable of interest. This difference essentially provides climatic water balance, i.e., whether there exists a water surplus or water deficit in a particular month. In a recent study, Zhao and Ma (2019) considered TRMM, CHIRPS, and PERSIANN-CDR (Precipitation Estimation from Remotely Sensed Information using Artificial Neural Networks- Climate Data Record) (Ashouri et al., 2015; Hsu et al., 1997) along with other precipitation products to estimate SPEI at the global scale. They found PERSIANN-CDR to be relatively more suitable for long-term drought monitoring purposes. Similar to SPEI, Reconnaissance Drought Index (RDI) (Tsakiris et al., 2007) is a meteorological drought index computed as a ratio between accumulated rainfall and PET. Dalezios et al. (2012) determined RDI for drought assessment using remotely sensed information based PET and station rainfall data in Greece. Zhang and Jia (2013) proposed Microwave Integrated Drought Index (MIDI) that considers TRMM precipitation, AMSR-E derived land surface temperature, and soil moisture for monitoring short-term meteorological drought. Zhang et al. (2019a) attempted to improve meteorological drought monitoring using multi-satellite precipitation products with MIDI in tropical and subtropical water-limited climates. They found multi-satellite MIDI estimates to correlate well with SPI and SPEI.

3.3.2.2. Agricultural drought. Agricultural drought occurs due to a decline in soil moisture, which subsequently leads to the failure of crops (Mishra and Singh, 2010). The lack of water in the soil can be attributed to a deficit in rainfall or lack of irrigation (due to lack of water in the reservoirs) along with a greater amount of evapotranspiration from the soil. Therefore, agricultural drought monitoring is carried out primarily by analyzing the patterns of vegetation and soil moisture. Agricultural drought is also intricately related to the meteorological conditions. Several studies indicated the link between the agricultural drought and precipitation anomalies (Elagib, 2013; Kurnik et al., 2011; Rouault and Richard, 2003; Svoboda et al., 2012). So, attempts are made to study agricultural drought in an integrated manner. We find that there is a relatively greater number of agricultural drought indices compared to the meteorological drought indices proposed in the literature.

PDSI has an issue of reacting slowly to short-term droughts, which, if overlooked, can impact the monitoring of crop growth (Narasimhan and Srinivasan, 2005). Crop Moisture Index (CMI) developed by Palmer (1968) attempts to alleviate this problem. It is calculated based on PET and soil moisture depletion with soil water balance as a governing concept. On a similar idea, Relative Soil Moisture (RSM) (Thornthwaite and Mather, 1955), Agricultural Drought Index (DTx) (Matera et al., 2007). Narasimhan and Srinivasan (2005) noted that CMI, similar to PDSI, has limitations of assuming uniform properties of land use and soil in a climatic zone. They attempted to address this issue through new indices called the soil moisture deficit index (SMDI) and evapotranspiration deficit index (ETDI) by simulating soil moisture and ET using Soil Water Assessment Tool (SWAT). Attempts are made to analyze multiple types of droughts by using the water-energy balance equation (Ayantobo and Wei, 2019; Zhang et al., 2019b). Similar to the computation of SPI, Standardized Soil Moisture Index (SSI) can be derived based on the soil moisture information (Mishra et al., 2015; AghaKouchak, 2015). Zhang et al. (2019d) computed weekly SSI using ESA-CCI soil moisture product for agricultural drought monitoring of the Yellow river basin, China.

With the advent of remote sensing information, several compatible agricultural drought indices are proposed. Hunt et al. (2009) and Sridhar et al. (2008) proposed the Soil Moisture Index (SMI), which is calculated as a function of the ratio of the difference between soil moisture and wilting point, and the difference between field capacity and wilting point. Recently, Martínez-Fernández et al. (2015) modified the SMI to propose Soil Water Deficit Index (SWDI) wherein the soil moisture deficit is limited by field capacity instead of wilting point (in the numerator). Given its advantage of being independent of the length of the record, SWDI can be applied even on shorter soil moisture time series. Mishra et al. (2017) used SMAP soil moisture to generate SWDI to monitor agricultural drought over the Contiguous United States (CONUS). Carrão et al. (2016) proposed Empirical Standardized Soil Moisture Index (ESSMI) using ESA-CCI soil moisture data by estimating the standard normal variates of empirical distribution of soil moisture at various timescales.

In terms of characterizing the agricultural drought corresponding to vegetation, the Normalized Vegetation Difference Index (NDVI) (Tucker, 1979) is probably the most famous remote sensing based index. It is calculated as the ratio of difference between reflectance of near-infrared (NIR) and red (R) bands and the sum of NIR and R bands of an optical satellite/airborne sensor. NDVI indicates the condition of vegetation (healthy or unhealthy) and its presence. However, it is associated with certain limitations (Zargar et al., 2011). This resulted in alternate vegetation indices such as Enhanced Vegetation Index (EVI) (Liu and Huete, 1995), Soil Adjusted Vegetation Index (SAVI) (Epiphanio and Huete, 1995; Huete, 1988), Normalized Difference Water Index (NDWI) (Gao, 1996), and Normalized Multi-band Drought Index (NMDI) (Wang and Qu, 2007). Furthermore, Vegetation Condition Index (VCI) (Kogan, 1990) is a scaled version of NDVI, computed as $VCI_t = (NDVI_t - NDVI_{\min})/(NDVI_{\max} - NDVI_{\min})$ at time t, that removes the effects of weather in NDVI and determines the health of vegetation. It is used extensively for agricultural drought monitoring in the literature. Quiring and Ganesh (2010) estimated VCI using Advanced Very High Resolution Radiometer (AVHRR) to assess the possibility of using VCI as a meteorological drought indicator in Texas. In a similar attempt, Zambrano et al. (2016) carried out agricultural drought monitoring with VCI using MODIS MOD13Q1 NDVI product over cropland areas in Chile and compared the outcome with station based SPI. Similar to VCI, Temperature Condition Index (TCI) is proposed to determine how vegetation reacts to temperature ($TCI = (LST_{\max} - LST)/(LST_{\max} - LST_{\min})$) (Kogan (1995).

Apart from the above indices, some of the hybrid drought indices are also proposed in the literature that considers remote sensing information can input. As an extension of VCI and TCI, Kogan (1995) introduced the Vegetation Health Index (VHI), which is a linear combination of TCI and VCI. Mostly an equal weight is assigned to TCI and VCI while calculating VHI (Kogan, 1997). Recently, Bachmair et al. (2018) compared MODIS based VCI and VHI with SPI and SPEI over Europe under crop and forest land cover conditions. Brown et al. (2008) developed an integrated drought index called the Vegetation Drought Response Index (VegDRI) that uses climate, satellite, and biophysical variables in a statistical regression framework. Similarly, Rhee et al. (2010) proposed Scaled Drought Condition Index (SDCI) for monitoring agricultural droughts. SDCI is computed as a linear combination of scaled MODIS LST, NDVI, and TRMM precipitation. Using a linear combination of ratios of ET and PET and NDVI, Mu et al. (2013) proposed Drought Severity Index (DSI), which is based on MODIS products. Vyas et al. (2015) proposed a Combined Deficit Index (CDI) to characterize agricultural drought. It is based linear combination of remotely sensed rainfall and NDVI datasets. Zuo et al. (2019) used CDI to assess agricultural drought in Northeast China. Liu et al. (2017b) used the relationship between satellite brightness temperature (from AMSR-E) and NDVI (from MODIS) to develop Microwave Temperature Vegetation Drought Index (MTVDI).

While determining an integrated agricultural drought response, it is essential to note that vegetation exhibits lagged response to the meteorological drought due to the residual soil moisture content and the soil moisture memory (Anderson et al., 2012; Di et al., 1994). Therefore, it is important to consider this lag for the accurate characterization of the agricultural drought. In this context, Sánchez et al. (2016) proposed Soil Moisture Agricultural Drought Index (SMADI) by integrating the Soil Moisture Condition Index (SMCI, formulation of which is similar to that of VCI), a modified version of TCI, and lagged VCI. SMADI is found to capture the agricultural droughts when tested using SMOS soil moisture, MODIS LST, and NDVI at global scale (Sánchez et al., 2018).

The multivariate drought indices are recently derived from integrate different types of drought (Rajsekhar et al., 2015). Kao and Govindaraju (2010) proposed the Joint Deficit Index (JDI) that utilized copulas to estimate probability based integrated drought index by considering multiple drought indices. Hao et al. (2014) developed the Multivariate Standardized Drought Index (MSDI), which is the normalization of the joint probability of accumulated rainfall and soil moisture. Recently, attempts are made to assess the agricultural droughts using the water balance equation (Cao et al., a,b,c). Further information on the multivariate drought indices can be obtained from Hao and Singh (2015).

3.3.2.3. Hydrological drought. Hydrological drought is associated with the deficit in surface and subsurface water resources (Mishra and Singh (2010). The meteorological drought can trigger agricultural drought, which can lead to hydrological drought (Sheffield and Wood, 2007; Sheffield et al., 2012). Traditionally, the streamflow anomalies are analyzed to identify the periods of hydrological drought (Keyantash and Dracup, 2002). Palmer Hydrological Drought Index (PHDI) (Palmer and Drought, 1965) is the earliest hydrological drought index. PHDI works similar to PDSI. Whereas PDSI considers the end of drought as the moisture deficit begins to subside gradually, PHDI considers the end of drought when the moisture deficit is subsided completely to assess the hydrological drought (Heim, 2000; Keyantash and Dracup, 2002). PHDI does not work in the basins, which have snowmelt runoff contribution in the streamflow. Shukla and Wood (2008) developed the Surface Runoff Index (SRI) to characterize hydrological drought. To the best of our knowledge, no studies have been carried out that integrated remote sensing information into these drought indices. In this context, West et al. (2019) noted that there is relatively limited research in the area of quantifying hydrological droughts compared to that of meteorological and agricultural droughts.

The launch of GRACE and its follow on missions in 2002, and 2018 respectively (Flechtner et al., 2014; Tapley et al., 2004b), opened up possibilities of estimating the Terrestrial Water Storage (TWS) components of soil moisture, surface and subsurface water in a basin. With these missions, the research on the application of remote sensing to investigate hydrological (groundwater) drought flourished. The difference between monthly TWS anomalies and climatology of TWS anomalies with subsequent transformation was applied to identify hydrological droughts (Sinha et al., 2017; Thomas et al., 2014; Zhang et al., 2016). Yirdaw et al. (2008) developed the Total Storage Deficit Index (TSDI) by standardizing the monthly TWS anomaly and then combining the outcome at a timestep with that of that previous timestep through an arithmetic weighted summation. Recently, Forootan et al. (2019) derived a multivariate drought index based on the precipitation and TWS to conduct global hydrological drought assessment along with their relationship with climatic teleconnections. Furthermore, GRACE data is assimilated into hydrological models to study hydrological drought (Schumacher et al., 2018). Given its coarse resolution, attempts are being made to downscale the GRACE TWS data (using hydrological models), which can assist in monitoring hydrological droughts (Zhang et al., 2019c).

Groundwater is a crucial component of the hydrological cycle. Mishra and Singh (2010) define groundwater drought as the situation of the below-normal groundwater level. Since the GRACE mission provides information regarding groundwater storage, several studies used GRACE data to assess groundwater drought. The separation of groundwater components from TWS estimates is carried out generally using the water balance equation or by using the simulations of land surface models. GRACE estimates are helpful to identify groundwater depletion in a region (Asoka et al., 2017; Castle et al., 2014; Famiglietti et al., 2011; Huang et al., 2015; Long et al., 2013; Richey et al., 2015; Rodell et al., 2009; Zhao et al., 2019). Attempts are being made to utilize GRACE TWS estimates in tandem with interferometric SAR data and GPS measurement sensors to determine the groundwater depletion (Castellazzi et al., 2018; Liu et al., 2019; Ojha et al., 2018; Rateb and Kuo, 2019). Some studies assimilated GRACE data into hydrological models to assess the groundwater depletion (Döll et al., 2014; Khaki et al., 2018). Such GRACE based data assimilation techniques also carried out to investigate the groundwater droughts (Li and Rodell, 2015; Li et al., 2019). Van Loon et al. (2017) used GRACE TWS anomalies along with hydrological model simulations are to assess the 2015 European groundwater drought. On a similar note, Mishra et al. (2016) conducted drought assessment over India using GRACE anomalies. Recently, Thomas et al. (2017) proposed GRACE Groundwater Drought Index (GGDI) based on normalized GRACE groundwater storage deviations to study groundwater drought in California Central Valley. Recent studies attempted to assimilate the GRACE data into land surface models to improve the accuracy of groundwater storage information, which is expected to contribute towards drought monitoring purposes (Getirana et al., 2019; Li et al., 2019).

3.3.2.4. Drought prediction using remote sensing. Remote sensing information is also used for drought forecasting purposes. The drought forecasting is carried out using either statistical models or physical models in an assimilation framework (Hao et al., 2018). In the case of statistical models, time series prediction models or regression models are established between appropriate predictors and remotely sensed datasets such as SPI, SPEI, NDVI, VTCI, soil moisture, and TWS anomalies, among others (De Linage et al., 2014; Mishra and Desai, 2005, 2006; Mishra et al., 2007; Park et al., 2018; Rhee and Im, 2017). On the other hand, remote sensing products are ingested into land surface models in a data assimilation framework to carry out short-term as well as long-term prediction of droughts (Mishra and Singh, 2011; Sheffield et al., 2014; Liu et al., 2017; Yan et al., 2017). Satellite remote sensing products are also being utilized in drought early warning systems (Funk et al., 2019; Pozzi et al., 2013; Tadesse et al., 2014).

3.3.2.5. Regional drought analysis using remote sensing. Regional drought analysis can generate spatio-temporal drought information, which plays an important role to improve water resources management at a regional scale (Mishra and Singh, 2011). The regional analysis integrates different components of the drought characteristics, such as duration, severity, area, and frequency (Mishra and Singh, 2009, 2011). The regional analysis can be carried out using different variables, such as drought indices, rainfall, streamflow and soil moisture (Alijanian et al., 2019; Dabanlı et al., 2017; Hisdal et al., 2001; Mishra and Singh, 2009), and these variables can be obtained (derived) from the remote sensing products.

The regional drought analysis typically combines more than one drought characteristics, for example, Intensity-Duration Frequency curves (Hallack-Alegria and Watkins, 2007); Total areal deficit and maximum deficit intensity (Tase, 1976); severity- area- duration (SAD) curves (Andreadis et al., 2005). The gauged precipitation data can be used for regional drought analysis, or these data can be used to derive Standardized Precipitation Index (SPI) for regional drought assessment (Mishra and Desai, 2005, Mishra and Singh, 2008, Bonaccorso et al., 2015, Cai et al., 2015; Dabanlı et al., 2017).

The regional drought information is critical for water resources management (Mishra and Singh, 2011; Alijanian et al., 2019), therefore, it is important to investigate the regional or spatial behavior of droughts (Panu and Sharma, 2002; Mishra and Singh, 2011; Bonaccorso et al., 2015), especially for data scarce regions (Mishra and Singh, 2011). However, one of the key limitations is lack of high-quality and continuous hydroclimate data to capture spatial coverage in many parts of the world (Mishra and Singh, 2011). To overcome such limitations, long-term satellite datasets can be a reliable alternative source for drought assessments in un-gauged basins. Some of the examples of long term (up to 30 years) satellite rainfall products are PERSIANN-CDR (Beck et al., 2017), and MSWEP (Beck et al., 2017). Although a number of studies investigated the performance of satellite rainfall products for temporal drought analysis, limited number of studies investigated the regional drought analysis (Alijanian et al., 2019). In a recent study, Alijanian et al. (2019) evaluated the performance of satellite rainfall estimates (PERSIANN-CDR and MSWEP) for regional drought analysis for Iran and to compare the four major historical severe drought events over the different climatic regions. The performance of remote sensing products may differ with respect to gauge data in terms of quantifying drought characteristics (e.g., severity, duration, and frequency), and identification of major historical droughts. The performance of selected remote sensing products largely differs in terms of quantifying the frequency component embedded in the regional drought analysis for selected climatic regions located in Iran.

4. Summary

In this work, we review role of remote sensing in addressing three critical aspects of water security, i.e., (i) water quality, (ii) water quantity - surface and sub-surface water resources, and (iii) extreme events. This review suggests that the satellite data offers promising results for the monitoring of the aforementioned categories. The satellite measurements will increase the observation network to map the water resources globally. The use of remotely sensed data for estimating water quality parameters, river discharge, reservoir monitoring, groundwater storage, and mapping the extreme events is likely to provide valuable information related to the water availability in order to improve water security of a region. Following is the summary of the review:

Water quality: The spectral properties of clear water are significantly different from polluted water. This feature is explored by the remote sensing sensors to monitor water quality. The water quality estimation is mostly carried out in the visible region of the spectrum. Chlorophyll (Chl) concentration, turbidity and Total Suspended Solids (TSS), Secchi Disk Depth (SDD), and Colored Dissolved Organic Matter (CDOM) are the most common water quality parameters estimated using the remote sensing datasets. Attempts are made to establish statistical relationship between water quality parameters and spectral reflectance. For this, data from Landsat, MODIS, OrbView-2 (SeaWiFS), MERIS, Sentinel-2, and Hyperion are increasingly used. For Chl mapping, bandwidths of 675 nm and 700 nm are found to be most useful, whereas Red and NIR bands are found to be useful for turbidity and TSS mapping. Apart from the use of single bands, incorporation of reflectance from multiple bands through band ratios is noted to improve water quality parameter estimates by reducing the effect of atmosphere and increasing the signal to noise ratio. The SDD is inversely related to turbidity and TSS concentration and is therefore estimated using empirical relationships with TSS and turbidity. Similarly, CDOM is found to be strongly correlated to Chl-a, TSS and turbidity levels. The lack of extensive availability of remote sensing datasets required for water quality monitoring adds large uncertainties to the estimates, highlighting the need for further improvement in the data. Further, most of the algorithms are empirical in nature, which requires accurate parameterization that can vary with the optical properties of the water body. During recent years, the merging of multispectral data with hyperspectral sensor data is also being attempted to accurately determine the water quality parameters.

Water quantity: Streamflow, reservoirs, and terrestrial water storage (TWS) contribute to the surface and subsurface water resources in a region. Satellite altimetric datasets are most commonly used for estimating water levels in rivers and reservoirs. A combination of different altimetric datasets is found to be useful for streamflow estimation and reservoir monitoring. The earlier altimeter missions were successful in mapping only large rivers and reservoirs due to their large footprint. However, the recent datasets such as Jason-2, Jason-3, and Saral are capable of monitoring small rivers with varying width. Besides, incorporation of other remotely sensed data pertaining to river widths and paths can significantly improve the river water level estimates. Apart from altimeter datasets, ancillary data pertaining to water-surface area, channel slope, average channel width, and velocity of rivers can be obtained from remote sensing datasets and can be used in hydraulic equations to estimate discharge. The recent advancements in the data assimilation has shown the potential to improve the water level estimates. The upcoming SWOT mission will be a significant development in estimating river discharge and storage. For monitoring changes in TWS, the GRACE twin satellite mission is commonly used. GRACE data is also used for mapping groundwater changes and groundwater depletion. One of the major limitations of the GRACE data is its coarse resolution, which limits its application at continental scale. However, efforts are currently being made to disaggregate the TWS at fine resolution for hydrologic studies.

Extreme events (floods): Estimation of flood extent is carried out using optical/thermal, active microwave, and passive microwave sensors. The optical/thermal reflectances are used to develop indices, which can indicate the inundated areas and dry areas in a region. The applicability of these indices is restricted to daytime-cloud free conditions. Microwave sensors address this issue, by providing measurements that have atmosphere penetration capability, and are independent of solar illumination. In the case of active microwave sensors, the SAR image, after necessary pre-processing, is subjected to classification algorithms such as image thresholding, active contour models, and change detection technique, etc., to identify flooded pixels. Attempts are made to develop automatic flood extent detection schemes by using a combination of the above methods. Information from passive microwave sensors can be used to detect the flood extent based on the low emissivity of inundated areas compared to that of dry pixels. Due to the coarse resolution of brightness temperatures from passive microwave sensors, the flood extent analysis can be carried out only on large catchments. Efforts are in progress to utilize the individual merits of each of the described sensing systems towards the development of global flood inundation maps.

Extreme events (droughts): Satellite remote sensing is used to analyze meteorological, agricultural, hydrological, and groundwater droughts. Long records of remote sensing-based precipitation and ET datasets (available from the early 1980s) are useful to conduct meteorological drought analysis using indices such as SPI and SPEI. Efforts are made to develop indices to apply with microwave precipitation products. In the context of agricultural droughts, several drought indices are proposed in the literature, which characterizes the persistent soil moisture deficit and vegetation stresses. Some of the drought indices, such as SMI, SWDI, ESSMI, etc., are developed considering satellite soil moisture products. Vegetation indices are widely used to determine the vegetation stresses. Efforts are being made to combine variables affected during agricultural drought, such as ET, LST, along with soil moisture and vegetation, into drought indices. Besides, such attempts are made through a statistical viewpoint, resulting in multivariate drought indices. The role of remote sensing in analyzing hydrological and groundwater droughts has become popular with the launch of the GRACE satellite. The TWS estimates from GRACE are used to develop hydrological and groundwater drought indices. Remote sensing information is now an integral part of drought prediction algorithms. The hydrometeorological observations obtained in near-real-time from operational satellite missions are being utilized in famine early warning systems. Since remote sensing products have the ability to cover larger spatial extent, they are used to carry out regional drought analysis that typically assesses features such as intensity, duration, frequency, severity, and area of droughts. Despite the advantages, the systematic differences between the remote sensing products of the same variable may affect the outcome. So, caution should be exercised while selecting an appropriate product.

5. Outlook

Satellite remote sensing plays a vital role in monitoring key hydroclimate variables as well as in managing water resources. In this work, we review three aspects of the role of remote sensing in assessing water security, water quality, water quantity, and extreme events. In this process, we reviewed how satellite sensors that measure signals from the Earth's surface across various frequencies, including optical, thermal, and microwave spectrum, along with gravity field measurements, are contributing to the above areas of research.

We present the following outlook with the wisdom gained from the review:

- Most of the water quality parameters, such as color dissolved organic matter (CDOM) and Secchi Disc Depth (SDD), are represented through total suspended sediments. There is a need for improvements in the sensing systems as well as retrieval methods that enable direct detection of these parameters at global scales.
- Regarding flow estimation, most of the research is limited to detecting flows in large rivers such as Mekong, Congo, Amazon, Ganga, and Brahmaputra. Although the research is still advancing to improving the flow measurement accuracies, efforts should also be directed towards developing a framework to monitor rivers of all widths at the global scale. Besides, detecting flows over transboundary rivers with reservoirs pose additional challenges. The upcoming SWOT mission (Biancamaria et al., 2016) is anticipated to address these issues.
- The current altimeters have low temporal resolution (in the order of tens of days), which makes it challenging to monitor rivers. One way of overcoming this limitation is to fuse multi-satellite information (Tourian et al., 2013). Furthermore, since most of the altimeters are intended to monitor ocean surface, they have limitations of echoes from land while monitoring inland water bodies (Tarpanelli et al., 2019), which need to be addressed.
- GRACE and GRACE-FO provide valuable information on the terrestrial water storage, which include surface and sub-surface water resources. Efforts should be directed towards downscaling these products for diversifying their applications in the areas of irrigation and drinking water supply, among others.
- Flood monitoring can be further improved with the usage of multiple satellites that alleviate the issues of cloud cover, spatial resolution, and overpass time during the flooding event.
- Quantifying the anatomy of an agricultural drought remains a challenge due to our limited understanding of root zone soil moisture availability for crop growth (Mishra et al., 2015). Therefore, there is a need to improve our understanding of soil moisture signals in different types of environments to improve agricultural water management. The continuous development in remote sensing products (e.g., SMAP, SMOS, AMSR-2, and Sentinel missions), and assimilating them into land surface model can generate root zone soil moisture (Das and Mohanty, 2006; De Lannoy and Reichle, 2016; Li et al., 2010; Liu and Mishra, 2017; Martens et al., 2017; Reichle et al., 2017; Reichle et al., 2019) to improve agricultural drought management. In addition, remote sensing soil moisture products can expand the capability to map soil moisture deficit with global coverage, and it can significantly compliment to the sparse in situ soil moisture networks. The mapping capability of satellite remote sensing products opens a new window on the onset and evolution of droughts at regional to national scale (Mishra et al., 2017).
- There is a need to ingest the information of varying temporal scales at which the hydro-meteorological variables behave while characterizing droughts. For instance, the role of persistence of soil moisture profile on agricultural droughts is yet to be well understood. Remote sensing products can be useful for regional drought assessment in ungagged basins. Remote sensing data should be promoted among the stakeholders to develop regional drought management plans to improve water security by integrating multivariate nature of drought events. This is especially important for data scare regions in many parts of the world.
- Progress in several of the above-mentioned directions requires efforts to develop science to obtain hyper-spatio-temporal-resolution remote sensing products. Projects such as SMOS-HR (High-Resolution) (Rodríguez-Fernández et al., 2019) – which is still at concept stage – may fill this requirement.

CRediT authorship contribution statement

Ila Chawla: Conceptualization, Formal analysis, Investigation, Writing - original draft. **L. Karthikeyan:** Conceptualization, Formal analysis, Investigation, Writing - original draft. **Ashok K. Mishra:** Conceptualization, Formal analysis, Supervision, Writing - review & editing, Funding acquisition.

Declaration of Competing Interest

The authors declare that they have no known competing financial interests or personal relationships that could have appeared to influence the work reported in this paper.

Acknowledgments

This study was supported by the National Science Foundation (NSF, USA) award # 1653841 and 1841629. Authors acknowledge Abhishek Kumar, Azad Patle and Sumant Tyagi (Masters students of CSRE, IIT Bombay) for their assistance in compiling the literature.

References

AghaKouchak, A., 2015. A multivariate approach for persistence-based drought prediction: Application to the 2010–2011 East Africa drought. J. Hydrol. 526, 127–135.
Aguirre-Gomez, R., 2000. Detection of total suspended sediments in the North Sea using AVHRR and ship data. Int. J. Remote Sens. 21, 1583–1596.
Al Shehhi, M.R., Gherboudj, I., Ghedira, H., 2019. Detection of algal blooms over optically complex waters of the Arabian Gulf and Sea of Oman using MODIS fluorescence data. Int. J. Remote Sens. 40, 3751–3771.
Alawadi, F., 2010. Detection of surface algal blooms using the newly developed algorithm surface algal bloom index (SABI). In: Remote Sensing of the Ocean, Sea Ice, and Large Water Regions 2010. International Society for Optics and Photonics, pp. 782506.
Alijanian, M., Reza Rakhshandehroo, G., Mishra, A., Dehghani, M., 2019. Evaluation of remotely sensed precipitation estimates using PERSIANN-CDR and MSWEP for spatiotemporal drought assessment over Iran. J. Hydrol. 579, 124189. https://doi.org/10.1016/j.jhydrol.2019.124189.
Allee, R., Johnson, J., 1999. Use of satellite imagery to estimate surface chlorophyll a and Secchi disc depth of Bull Shoals Reservoir, Arkansas, USA. Int. J. Remote Sens. 20, 1057–1072.
Alparslan, E., Aydöner, C., Tufekci, V., Tüfekci, H., 2007. Water quality assessment at Ömerli Dam using remote sensing techniques. Environ. Monit. Assess. 135, 391.
Alparslan, E., Coskun, H.G., Alganci, U., 2009. Water quality determination of Küçükçekmece Lake, Turkey by using multispectral satellite data. Sci. World J. 9, 1215–1229.
Alsdorf, D., Han, S.-C., Bates, P., Melack, J., 2010. Seasonal water storage on the Amazon floodplain measured from satellites. Remote Sens. Environ. 114, 2448–2456.
Alsdorf, D., Lettenmaier, D., Vörösmarty, C., 2003. The need for global, satellite-based observations of terrestrial surface waters. Eos, Trans. Am. Geophys. Union 84, 269–276.
Alsdorf, D.E., Lettenmaier, D.P., 2003. Tracking fresh water from space. Science 301, 1491–1494.
Anderson, M.C., Hain, C., Wardlow, B., Pimstein, A., Mecikalski, J.R., Kustas, W.P., 2011. Evaluation of drought indices based on thermal remote sensing of evapotranspiration over the continental United States. J. Clim. 24, 2025–2044.
Anderson, M.C., Norman, J.M., Mecikalski, J.R., Otkin, J.A., Kustas, W.P., 2007. A climatological study of evapotranspiration and moisture stress across the continental United States based on thermal remote sensing: 2. Surface moisture climatology. J. Geophys. Res.: Atmos. 112.
Anderson, W., Zaitchik, B., Hain, C., Anderson, M., Yilmaz, M., Mecikalski, J., Schultz, L., 2012. Towards an integrated soil moisture drought monitor for East Africa. Hydrol. Earth Syst. Sci. 16, 2893–2913.
Andreadis, K.M., Schumann, G.J., 2014. Estimating the impact of satellite observations on the predictability of large-scale hydraulic models. Adv. Water Resour. 73, 44–54.
Andreadis, K.M., Clark, E.A., Lettenmaier, D.P., Alsdorf, D.E., 2007. Prospects for river discharge and depth estimation through assimilation of swath-altimetry into a raster-based hydrodynamics model. Geophys. Res. Lett. 34.
Andreadis, K.M., Clark, E.A., Wood, A.W., Hamlet, A.F., Lettenmaier, D.P., 2005. Twentieth-century drought in the conterminous United States. J. Hydrometeorol. 6 (6), 985–1001.
Ashouri, H., Hsu, K.-L., Sorooshian, S., Braithwaite, D.K., Knapp, K.R., Cecil, L.D., Nelson, B.R., Prat, O.P., 2015. PERSIANN-CDR: Daily precipitation climate data record from multisatellite observations for hydrological and climate studies. Bull. Am. Meteorol. Soc. 96, 69–83.
Asoka, A., Gleeson, T., Wada, Y., Mishra, V., 2017. Relative contribution of monsoon precipitation and pumping to changes in groundwater storage in India. Nat. Geosci. 10, 109.
Ayantobo, O.O., Wei, J., 2019. Appraising regional multi-category and multi-scalar drought monitoring using standardized moisture anomaly index (SZI): A water-energy balance approach. J. Hydrol. 579, 124139.
Bachmair, S., Tanguy, M., Hannaford, J., Stahl, K., 2018. How well do meteorological indicators represent agricultural and forest drought across Europe? Environ. Res. Lett. 13, 034042.
Basist, A., Grody, N.C., Peterson, T.C., Williams, C.N., 1998. Using the Special Sensor Microwave/Imager to monitor land surface temperatures, wetness, and snow cover. J. Appl. Meteorol. 37, 888–911.
Bates, P., Horritt, M., Smith, C., Mason, D., 1997. Integrating remote sensing observations of flood hydrology and hydraulic modelling. Hydrol. Process. 11, 1777–1795.
Bates, P.D., Wilson, M.D., Horritt, M.S., Mason, D.C., Holden, N., Currie, A., 2006. Reach scale floodplain inundation dynamics observed using airborne synthetic aperture radar imagery: Data analysis and modelling. J. Hydrol. 328, 306–318.
Bayissa, Y., Tadesse, T., Demisse, G., Shiferaw, A., 2017. Evaluation of satellite-based rainfall estimates and application to monitor meteorological drought for the Upper Blue Nile Basin. Ethiopia. *Remote Sensing* 9, 669.
Bazi, Y., Bruzzone, L., Melgani, F., 2005. An unsupervised approach based on the generalized Gaussian model to automatic change detection in multitemporal SAR images. IEEE Trans. Geosci. Remote Sens. 43, 874–887.
Beck, H.E., Van Dijk, A.I., Levizzani, V., Schellekens, J., Gonzalez Miralles, D., Martens, B., De Roo, A., 2017. MSWEP: 3-hourly 0.25 global gridded precipitation (1979–2015) by merging gauge, satellite, and reanalysis data. Hydrol. Earth Syst. Sci. 21 (1), 589–615.
Beck, H.E., Wood, E.F., Pan, M., Fisher, C.K., Miralles, D.G., Van Dijk, A.I., McVicar, T.R., Adler, R.F., 2019. MSWEP V2 global 3-hourly 0.1° precipitation: methodology and quantitative assessment. Bull. Am. Meteorol. Soc. 100, 473–500.
Berry, P., Garlick, J., Freeman, J., Mathers, E., 2005. Global inland water monitoring from multi-mission altimetry. Geophys. Res. Lett. 32.
Bhattf, A.M., Rundquist, D., Schalles, J., Ramirez, L., 2010. Application of hyperspectral remotely sensed data for water quality monitoring: Accuracy and limitation. In: 9th International Symposium on Spatial Accuracy Assessment in Natural Resources and Environmental Sciences, Accuracy 2010. International Spatial Accuracy Research Association (ISARA), pp. 349–352.
Bhavsar, P., 1984. Review of remote sensing applications in hydrology and water resources management in India. Adv. Space Res. 4, 193–200.
Biancamaria, S., Durand, M., Andreadis, K., Bates, P., Boone, A., Mognard, N., Rodriguez, E., Alsdorf, D., Lettenmaier, D., Clark, E., 2011. Assimilation of virtual wide swath altimetry to improve Arctic river modeling. Remote Sens. Environ. 115, 373–381.
Biancamaria, S., Lettenmaier, D.P., Pavelsky, T.M., 2016. The SWOT mission and its capabilities for land hydrology. In: Remote Sensing and Water Resources. Springer, pp. 117–147.
Bierman, P., Lewis, M., Ostendorf, B., Tanner, J., 2011. A review of methods for analysing spatial and temporal patterns in coastal water quality. Ecol. Ind. 11, 103–114.
Binding, C., Greenberg, T., Bukata, R., 2012. An analysis of MODIS-derived algal and mineral turbidity in Lake Erie. J. Great Lakes Res. 38, 107–116.
Binding, C., Greenberg, T., Bukata, R., 2013. The MERIS maximum chlorophyll index; its merits and limitations for inland water algal bloom monitoring. J. Great Lakes Res. 39, 100–107.
Birkett, C., 1994. Radar altimetry: a new concept in monitoring lake level changes. Eos, Trans. Am. Geophys. Union 75, 273–275.
Birkett, C., 1995a. The contribution of TOPEX/POSEIDON to the global monitoring of climatically sensitive lakes. J. Geophys. Res. Oceans 100, 25179–25204.
Birkett, C., 1995b. The global remote sensing of lakes, wetlands and rivers for hydrological and climate research. In: 1995 International Geoscience and Remote Sensing Symposium, IGARSS'95. Quantitative Remote Sensing for Science and Applications. IEEE, pp. 1979–1981.
Birkett, C., 2000. Synergistic remote sensing of Lake Chad: Variability of basin inundation. Remote Sens. Environ. 72, 218–236.
Birkett, C.M., 1998. Contribution of the TOPEX NASA radar altimeter to the global monitoring of large rivers and wetlands. Water Resour. Res. 34, 1223–1239.
Birkett, C.M., Beckley, B., 2010. Investigating the performance of the Jason-2/OSTM radar altimeter over lakes and reservoirs. Mar. Geod. 33, 204–238.
Birkett, C.M., Mertes, L., Dunne, T., Costa, M., Jasinski, M., 2002. Surface water dynamics in the Amazon Basin: application of satellite radar altimetry. J. Geophys. Res. 107 LBA 26-21-LBA 26-21.
Birkinshaw, S., Moore, P., Kilsby, C., O'donnell, G., Hardy, A.J., & Berry, P, 2014. Daily discharge estimation at ungauged river sites using remote sensing. Hydrol. Process. 28, 1043–1054.
Biswas, N.K., Hossain, F., Bonnema, M., Okeowo, M.A., Lee, H., 2019. An altimeter height extraction technique for dynamically changing rivers of South and South-East Asia. Remote Sens. Environ. 221, 24–37.
Bjerklie, D.M., 2007. Estimating the bankfull velocity and discharge for rivers using remotely sensed river morphology information. J. Hydrol. 341, 144–155.
Bjerklie, D.M., Dingman, S.L., Vorosmarty, C.J., Bolster, C.H., Congalton, R.G., 2003. Evaluating the potential for measuring river discharge from space. J. Hydrol. 278, 17–38.
Bogning, S., Frappart, F., Blarel, F., Niño, F., Mahé, G., Bricquet, J.-P., Seyler, F., Onguéné, R., Etamé, J., Paiz, M.-C., 2018. Monitoring water levels and discharges using radar altimetry in an ungauged river basin: The case of the Ogooué. Remote Sensing 10, 350.
Bonaccorso, B., Peres, D.J., Castano, A., Cancelliere, A., 2015. SPI-based probabilistic analysis of drought areal extent in Sicily. Water Resour. Manage. 29 (2), 459–470.
Bonansea, M., Ledesma, M., Bazán, R., Ferral, A., German, A., O'Mill, P., Rodriguez, C., Pinotti, L., 2019. Evaluating the feasibility of using Sentinel-2 imagery for water clarity assessment in a reservoir. J. S. Am. Earth Sci. 95, 102265.
Bonnema, M., Hossain, F., 2019. Assessing the Potential of the Surface Water and Ocean

Topography Mission for Reservoir Monitoring in the Mekong River Basin. Water Resour. Res. 55, 444–461.
Braga, C.Z.F., Setzer, A.W., de Lacerda, L.D., 1993. Water quality assessment with simultaneous Landsat-5 TM data at Guanabara Bay, Rio de Janeiro, Brazil. Remote Sens. Environ. 45, 95–106.
Brakenridge, G.R., Nghiem, S.V., Anderson, E., Mic, R., 2007. Orbital microwave measurement of river discharge and ice status: MICROWAVE MEASUREMENT OF RIVER DISCHARGE. Water Resour. Res. 43.
Branco, A.B., Kremer, J.N., 2005. The relative importance of chlorophyll and colored dissolved organic matter (CDOM) to the prediction of the diffuse attenuation coefficient in shallow estuaries. Estuaries 28, 643–652.
Brando, V.E., Dekker, A.G., 2003. Satellite hyperspectral remote sensing for estimating estuarine and coastal water quality. IEEE Trans. Geosci. Remote Sens. 41, 1378–1387.
Brezonik, P., Menken, K.D., Bauer, M., 2005. Landsat-based remote sensing of lake water quality characteristics, including chlorophyll and colored dissolved organic matter (CDOM). Lake Reservoir Manage. 21, 373–382.
Brezonik, P.L., 1978. Effect of organic color and turbidity of Secchi disk transparency. J. Fish. Board Canada 35, 1410–1416.
Brivio, P.A., Giardino, C., Zilioli, E., 2001. Determination of chlorophyll concentration changes in Lake Garda using an image-based radiative transfer code for Landsat TM images. Int. J. Remote Sens. 22 (2–3), 487–502.
Brivio, P., Colombo, R., Maggi, M., Tomasoni, R., 2002. Integration of remote sensing data and GIS for accurate mapping of flooded areas. Int. J. Remote Sens. 23, 429–441.
Brown, G., 1977. Skylab S-193 radar experiment analysis and results. NASA report NASA CR, 2763.
Brown, J.F., Wardlow, B.D., Tadesse, T., Hayes, M.J., Reed, B.C., 2008. The Vegetation Drought Response Index (VegDRI): A new integrated approach for monitoring drought stress in vegetation. GI Sci. Remote Sensing 45, 16–46.
Bustamante, J., Pacios, F., Díaz-Delgado, R., Aragonés, D., 2009. Predictive models of turbidity and water depth in the Doñana marshes using Landsat TM and ETM+ images. J. Environ. Manage. 90, 2219–2225.
Büttner, G., Korándi, M., Gyömörei, A., Köte, Z., Szabó, G., 1987. Satellite remote sensing of inland waters: Lake Balaton and reservoir Kisköre. Acta Astronaut. 15, 305–311.
Cai, L., Yu, W., Shao, W., Tang, D., Belkin, I.M., 2019. Satellite observations of suspended sediment near Ningbo North Dyke, China. Adv. Space Res. 64, 1415–1422.
Cai, W., Zhang, Y., Yao, Y., Chen, Q., 2015. Probabilistic analysis of drought spatio-temporal characteristics in the Beijing-Tianjin-Hebei metropolitan area in China. Atmosphere 6 (4), 431–450.
Cao, H., Zhang, H., Wang, C., Zhang, B., 2019a. Operational Flood Detection Using Sentinel-1 SAR Data over Large Areas. Water 11, 786.
Cao, Q., Clark, E.A., Mao, Y., Lettenmaier, D.P., 2019b. Trends and Interannual Variability in Terrestrial Water Storage Over the Eastern United States, 2003–2016. Water Resour. Res. 55, 1928–1950.
Cao, Y., Chen, S., Wang, L., Zhu, B., Lu, T., Yu, Y., 2019c. An Agricultural Drought Index for Assessing Droughts Using a Water Balance Method: A Case Study in Jilin Province. Northeast China. *Remote Sensing* 11, 1066.
Cardenal, S.J.P., Riegels, N., Bauer-Gottwein, P., Berry, P., Smith, R., Yakovlev, A., Siegfried, T., 2011. Real-time remote sensing driven river basin modeling using radar altimetry. Hydrol. Earth Syst. Sci. 15, 241–254.
Carder, K.L., Steward, R.G., Harvey, G.R., Ortner, P.B., 1989. Marine humic and fulvic acids: Their effects on remote sensing of ocean chlorophyll. Limnol. Oceanogr. 34, 68–81.
Carlson, R.E., 1977. A trophic state index for lakes 1. Limnol. Oceanogr. 22, 361–369.
Carrão, H., Russo, S., Sepulcre-Canto, G., Barbosa, P., 2016. An empirical standardized soil moisture index for agricultural drought assessment from remotely sensed data. Int. J. Appl. Earth Obs. Geoinf. 48, 74–84.
Caselles, V., Catté, F., Coll, T., Dibos, F., 1993. A geometric model for active contours in image processing. Numer. Math. 66, 1–31.
Castellazzi, P., Longuevergne, L., Martel, R., Rivera, A., Brouard, C., Chaussard, E., 2018. Quantitative mapping of groundwater depletion at the water management scale using a combined GRACE/InSAR approach. Remote Sens. Environ. 205, 408–418.
Castle, S.L., Thomas, B.F., Reager, J.T., Rodell, M., Swenson, S.C., Famiglietti, J.S., 2014. Groundwater depletion during drought threatens future water security of the Colorado River Basin. Geophys. Res. Lett. 41, 5904–5911.
Chan, T.F., Vese, L.A., 2001. Active contours without edges. IEEE Trans. Image Process. 10, 266–277.
Chang, C.-H., Lee, H., Hossain, F., Basnayake, S., Jayasinghe, S., Chishtie, F., Saah, D., Yu, H., Sothea, K., Du Bui, D., 2019. A model-aided satellite-altimetry-based flood forecasting system for the Mekong River. Environ. Modell. Software 112, 112–127.
Chang, L.-C., Shen, H.-Y., Wang, Y.-F., Huang, J.-Y., Lin, Y.-T., 2010. Clustering-based hybrid inundation model for forecasting flood inundation depths. J. Hydrol. 385, 257–268.
Chen, J., Zhu, W., Zheng, Y., Tian, Y.Q., Yu, Q., 2019. Monitoring seasonal variations of colored dissolved organic matter for the Saginaw River based on Landsat-8 data. Water Sci. Technol. Water Supply 19, 274–281.
Chawla, I., Mujumdar, P.P., 2015. Isolating the impacts of land use and climate change on streamflow. Hydrol. Earth Syst. Sci. 19 (8), 3633–3651.
Chawla, I, Mujumdar, P.P., 2017. Partitioning uncertainty in streamflow projections under nonstationary model conditions. Adv. Water Res. 112, 266–282.
Chen, Z., Li, Y., Pan, J., 2004. Distributions of colored dissolved organic matter and dissolved organic carbon in the Pearl River Estuary, China. Cont. Shelf Res. 24, 1845–1856.
Chen, Z., Muller-Karger, F.E., Hu, C., 2007. Remote sensing of water clarity in Tampa Bay. Remote Sens. Environ. 109, 249–259.
Cheng, H., Chen, Y.-H., Sun, Y., 1999. A novel fuzzy entropy approach to image enhancement and thresholding. Signal Process. 75, 277–301.
Chini, M., Hostache, R., Giustarini, L., Matgen, P., 2017. A hierarchical split-based approach for parametric thresholding of SAR images: Flood inundation as a test case. IEEE Trans. Geosci. Remote Sens. 55, 6975–6988.
Chipman, J.W., Lillesand, T.M., Schmaltz, J.E., Leale, J.E., Nordheim, M.J., 2004. Mapping lake water clarity with Landsat images in Wisconsin, USA. Canadian J. Remote Sensing 30, 1–7.
Cho, S., Haralick, R., Yi, S., 1989. Improvement of Kittler and Illingworth's minimum error thresholding. Pattern Recogn. 22, 609–617.
Choubey, V., 1998. Laboratory experiment, field and remotely sensed data analysis for the assessment of suspended solids concentration and secchi depth of the reservoir surface water. Int. J. Remote Sens. 19, 3349–3360.
Choudhury, B.J., 1989. Monitoring global land surface using Nimbus-7 37 GHz data theory and examples. Int. J. Remote Sens. 10, 1579–1605.
Coe, M.T., Birkett, C.M., 2004. Calculation of river discharge and prediction of lake height from satellite radar altimetry: Example for the Lake Chad basin. Water Resour. Res. 40.
Cohen, L.D., 1991. On active contour models and balloons. CVGIP: Image Understanding 53, 211–218.
Costa, J.E., Cheng, R.T., Haeni, F.P., Melcher, N., Spicer, K.R., Hayes, E., Plant, W., Hayes, K., Teague, C., Barrick, D., 2006. Use of radars to monitor stream discharge by noncontact methods. Water Resour. Res. 42.
Cottrell, R.S., Nash, K.L., Halpern, B.S., Remenyi, T.A., Corney, S.P., Fleming, A., Fulton, E.A., Hornborg, S., Johne, A., Watson, R.A., 2019. Food production shocks across land and sea. Nat. Sustainability 2, 130.
Covello, F., Battazza, F., Coletta, A., Lopinto, E., Fiorentino, C., Pietranera, L., Valentini, G., Zoffoli, S., 2010. COSMO-SkyMed an existing opportunity for observing the Earth. J. Geodyn. 49, 171–180.
Crist, E.P., 1985. A TM tasseled cap equivalent transformation for reflectance factor data. Remote Sens. Environ. 17, 301–306.
Crist, E.P., Cicone, R.C., 1984. A physically-based transformation of Thematic Mapper data–-The TM Tasseled Cap. IEEE Trans. Geosci. Remote Sens. 256–263.
Crowley, J.W., Mitrovica, J.X., Bailey, R.C., Tamisiea, M.E., Davis, J.L., 2006. Land water storage within the Congo Basin inferred from GRACE satellite gravity data. Geophys. Res. Lett. 33.
Da Silva, J.S., Calmant, S., Seyler, F., Rotunno Filho, O.C., Cochonneau, G., Mansur, W.J., 2010. Water levels in the Amazon basin derived from the ERS 2 and ENVISAT radar altimetry missions. Remote Sens. Environ. 114, 2160–2181.
De Lannoy, G.J., Reichle, R.H., 2016. Global assimilation of multiangle and multi-polarization SMOS brightness temperature observations into the GEOS-5 catchment land surface model for soil moisture estimation. J. Hydrometeorol. 17 (2), 669–691.
Dabanlı, İ., Mishra, A.K., Şen, Z., 2017. Long-term spatio-temporal drought variability in Turkey. J. Hydrol. 552, 779–792.
Dalezios, N., Blanta, A., Spyropoulos, N., 2012. Assessment of remotely sensed drought features in vulnerable agriculture. Nat. Hazards Earth Syst. Sci. 12, 3139–3150.
Dall'Olmo, G., Gitelson, A.A., 2005. Effect of bio-optical parameter variability on the remote estimation of chlorophyll-a concentration in turbid productive waters: experimental results. Appl. Opt. 44, 412–422.
Das, N.N., Mohanty, B.P., 2006. Root zone soil moisture assessment using remote sensing and vadose zone modeling. Vadose Zone J. 5 (1), 296–307.
Dasgupta, A., Grimaldi, S., Ramsankaran, R., Pauwels, V.R., Walker, J.P., 2018. Towards operational SAR-based flood mapping using neuro-fuzzy texture-based approaches. Remote Sens. Environ. 215, 313–329.
Davies-Colley, R., Smith, D., 2001. Turbidity suspeni) ed sediment, and water clarity: a review 1. JAWRA J. Am. Water Resour. Assoc. 37, 1085–1101.
De Linage, C., Famiglietti, J., Randerson, J., 2014. Statistical prediction of terrestrial water storage changes in the Amazon Basin using tropical Pacific and North Atlantic sea surface temperature anomalies.
De Roo, A., Van Der Knijff, J., Horritt, M., Schmuck, G., De Jong, S., 1999. Assessing flood damages of the 1997 Oder flood and the 1995 Meuse flood. In: Proceedings of the Second International ITC Symposium on Operationalization of Remote Sensing, Enschede. The Netherlands, pp. 16–20.
Debusscher, B., Van Coillie, F., 2019. Object-based flood analysis using a graph-based representation. Remote Sensing 11, 1883.
Dekker, A., Peters, S., 1993. The use of the Thematic Mapper for the analysis of eutrophic lakes: a case study in the Netherlands. Int. J. Remote Sens. 14, 799–821.
Dekker, A., Malthus, T., Hoogenboom, H., 1995. The remote sensing of inland water quality. Adv. Environ. Remote Sensing 1995, 123–142.
Delpla, I., Jung, A.-V., Baures, E., Clement, M., Thomas, O., 2009. Impacts of climate change on surface water quality in relation to drinking water production. Environ. Int. 35, 1225–1233.
Di Baldassarre, G., Schumann, G., Brandimarte, L., Bates, P., 2011. Timely low resolution SAR imagery to support floodplain modelling: a case study review. Surv. Geophys. 32, 255–269.
Di, L., Rundquist, D.C., Han, L., 1994. Modelling relationships between NDVI and precipitation during vegetative growth cycles. Int. J. Remote Sens. 15, 2121–2136.
Dibarboure, G., Renaudie, C., Pujol, M.-I., Labroue, S., Picot, N., 2012. A demonstration of the potential of Cryosat-2 to contribute to mesoscale observation. Adv. Space Res. 50, 1046–1061.
Dogliotti, A.I., Ruddick, K., Nechad, B., Doxaran, D., Knaeps, E., 2015. A single algorithm to retrieve turbidity from remotely-sensed data in all coastal and estuarine waters. Remote Sens. Environ. 156, 157–168.
Döll, P., Mueller Schmied, H., Schuh, C., Portmann, F.T., Eicker, A., 2014. Global-scale assessment of groundwater depletion and related groundwater abstractions: Combining hydrological modeling with information from well observations and GRACE satellites. Water Resour. Res. 50, 5698–5720.

Domeneghetti, A., Tarpanelli, A., Grimaldi, L., Brath, A., Schumann, G., 2018. Flow duration curve from satellite: potential of a lifetime SWOT mission. Remote Sensing 10, 1107.
Doña, C., Chang, N.-B., Caselles, V., Sánchez, J.M., Camacho, A., Delegido, J., Vannah, B.W., 2015. Integrated satellite data fusion and mining for monitoring lake water quality status of the Albufera de Valencia in Spain. J. Environ. Manage. 151, 416–426.
Doña, C., Sánchez, J.M., Caselles, V., Domínguez, J.A., Camacho, A., 2014. Empirical relationships for monitoring water quality of lakes and reservoirs through multispectral images. IEEE J. Sel. Top. Appl. Earth Obs. Remote Sens. 7, 1632–1641.
Donlon, C., Berruti, B., Buongiorno, A., Ferreira, M.-H., Féménias, P., Frerick, J., Goryl, P., Klein, U., Laur, H., Mavrocordatos, C., 2012. The global monitoring for environment and security (GMES) sentinel-3 mission. Remote Sens. Environ. 120, 37–57.
Doxaran, D., Froidefond, J.-M., Lavender, S., Castaing, P., 2002. Spectral signature of highly turbid waters: Application with SPOT data to quantify suspended particulate matter concentrations. Remote Sens. Environ. 81, 149–161.
Drusch, M., Del Bello, U., Carlier, S., Colin, O., Fernandez, V., Gascon, F., Hoersch, B., Isola, C., Laberinti, P., Martimort, P., 2012. Sentinel-2: ESA's optical high-resolution mission for GMES operational services. Remote Sens. Environ. 120, 25–36.
D'Sa, E.J., 2008. Colored dissolved organic matter in coastal waters influenced by the Atchafalaya River, USA: Effects of an algal bloom. J. Appl. Remote Sens. 2, 023502.
Dubey, A.K., Gupta, P., Dutta, S., Singh, R.P., 2015. Water level retrieval using SARAL/AltiKa observations in the Braided Brahmaputra river, Eastern India. Mar. Geod. 38, 549–567.
Durand, M., Andreadis, K.M., Alsdorf, D.E., Lettenmaier, D.P., Moller, D., Wilson, M., 2008. Estimation of bathymetric depth and slope from data assimilation of swath altimetry into a hydrodynamic model. Geophys. Res. Lett. 35.
Durand, M., Gleason, C., Garambois, P.-A., Bjerklie, D., Smith, L., Roux, H., Rodriguez, E., Bates, P.D., Pavelsky, T.M., Monnier, J., 2016. An intercomparison of remote sensing river discharge estimation algorithms from measurements of river height, width, and slope. Water Resour. Res. 52, 4527–4549.
Durand, M., Neal, J., Rodríguez, E., Andreadis, K.M., Smith, L.C., Yoon, Y., 2014. Estimating reach-averaged discharge for the River Severn from measurements of river water surface elevation and slope. J. Hydrol. 511, 92–104.
Eicker, A., Schumacher, M., Kusche, J., Döll, P., Schmied, H.M., 2014. Calibration/data assimilation approach for integrating GRACE data into the WaterGAP Global Hydrology Model (WGHM) using an ensemble Kalman filter: First results. Surv. Geophys. 35, 1285–1309.
Ekercin, S., 2007. Water quality retrievals from high resolution IKONOS multispectral imagery: A case study in Istanbul, Turkey. Water Air Soil Pollut. 183, 239–251.
Elagib, N.A., 2013. Meteorological drought and crop yield in Sub-Saharan Sudan. Water Resour. Arid Environ 3, 164–171.
Emery, C.M., Paris, A., Biancamaria, S., Boone, A., Calmant, S., Garambois, P.-A., Da Silva, J.S., 2017. Large scale hydrological model river storage and discharge correction using satellite altimetry-based discharge product. Hydrol. Earth Syst. Sci. Discuss. 22, 2135–2162.
Epiphanio, J.N., Huete, A.R., 1995. Dependence of NDVI and SAVI on sun/sensor geometry and its effect on fAPAR relationships in Alfalfa. Remote Sens. Environ. 51, 351–360.
Famiglietti, J.S., Lo, M., Ho, S.L., Bethune, J., Anderson, K., Syed, T.H., Swenson, S.C., de Linage, C.R., Rodell, M., 2011. Satellites measure recent rates of groundwater depletion in California's Central Valley. Geophys. Res. Lett. 38.
Feng, L., Hu, C., Chen, X., Tian, L., Chen, L., 2012. Human induced turbidity changes in Poyang Lake between 2000 and 2010: Observations from MODIS. J. Geophys. Res. Oceans 117.
Feng, L., Hu, C., Han, X., Chen, X., Qi, L., 2015. Long-term distribution patterns of chlorophyll-a concentration in China's largest freshwater lake: MERIS full-resolution observations with a practical approach. Remote Sensing 7, 275–299.
Feng, W., Zhong, M., Lemoine, J.M., Biancale, R., Hsu, H.T., Xia, J., 2013. Evaluation of groundwater depletion in North China using the Gravity Recovery and Climate Experiment (GRACE) data and ground-based measurements. Water Resour. Res. 49, 2110–2118.
Feyisa, G.L., Meilby, H., Fensholt, R., Proud, S.R., 2014. Automated Water Extraction Index: A new technique for surface water mapping using Landsat imagery. Remote Sens. Environ. 140, 23–35.
Fisher, A., Flood, N., Danaher, T., 2016. Comparing Landsat water index methods for automated water classification in eastern Australia. Remote Sens. Environ. 175, 167–182.
Flechtner, F., Morton, P., Watkins, M., Webb, F., 2014. Status of the GRACE follow-on mission. In: Gravity, geoid and height systems. Springer, pp. 117–121.
Forootan, E., Khaki, M., Schumacher, M., Wulfmeyer, V., Mehrnegar, N., Van Dijk, A., Brocca, L., Farzaneh, S., Akinluyi, F., Ramillien, G., 2019. Understanding the global hydrological droughts of 2003–2016 and their relationships with teleconnections. Sci. Total Environ. 650, 2587–2604.
Forootan, E., Rietbroek, R., Kusche, J., Sharifi, M., Awange, J., Schmidt, M., Omondi, P., Famiglietti, J., 2014. Separation of large scale water storage patterns over Iran using GRACE, altimetry and hydrological data. Remote Sens. Environ. 140, 580–595.
Frappart, F., Ramillien, G., 2018. Monitoring groundwater storage changes using the Gravity Recovery and Climate Experiment (GRACE) satellite mission: a review. Remote Sensing 10, 829.
Frappart, F., Minh, K.D., L'Hermitte, J., Cazenave, A., Ramillien, G., Le Toan, T., Mognard-Campbell, N., 2006. Water volume change in the lower Mekong from satellite altimetry and imagery data. Geophys. J. Int. 167, 570–584.
Frappart, F., Seyler, F., Martinez, J.-M., León, J.G., Cazenave, A., 2005. Floodplain water storage in the Negro River basin estimated from microwave remote sensing of inundation area and water levels. Remote Sens. Environ. 99, 387–399.
Freeman, A., Durden, S.L., 1998. A three-component scattering model for polarimetric SAR data. IEEE Trans. Geosci. Remote Sens. 36, 963–973.
Funk, C., Peterson, P., Landsfeld, M., Pedreros, D., Verdin, J., Shukla, S., Husak, G., Rowland, J., Harrison, L., Hoell, A., 2015. The climate hazards infrared precipitation with stations—a new environmental record for monitoring extremes. Sci. Data 2, 150066.
Funk, C., Shukla, S., Thiaw, W.M., Rowland, J., Hoell, A., McNally, A., Husak, G., Novella, N., Budde, M., Peters-Lidard, C., 2019. Recognizing the Famine Early Warning Systems Network (FEWS NET): Over 30 Years of Drought Early Warning Science Advances and Partnerships Promoting Global Food Security. Bull. Am. Meteorol. Soc.
Gallant, J.C., Dowling, T.I., 2003. A multiresolution index of valley bottom flatness for mapping depositional areas. Water Resour. Res. 39.
Gan, T., Kalinga, O., Ohgushi, K., Araki, H., 2004. Retrieving seawater turbidity from Landsat TM data by regressions and an artificial neural network. Int. J. Remote Sens. 25, 4593–4615.
Gao, H., Birkett, C., Lettenmaier, D.P., 2012. Global monitoring of large reservoir storage from satellite remote sensing. Water Resour. Res. 48.
Garambois, P.-A., Monnier, J., 2015. Inference of effective river properties from remotely sensed observations of water surface. Adv. Water Resour. 79, 103–120.
Getirana, A., Rodell, M., Kumar, S., Beaudoing, H.K., Arsenault, K., Zaitchik, B., Save, H., Bettadpur, S., 2019. GRACE improves seasonal groundwater forecast initialization over the US. J. Hydrometeorol.
Geudtner, D., Torres, R., Snoeij, P., Davidson, M., Rommen, B., 2014. Sentinel-1 system capabilities and applications. In: 2014 IEEE Geoscience and Remote Sensing Symposium. IEEE, pp. 1457–1460.
Gholizadeh, M.H., Melesse, A.M., Reddi, L., 2016. A comprehensive review on water quality parameters estimation using remote sensing techniques. Sensors 16, 1298.
Ghosh, S., Kumar Thakur, P., Garg, V., Nandy, S., Aggarwal, S., Saha, S.K., Sharma, R., Bhattacharyya, S., 2015. SARAL/AltiKa waveform analysis to monitor inland water levels: a case study of Maithon reservoir, Jharkhand, India. Mar. Geod. 38, 597–613.
Giardino, C., Brando, V.E., Dekker, A.G., Strömbeck, N., Candiani, G., 2007. Assessment of water quality in Lake Garda (Italy) using Hyperion. Remote Sens. Environ. 109, 183–195.
Giardino, C., Pepe, M., Brivio, P.A., Ghezzi, P., Zilioli, E., 2001. Detecting chlorophyll, Secchi disk depth and surface temperature in a sub-alpine lake using Landsat imagery. Sci. Total Environ. 268, 19–29.
Gikas, G.D., Tsihrintzis, V.A., Akratos, C.S., Haralambidis, G., 2009. Water quality trends in Polyphytos reservoir, Aliakmon river, Greece. Environ. Monit. Assess. 149, 163–181.
Gikas, G.D., Yiannakopoulou, T., Tsihrintzis, V.A., 2006. Water quality trends in a coastal lagoon impacted by non-point source pollution after implementation of protective measures. Hydrobiologia 563, 385–406.
Girotto, M., Reichle, R.H., Rodell, M., Liu, Q., Mahanama, S., De Lannoy, G.J., 2019. Multi-sensor assimilation of SMOS brightness temperature and GRACE terrestrial water storage observations for soil moisture and shallow groundwater estimation. Remote Sens. Environ. 227, 12–27.
Gitelson, A.A., Gritz, Y., Merzlyak, M.N., 2003. Relationships between leaf chlorophyll content and spectral reflectance and algorithms for non-destructive chlorophyll assessment in higher plant leaves. J. Plant Physiol. 160, 271–282.
Giustarini, L., Hostache, R., Kavetski, D., Chini, M., Corato, G., Schlaffer, S., Matgen, P., 2016. Probabilistic flood mapping using synthetic aperture radar data. IEEE Trans. Geosci. Remote Sens. 54, 6958–6969.
Giustarini, L., Hostache, R., Matgen, P., Schumann, G.J.-P., Bates, P.D., Mason, D.C., 2012. A change detection approach to flood mapping in urban areas using TerraSAR-X. IEEE Trans. Geosci. Remote Sens. 51, 2417–2430.
Glasgow, H.B., Burkholder, J.M., Reed, R.E., Lewitus, A.J., Kleinman, J.E., 2004. Real-time remote monitoring of water quality: a review of current applications, and advancements in sensor, telemetry, and computing technologies. J. Exp. Mar. Biol. Ecol. 300, 409–448.
Gleason, C.J., Smith, L.C., 2014. Toward global mapping of river discharge using satellite images and at-many-stations hydraulic geometry. Proc. Natl. Acad. Sci. 111, 4788–4791.
Gohin, F., Van der Zande, D., Tilstone, G., Eleveld, M.A., Lefebvre, A., Andrieux-Loyer, F., Blauw, A.N., Bryère, P., Devreker, D., Garnesson, P., 2019. Twenty years of satellite and in situ observations of surface chlorophyll-a from the northern Bay of Biscay to the eastern English Channel. Is the water quality improving? Remote Sens. Environ. 233, 111343.
Golian, S., Javadian, M., Behrangi, A., 2019. On the use of satellite, gauge, and reanalysis precipitation products for drought studies. Environ. Res. Lett.
Gonçalves, R.D., Stollberg, R., Weiss, H., Chang, H.K., 2019. Using GRACE to quantify the depletion of terrestrial water storage in Northeastern Brazil: The Urucuia Aquifer System. Sci. Total Environ 135845.
Gons, H.J., Rijkeboer, M., Ruddick, K.G., 2005. Effect of a waveband shift on chlorophyll retrieval from MERIS imagery of inland and coastal waters. J. Plankton Res. 27, 125–127.
Goodin, D.G., Harrington Jr, J.A., Nellis, M.D., & Rundquist, D.C., 1996. Mapping Reservoir Turbidity Patterns Using SPOT-HRV Data.
Green, S.A., Blough, N.V., 1994. Optical absorption and fluorescence properties of chromophoric dissolved organic matter in natural waters. Limnol. Oceanogr. 39, 1903–1916.
Grimaldi, S., Li, Y., Pauwels, V.R., Walker, J.P., 2016. Remote sensing-derived water extent and level to constrain hydraulic flood forecasting models: Opportunities and challenges. Surv. Geophys. 37, 977–1034.
Guerschman, J.P., Warren, G., Byrne, G., Lymburner, L., Mueller, N., Van-Dijk, A., 2011. MODIS-based standing water detection for flood and large reservoir mapping: algorithm development and applications for the Australian continent. Water for a Healthy

Country National Research Flagship Report, Canberra.
Guo, R., Pandit, S., 1998. Automatic threshold selection based on histogram modes and a discriminant criterion. Mach. Vis. Appl. 10, 331–338.
Gupta, P., Dubey, A.K., Goswami, N., Singh, R.P., Chauhan, P., 2015. Use of SARAL/AltiKa observations for modeling river flow. Mar. Geod. 38, 614–625.
Hakvoort, H., De Haan, J., Jordans, R., Vos, R., Peters, S., Rijkeboer, M., 2002. Towards airborne remote sensing of water quality in The Netherlands—validation and error analysis. ISPRS J. Photogramm. Remote Sens. 57, 171–183.
Hallack-Alegria, M., Watkins Jr, D.W., 2007. Annual and warm season drought intensity–duration–frequency analysis for Sonora, Mexico. J. Clim. 20 (9), 1897–1909.
Hamilton, S., Sippel, S., Melack, J., 1996. Inundation patterns in the Pantanal wetland of South America determined from passive microwave remote sensing. Archiv für Hydrobiologie 137, 1–23.
Hao, Z., Singh, V.P., 2015. Drought characterization from a multivariate perspective: A review. J. Hydrol. 527, 668–678.
Hao, Z., Singh, V.P., Xia, Y., 2018. Seasonal drought prediction: advances, challenges, and future prospects. Rev. Geophys. 56, 108–141.
Harding, L., Itsweire, E., Esaias, W., 1995. Algorithm development for recovering chlorophyll concentrations in the Chesapeake Bay using aircraft remote sensing, 1989–91. Oceanographic Literature Rev. 10, 907–908.
Härmä, P., Vepsäläinen, J., Hannonen, T., Pyhälahti, T., Kämäri, J., Kallio, K., Eloheimo, K., Koponen, S., 2001. Detection of water quality using simulated satellite data and semi-empirical algorithms in Finland. Sci. Total Environ. 268, 107–121.
Harrington Jr, J.A., Schiebe, F.R., Nix, J.F., 1992. Remote sensing of Lake Chicot, Arkansas: Monitoring suspended sediments, turbidity, and Secchi depth with Landsat MSS data. Remote Sens. Environ. 39, 15–27.
He, Q., Qiu, Y., Liu, H., Sun, X., Kang, L., Cao, L., Li, H., Ai, H., 2017. New insights into the impacts of suspended particulate matter on phytoplankton density in a tributary of the Three Gorges Reservoir, China. Sci. Rep. 7, 13518.
Heddam, S., 2016. Secchi disk depth estimation from water quality parameters: artificial neural network versus multiple linear regression models? Environ. Process. 3, 525–536.
Heim, R., 2000. Drought Indices. A Review In: Drought A Global Assessment, Hazards Disaster Series. Routledge, New York.
Hellweger, F., Schlosser, P., Lall, U., Weissel, J., 2004. Use of satellite imagery for water quality studies in New York Harbor. Estuar. Coast. Shelf Sci. 61, 437–448.
Hertz, L., Schafer, R.W., 1988. Multilevel thresholding using edge matching. Computer Vision, Graphics, Image Process. 44, 279–295.
Hirtle, H., Rencz, A., 2003. The relation between spectral reflectance and dissolved organic carbon in lake water: Kejimkujik National Park, Nova Scotia, Canada. Int. J. Remote Sens. 24, 953–967.
Hisdal, H., Stahl, K., Tallaksen, L.M., Demuth, S., 2001. Have streamflow droughts in Europe become more severe or frequent? Int. J. Climatol. 21 (3), 317–333.
Hoge, F.E., Williams, M.E., Swift, R.N., Yungel, J.K., Vodacek, A., 1995. Satellite retrieval of the absorption coefficient of chromophoric dissolved organic matter in continental margins. J. Geophys. Res. Oceans 100, 24847–24854.
Hoogenboom, H., Dekker, A., Althuis, I.A., 1998. Simulation of AVIRIS sensitivity for detecting chlorophyll over coastal and inland waters. Remote Sens. Environ. 65, 333–340.
Horritt, M., 1999. A statistical active contour model for SAR image segmentation. Image Vis. Comput. 17, 213–224.
Horritt, M., Mason, D., Luckman, A., 2001. Flood boundary delineation from synthetic aperture radar imagery using a statistical active contour model. Int. J. Remote Sens. 22, 2489–2507.
Hossain, F., Maswood, M., Siddique-E-Akbor, A., Yigzaw, W., Mazumdar, L.C., Ahmed, T., Hossain, M., Shah-Newaz, S., Limaye, A., Lee, H., 2014. A promising radar altimetry satellite system for operational flood forecasting in flood-prone Bangladesh. IEEE Geosci. Remote Sens. Mag. 2, 27–36.
Hostache, R., Matgen, P., Wagner, W., 2012. Change detection approaches for flood extent mapping: How to select the most adequate reference image from online archives? Int. J. Appl. Earth Obs. Geoinf. 19, 205–213.
Houghton, J.T., Ding, Y., Griggs, D.J., Noguer, M., van der Linden, P.J., Dai, X., Maskell, K., Johnson, C., 2001. Climate change 2001: the scientific basis. The Press Syndicate of the University of Cambridge.
Hsu, K.-L., Gao, X., Sorooshian, S., Gupta, H.V., 1997. Precipitation estimation from remotely sensed information using artificial neural networks. J. Appl. Meteorol. 36, 1176–1190.
Huang, C., Chen, Y., Zhang, S., Wu, J., 2018. Detecting, extracting, and monitoring surface water from space using optical sensors: A review. Rev. Geophys. 56, 333–360.
Huang, Z., Pan, Y., Gong, H., Yeh, P.J.F., Li, X., Zhou, D., Zhao, W., 2015. Subregional-scale groundwater depletion detected by GRACE for both shallow and deep aquifers in North China Plain. Geophys. Res. Lett. 42, 1791–1799.
Huete, A.R., 1988. A soil-adjusted vegetation index (SAVI). Remote Sens. Environ. 25, 295–309.
Hunt, E.D., Hubbard, K.G., Wilhite, D.A., Arkebauer, T.J., Dutcher, A.L., 2009. The development and evaluation of a soil moisture index. Int. J. Climatol.: J. R. Meteorolog. Soc. 29, 747–759.
Hunter, P.D., Tyler, A.N., Carvalho, L., Codd, G.A., Maberly, S.C., 2010. Hyperspectral remote sensing of cyanobacterial pigments as indicators for cell populations and toxins in eutrophic lakes. Remote Sens. Environ. 114, 2705–2718.
Huntington, T.G., 2006. Evidence for intensification of the global water cycle: review and synthesis. J. Hydrol. 319, 83–95.
Huovinen, P., Ramírez, J., Caputo, L., Gómez, I., 2019. Mapping of spatial and temporal variation of water characteristics through satellite remote sensing in Lake Panguipulli, Chile. Sci. Total Environ. 679, 196–208.
Huss, M., Hock, R., 2018. Global-scale hydrological response to future glacier mass loss. Nat. Clim. Change 8, 135.
IPCC (Intergovernmental Panel on Climate Change), 2019. Climate Change and Land: An IPCC Special Report on climate change, desertification, land degradation, sustainable land management, food security, and greenhouse gas fluxes in terrestrial ecosystems. https://www.ipcc.ch/report/srccl/.
Jarihani, A.A., Callow, J.N., Johansen, K., Gouweleeuw, B., 2013. Evaluation of multiple satellite altimetry data for studying inland water bodies and river floods. J. Hydrol. 505, 78–90.
Jawahar, C., Biswas, P.K., Ray, A., 1997. Investigations on fuzzy thresholding based on fuzzy clustering. Pattern Recogn. 30, 1605–1613.
Jiang, H., Feng, M., Zhu, Y., Lu, N., Huang, J., Xiao, T., 2014. An automated method for extracting rivers and lakes from Landsat imagery. Remote Sensing 6, 5067–5089.
Jing, W., Zhao, X., Yao, L., Jiang, H., Xu, J., Yang, J., Li, Y., 2020. Variations in terrestrial water storage in the Lancang-Mekong river basin from GRACE solutions and land surface model. J. Hydrol. 580, 124258.
Juhls, B., Overduin, P.P., Hölemann, J., Hieronymi, M., Matsuoka, A., Heim, B., Fischer, J., 2019. Dissolved organic matter at the fluvial–marine transition in the Laptev Sea using in situ data and ocean colour remote sensing. Biogeosciences 16, 2693–2713.
Kahru, M., Mitchell, B.G., 2001. Seasonal and nonseasonal variability of satellite-derived chlorophyll and colored dissolved organic matter concentration in the California Current. J. Geophys. Res. Oceans 106, 2517–2529.
Kao, S.-C., Govindaraju, R.S., 2010. A copula-based joint deficit index for droughts. J. Hydrol. 380, 121–134.
Kapur, J.N., Sahoo, P.K., Wong, A.K., 1985. A new method for gray-level picture thresholding using the entropy of the histogram. Computer Vision, Graphics, Image Process. 29, 273–285.
Karaska, M.A., Huguenin, R.L., Beacham, J.L., Wang, M.-H., Jensen, J.R., Kaufmann, R.S., 2004. AVIRIS measurements of chlorophyll, suspended minerals, dissolved organic carbon, and turbidity in the Neuse River, North Carolina. Photogramm. Eng. Remote Sens. 70, 125–133.
Karthikeyan, L., Pan, M., Wanders, N., Nagesh Kumar, D., Wood, E.F., 2017. Four decades of microwave satellite soil moisture observations: Part 1. A review of retrieval algorithms. Adv. Water Res. 109, 106–120.
Kass, M., Witkin, A., Terzopoulos, D., 1988. Snakes: Active contour models. Int. J. Comput. Vision 1, 321–331.
Keyantash, J., Dracup, J.A., 2002. The quantification of drought: an evaluation of drought indices. Bull. Am. Meteorol. Soc. 83, 1167–1180.
Khaki, M., Forootan, E., Kuhn, M., Awange, J., Papa, F., Shum, C., 2018a. A study of Bangladesh's sub-surface water storages using satellite products and data assimilation scheme. Sci. Total Environ. 625, 963–977.
Khaki, M., Forootan, E., Kuhn, M., Awange, J., van Dijk, A., Schumacher, M., Sharifi, M., 2018b. Determining water storage depletion within Iran by assimilating GRACE data into the W3RA hydrological model. Adv. Water Resour. 114, 1–18.
Kim, D., Rhee, J., 2016. A drought index based on actual evapotranspiration from the Bouchet hypothesis. Geophys. Res. Lett., 43, 10,277-210,285.
Kim, D., Yu, H., Lee, H., Beighley, E., Durand, M., Alsdorf, D.E., Hwang, E., 2019. Ensemble learning regression for estimating river discharges using satellite altimetry data: Central Congo River as a Test-bed. Remote Sens. Environ. 221, 741–755.
Kim, S.-I., Kim, H.-C., Hyun, C.-U., 2014. High resolution ocean color products estimation in Fjord of Svalbard, arctic sea using Landsat-8 oli. Korean J. Remote Sensing 30, 809–816.
Kloiber, S.M., Brezonik, P.L., Bauer, M.E., 2002a. Application of Landsat imagery to regional-scale assessments of lake clarity. Water Res. 36, 4330–4340.
Kloiber, S.M., Brezonik, P.L., Olmanson, L.G., Bauer, M.E., 2002b. A procedure for regional lake water clarity assessment using Landsat multispectral data. Remote Sens. Environ. 82, 38–47.
Koblinsky, C.J., Clarke, R.T., Brenner, A., Frey, H., 1993. Measurement of river level variations with satellite altimetry. Water Resour. Res. 29, 1839–1848.
Kogan, F., 1990. Remote sensing of weather impacts on vegetation in non-homogeneous areas. Int. J. Remote Sens. 11, 1405–1419.
Kogan, F.N., 1995. Application of vegetation index and brightness temperature for drought detection. Adv. Space Res. 15, 91–100.
Kogan, F.N., 1997. Global drought watch from space. Bull. Am. Meteorol. Soc. 78, 621–636.
Kondo, H., Seo, N., Yasuda, T., Hasizume, M., Koido, Y., Ninomiya, N., Yamamoto, Y., 2002. Post-flood—infectious diseases in Mozambique. Prehospital Disaster Med. 17, 126–133.
Koponen, S., Pulliainen, J., Kallio, K., Hallikainen, M., 2002. Lake water quality classification with airborne hyperspectral spectrometer and simulated MERIS data. Remote Sens. Environ. 79, 51–59.
Kugler, Z., De Groeve, T., 2007. The global flood detection system. Office for Official Publications of the European Communities, Luxembourg.
Kumar, R., Sharma, R., Singh, R., Gupta, P., Oza, S.R., 2017. SARAL/AltiKa Mission: Applications Using Ka-band Altimetry. Proc. Natl. Acad. Sci., India, Sect. A 87, 581–592.
Kumar, U.M., Sasamal, S., Swain, D., Reddy, N.N., Ramanjappa, T., 2015. Intercomparison of geophysical parameters from saral/altika and jason-2 altimeters. IEEE J. Sel. Top. Appl. Earth Obs. Remote Sens. 8, 4863–4870.
Kuo, C.-Y., Kao, H.-C., 2011. Retracked Jason-2 altimetry over small water bodies: Case study of Bajhang River. Taiwan. *Marine Geodesy* 34, 382–392.
Kurnik, B., Barbosa, P., Vogt, J., 2011. Testing two different precipitation datasets to compute the standardized precipitation index over the Horn of Africa. Int. J. Remote Sens. 32, 5947–5964.
Kuss, A., Brandt, W.T., Randall, J., Floyd, B., Bourai, A., Newcomer, M., Schmidt, C., Skiles, J., 2012. Comparison of changes in groundwater storage using GRACE data and a hydrological model in California's Central Valley. In: Proceedings of the

American Society for Photogrammetry and Remote Sensing (ASPRS); 2012 Annual Conference, pp. 12.
Kutser, T., Pierson, D.C., Tranvik, L., Reinart, A., Sobek, S., Kallio, K., 2005. Using satellite remote sensing to estimate the colored dissolved organic matter absorption coefficient in lakes. Ecosystems 8, 709–720.
Lambin, J., Morrow, R., Fu, L.-L., Willis, J.K., Bonekamp, H., Lillibridge, J., Perbos, J., Zaouche, G., Vaze, P., Bannoura, W., 2010. The OSTM/Jason-2 mission. Mar. Geod. 33, 4–25.
Landerer, F.W., Swenson, S., 2012. Accuracy of scaled GRACE terrestrial water storage estimates. Water Resour. Res. 48.
Landuyt, L., Van Wesemael, A., Schumann, G.J.-P., Hostache, R., Verhoest, N.E., Van Coillie, F.M., 2018. Flood Mapping Based on Synthetic Aperture Radar: An Assessment of Established Approaches. IEEE Trans. Geosci. Remote Sens. 1–18.
Lathrop, R., 1992. Landsat Thematic Mapper monitoring of turbid inland water quality. Photogramm. Eng. Remote Sens. 58, 465–470.
Lathrop, R., Lillesand, T.M., 1986. Use of Thematic Mapper data to assess water quality in Green Bay and central Lake Michigan. Photogramm. Eng. Remote Sens. 52, 671–680.
Le, C., Hu, C., Cannizzaro, J., English, D., Muller-Karger, F., Lee, Z., 2013. Evaluation of chlorophyll-a remote sensing algorithms for an optically complex estuary. Remote Sens. Environ. 129, 75–89.
Leon, J.G., Calmant, S., Seyler, F., Bonnet, M.-P., Cauhopé, M., Frappart, F., Filizola, N., Fraizy, P., 2006. Rating curves and estimation of average water depth at the upper Negro River based on satellite altimeter data and modeled discharges. J. Hydrol. 328, 481–496.
Lesht, B.M., Barbiero, R.P., Warren, G.J., 2013. A band-ratio algorithm for retrieving open-lake chlorophyll values from satellite observations of the Great Lakes. J. Great Lakes Res. 39, 138–152.
Lettenmaier, D.P., Famiglietti, J.S., 2006. Water from on high. Nature 444, 562–563.
Li, B., Rodell, M., 2015. Evaluation of a model-based groundwater drought indicator in the conterminous US. J. Hydrol. 526, 78–88.
Li, B., Rodell, M., Kumar, S., Beaudoing, H.K., Getirana, A., Zaitchik, B.F., de Goncalves, L.G., Cossetin, C., Bhanja, S., Mukherjee, A., 2019. Global GRACE data assimilation for groundwater and drought monitoring: Advances and challenges. Water Resour. Res.
Li, B., Rodell, M., Zaitchik, B.F., Reichle, R.H., Koster, R.D., van Dam, T.M., 2012. Assimilation of GRACE terrestrial water storage into a land surface model: Evaluation and potential value for drought monitoring in western and central Europe. J. Hydrol. 446, 103–115.
Li, F., Crow, W.T., Kustas, W.P., 2010. Towards the estimation root-zone soil moisture via the simultaneous assimilation of thermal and microwave soil moisture retrievals. Adv. Water Resour. 33 (2), 201–214.
Li, J., Yu, Q., Tian, Y.Q., Becker, B.L., Siqueira, P., Torbick, N., 2018. Spatio-temporal variations of CDOM in shallow inland waters from a semi-analytical inversion of Landsat-8. Remote Sens. Environ. 218, 189–200.
Li, Q., Zhong, B., Luo, Z., Yao, C., 2016. GRACE-based estimates of water discharge over the Yellow River basin. Geod. Geodyn. 7, 187–193.
Li, R., Li, J., 2004. Satellite remote sensing technology for lake water clarity monitoring: an overview. Environ. Inform. Arch. 2, 893–901.
Lillesand, T.M., Johnson, W.L., Deuell, R.L., Lindstrom, O.M., Meisner, D.E., 1983. Use of Landsat data to predict the trophic state of Minnesota lakes. Photogramm. Engng Remote Sens 49, 219–229.
Lim, J., Choi, M., 2015. Assessment of water quality based on Landsat 8 operational land imager associated with human activities in Korea. Environ. Monit. Assess. 187, 384.
Liu, D., Mishra, A.K., 2017. Performance of AMSR_E soil moisture data assimilation in CLM4. 5 model for monitoring hydrologic fluxes at global scale. J. Hydrol. 547, 67–79.
Liu, D., Mishra, A.K., Yu, Z., Yang, C., Konapala, G., Vu, T., 2017a. Performance of SMAP, AMSR-E and LAI for weekly agricultural drought forecasting over continental United States. J. Hydrol. 553, 88–104.
Liu, L., Liao, J., Chen, X., Zhou, G., Su, Y., Xiang, Z., Wang, Z., Liu, X., Li, Y., Wu, J., 2017b. The Microwave Temperature Vegetation Drought Index (MTVDI) based on AMSR-E brightness temperatures for long-term drought assessment across China (2003–2010). Remote Sens. Environ. 199, 302–320.
Liu, Z., Liu, P.-W., Massoud, E., Farr, T.G., Lundgren, P., Famiglietti, J.S., 2019. Monitoring Groundwater Change in California's Central Valley Using Sentinel-1 and GRACE Observations. Geosciences 9, 436.
Liversedge, L., 2007. Turbidity mapping and prediction in ice marginal lakes at the Bering Glacier system, Alaska.
Long, D., Scanlon, B.R., Longuevergne, L., Sun, A.Y., Fernando, D.N., Save, H., 2013. GRACE satellite monitoring of large depletion in water storage in response to the 2011 drought in Texas. Geophys. Res. Lett. 40, 3395–3401.
Long, S., Fatoyinbo, T.E., Policelli, F., 2014. Flood extent mapping for Namibia using change detection and thresholding with SAR. Environ. Res. Lett. 9, 035002.
Ma, S., Zhou, Y., Gowda, P.H., Dong, J., Zhang, G., Kakani, V.G., Wagle, P., Chen, L., Flynn, K.C., Jiang, W., 2019. Application of the water-related spectral reflectance indices: A review. Ecol. Ind. 98, 68–79.
MacIntosh, H., Profeti, G., 1995. The use of ERS SAR data to manage flood emergencies at the smaller scale. In: 2nd ERS Applications Workshop, European Space Agency, London, pp. 243–246.
Martens, B., Gonzalez Miralles, D., Lievens, H., Van Der Schalie, R., De Jeu, R.A., Fernández-Prieto, D., Verhoest, N., 2017. GLEAM v3: Satellite-based land evaporation and root-zone soil moisture. Geosci. Model Dev. 10 (5), 1903–1925.
Martínez-Fernández, J., González-Zamora, A., Sánchez, N., Gumuzzio, A., 2015. A soil water based index as a suitable agricultural drought indicator. J. Hydrol. 522, 265–273.
Martinis, S., Kersten, J., Twele, A., 2015. A fully automated TerraSAR-X based flood service. ISPRS J. Photogramm. Remote Sens. 104, 203–212.
Martinis, S., Twele, A., Voigt, S., 2009. Towards operational near real-time flood detection using a split-based automatic thresholding procedure on high resolution TerraSAR-X data. Nat. Hazards Earth Syst. Sci. 9, 303–314.
Mason, D.C., Schumann, G., Bates, P.D., 2011. Data utilization in flood inundation modelling.
Mason, I., Guzkowska, M., Rapley, C., Street-Perrott, F., 1994. The response of lake levels and areas to climatic change. Clim. Change 27, 161–197.
Matera, A., Fontana, G., Marletto, V., Zinoni, F., Botarelli, L., Tomei, F., 2007. Use of a new agricultural drought index within a regional drought observatory. In: Methods and tools for drought analysis and management. Springer, pp. 103–124.
Matgen, P., Hostache, R., Schumann, G., Pfister, L., Hoffmann, L., Savenije, H., 2011. Towards an automated SAR-based flood monitoring system: Lessons learned from two case studies. Phys. Chem. Earth, Parts A/B/C 36, 241–252.
McFeeters, S.K., 1996. The use of the Normalized Difference Water Index (NDWI) in the delineation of open water features. Int. J. Remote Sens. 17, 1425–1432.
McKee, T.B., Doesken, N.J., Kleist, J., 1993. The relationship of drought frequency and duration to time scales. In: Proceedings of the 8th Conference on Applied Climatology. American Meteorological Society, Boston, MA, pp. 179–183.
McLaughlin, D., 1995. Recent developments in hydrologic data assimilation. Rev. Geophys. 33, 977–984.
Meng, F., Su, F., Li, Y., Tong, K., 2019. Changes in terrestrial water storage during 2003–2014 and possible causes in Tibetan Plateau. J. Geophys. Res.: Atmos. 124, 2909–2931.
Menken, K.D., Brezonik, P.L., Bauer, M.E., 2006. Influence of chlorophyll and colored dissolved organic matter (CDOM) on lake reflectance spectra: Implications for measuring lake properties by remote sensing. Lake Reservoir Manage. 22, 179–190.
Michailovsky, C.I., Milzow, C., Bauer-Gottwein, P., 2013. Assimilation of radar altimetry to a routing model of the Brahmaputra River. Water Resour. Res. 49, 4807–4816.
Michailovsky, C.I.B., Bauer-Gottwein, P., 2014. Operational reservoir inflow forecasting with radar altimetry: the Zambezi case study. Hydrol. Earth Syst. Sci. 18, 997–1007.
Mishra, A.K., Coulibaly, P., 2009. Developments in hydrometric network design: a review. Rev. Geophys. 47 (2).
Mishra, A., Desai, V., 2005. Drought forecasting using stochastic models. Stoch. Env. Res. Risk Assess. 19, 326–339.
Mishra, A., Desai, V., 2006. Drought forecasting using feed-forward recursive neural network. Ecol. Model. 198, 127–138.
Mishra, A., Desai, V., Singh, V., 2007. Drought forecasting using a hybrid stochastic and neural network model. J. Hydrol. Eng. 12, 626–638.
Mishra, A.K., Ines, A.V., Das, N.N., Khedun, C.P., Singh, V.P., Sivakumar, B., Hansen, J.W., 2015. Anatomy of a local-scale drought: Application of assimilated remote sensing products, crop model, and statistical methods to an agricultural drought study. J. Hydrol. 526, 15–29.
Mishra, A.K., Singh, V.P., 2008. Development of drought SAF curves. Hydrology and hydraulics. Water Resources Publications, Highlands Ranch, 811–831.
Mishra, A.K., Singh, V.P., 2009. Analysis of drought severity-area-frequency curves using a general circulation model and scenario uncertainty. J. Geophys. Res.: Atmos. 114 (D6).
Mishra, A.K., Singh, V.P., 2011. Drought modeling–A review. J. Hydrol. 403 (1–2), 157–175.
Mishra, A., Vu, T., Veettil, A.V., Entekhabi, D., 2017. Drought monitoring with soil moisture active passive (SMAP) measurements. J. Hydrol. 552, 620–632.
Mishra, A.K., Singh, V.P., 2010. A review of drought concepts. J. Hydrol. 391, 202–216.
Mishra, S., Mishra, D.R., 2012. Normalized difference chlorophyll index: A novel model for remote estimation of chlorophyll-a concentration in turbid productive waters. Remote Sens. Environ. 117, 394–406.
Mishra, V., Aadhar, S., Asoka, A., Pai, S., Kumar, R., 2016. On the frequency of the 2015 monsoon season drought in the Indo-Gangetic Plain. Geophys. Res. Lett. 43 12,102-112,112.
Moreira, A., Prats-Iraola, P., Younis, M., Krieger, G., Hajnsek, I., Papathanassiou, K.P., 2013. A tutorial on synthetic aperture radar. IEEE Geosci. Remote Sens. Mag. 1, 6–43.
Morris, C.S., Gill, S.K., 1994. Variation of Great Lakes water levels derived from Geosat altimetry. Water Resour. Res. 30, 1009–1017.
Moser, G., Serpico, S.B., 2006. Generalized minimum-error thresholding for unsupervised change detection from SAR amplitude imagery. IEEE Trans. Geosci. Remote Sens. 44, 2972–2982.
Moses, W.J., Gitelson, A.A., Berdnikov, S., Povazhnyy, V., 2009. Satellite estimation of chlorophyll-$ a $ concentration using the red and NIR bands of MERIS—The Azov Sea case study. IEEE Geosci. Remote Sens. Lett. 6, 845–849.
Moya, L., Endo, Y., Okada, G., Koshimura, S., Mas, E., 2019. Drawback in the Change Detection Approach: False Detection during the 2018 Western Japan Floods. Remote Sensing 11, 2320.
Mu, Q., Zhao, M., Kimball, J.S., McDowell, N.G., Running, S.W., 2013. A remotely sensed global terrestrial drought severity index. Bull. Am. Meteorol. Soc. 94, 83–98.
Mukherjee, S., Mishra, A., Trenberth, K.E., 2018. Climate change and drought: a perspective on drought indices. Current Climate Change Reports 4, 145–163.
Munier, S., Polebistki, A., Brown, C., Belaud, G., Lettenmaier, D.P., 2015. SWOT data assimilation for operational reservoir management on the upper Niger River Basin. Water Resour. Res. 51, 554–575.
Murray-Tortarolo, G.N., Jaramillo, V.J., 2019. The impact of extreme weather events on livestock populations: the case of the 2011 drought in Mexico. Clim. Change 153, 79–89.
Narasimhan, B., Srinivasan, R., 2005. Development and evaluation of Soil Moisture Deficit Index (SMDI) and Evapotranspiration Deficit Index (ETDI) for agricultural drought monitoring. Agric. For. Meteorol. 133, 69–88.
Nasrabadi, T., Ruegner, H., Sirdari, Z.Z., Schwientek, M., Grathwohl, P., 2016. Using total

suspended solids (TSS) and turbidity as proxies for evaluation of metal transport in river water. Appl. Geochem. 68, 1–9.
Neal, J., Schumann, G., Bates, P., Buytaert, W., Matgen, P., Pappenberger, F., 2009. A data assimilation approach to discharge estimation from space. Hydrolog. Processes: Int. J. 23, 3641–3649.
Nelson, S.A., Soranno, P.A., Cheruvelil, K.S., Batzli, S.A., Skole, D.L., 2003. Regional assessment of lake water clarity using satellite remote sensing. J. Limnol. 27–32.
O'Connell, E., 2017. Towards adaptation of water resource systems to climatic and socio-economic change. Water Resour. Manage. 31 (10), 2965–2984.
Oberstadler, R., Hönsch, H., Huth, D., 1997. Assessment of the mapping capabilities of ERS-1 SAR data for flood mapping: a case study in Germany. Hydrol. Process. 11, 1415–1425.
Ojha, C., Shirzaei, M., Werth, S., Argus, D.F., Farr, T.G., 2018. Sustained groundwater loss in California's Central Valley exacerbated by intense drought periods. Water Resour. Res. 54, 4449–4460.
Okeowo, M.A., Lee, H., Hossain, F., Getirana, A., 2017. Automated generation of lakes and reservoirs water elevation changes from satellite radar altimetry. IEEE J. Sel. Top. Appl. Earth Obs. Remote Sens. 10, 3465–3481.
Oki, T., Kanae, S., 2006. Global hydrological cycles and world water resources. Science 313, 1068–1072.
Olmanson, L.G., Bauer, M.E., Brezonik, P.L., 2008. A 20-year Landsat water clarity census of Minnesota's 10,000 lakes. Remote Sens. Environ. 112, 4086–4097.
Ordoyne, C., Friedl, M.A., 2008. Using MODIS data to characterize seasonal inundation patterns in the Florida Everglades. Remote Sens. Environ. 112, 4107–4119.
O'Reilly, J.E., Maritorena, S., Mitchell, B.G., Siegel, D.A., Carder, K.L., Garver, S.A., Kahru, M., McClain, C., 1998. Ocean color chlorophyll algorithms for SeaWiFS. J. Geophys. Res. Oceans 103, 24937–24953.
Östlund, C., Flink, P., Strömbeck, N., Pierson, D., Lindell, T., 2001. Mapping of the water quality of Lake Erken, Sweden, from imaging spectrometry and Landsat Thematic Mapper. Sci. Total Environ. 268, 139–154.
Otsu, N., 1979. A threshold selection method from gray-level histograms. IEEE Trans. Syst., Man, Cybern. 9, 62–66.
Ouillon, S., Douillet, P., Petrenko, A., Neveux, J., Dupouy, C., Froidefond, J.-M., Andréfouët, S., Muñoz-Caravaca, A., 2008. Optical algorithms at satellite wavelengths for total suspended matter in tropical coastal waters. Sensors 8, 4165–4185.
Ouma, Y.O., Tateishi, R., 2006. A water index for rapid mapping of shoreline changes of five East African Rift Valley lakes: an empirical analysis using Landsat TM and ETM+ data. Int. J. Remote Sens. 27, 3153–3181.
Paiva, R., Collischonn, W., Bonnet, M.-P., De Goncalves, L., Calmant, S., Getirana, A., Santos da Silva, J., 2013. Assimilating in situ and radar altimetry data into a large-scale hydrologic-hydrodynamic model for streamflow forecast in the Amazon. Hydrol. Earth Syst. Sci. 17, 2929–2946.
Pal, N.R., Pal, S.K., 1993. A review on image segmentation techniques. Pattern Recogn. 26, 1277–1294.
Palmer, W., 1965. Meteorological Drought: Research Paper No. 45. US Department of Commerce Weather Bureau, Washington, DC, 58.
Palmer, W.C., 1968. Keeping track of crop moisture conditions, nationwide: The new crop moisture index.
Panu, U.S., Sharma, T.C., 2002. Challenges in drought research: some perspectives and future directions. Hydrol. Sci. J. 47 (S1), S19–S30.
Papa, F., Bala, S.K., Pandey, R.K., Durand, F., Gopalakrishna, V., Rahman, A., Rossow, W.B., 2012. Ganga-Brahmaputra river discharge from Jason-2 radar altimetry: An update to the long-term satellite-derived estimates of continental freshwater forcing flux into the Bay of Bengal. J. Geophys. Res. Oceans, 117.
Parinussa, R.M., Lakshmi, V., Johnson, F.M., Sharma, A., 2016. A new framework for monitoring flood inundation using readily available satellite data. Geophys. Res. Lett. 43, 2599–2605.
Park, S., Seo, E., Kang, D., Im, J., Lee, M.-I., 2018. Prediction of Drought on Pentad Scale Using Remote Sensing Data and MJO Index through Random Forest over East Asia. Remote Sensing 10, 1811.
Parrens, M., Al Bitar, A., Frappart, F., Paiva, R., Wongchuig, S., Papa, F., Yamasaki, D., Kerr, Y., 2019. High resolution mapping of inundation area in the Amazon basin from a combination of L-band passive microwave, optical and radar datasets. Int. J. Appl. Earth Obs. Geoinf. 81, 58–71.
Parry, M., Parry, M.L., Canziani, O., Palutikof, J., Van der Linden, P., Hanson, C., 2007. Climate change 2007-impacts, adaptation and vulnerability: Working group II contribution to the fourth assessment report of the IPCC. Cambridge University Press.
Pavelsky, T.M., Durand, M.T., Andreadis, K.M., Beighley, R.E., Paiva, R.C., Allen, G.H., Miller, Z.F., 2014. Assessing the potential global extent of SWOT river discharge observations. J. Hydrol. 519, 1516–1525.
Pearson, C.P., 1998. Changes to New Zealand's national hydrometric network in the 1990s. J. Hydrol. NZ 37, 1–17.
Pedinotti, V., Boone, A., Ricci, S., Biancamaria, S., Mognard, N., 2014. Assimilation of satellite data to optimize large-scale hydrological model parameters: a case study for the SWOT mission. Hydrol. Earth Syst. Sci. 18, 4485–4507.
Pedro-Monzonís, M., Solera, A., Ferrer, J., Estrela, T., Paredes-Arquiola, J., 2015. A review of water scarcity and drought indexes in water resources planning and management. J. Hydrol. 527, 482–493.
Peterson, K., Sagan, V., Sidike, P., Cox, A., Martinez, M., 2018. Suspended Sediment Concentration Estimation from Landsat Imagery along the Lower Missouri and Middle Mississippi Rivers Using an Extreme Learning Machine. Remote Sensing 10, 1503.
Pikaz, A., Averbuch, A., 1996. Digital image thresholding, based on topological stable-state. Pattern Recogn. 29, 829–843.
Podlaha, A., Bowen, S., Lörinc, M., Bhattacharya, A., 2019. Global catastrophe recap-March 2017. Aon Benfield Analytics.
Potes, M., Costa, M.J., Salgado, R., 2012. Satellite remote sensing of water turbidity in Alqueva reservoir and implications on lake modelling. Hydrol. Earth Syst. Sci. 16, 1623–1633.
Pozzi, W., Sheffield, J., Stefanski, R., Cripe, D., Pulwarty, R., Vogt, J.V., Heim Jr, R.R., Brewer, M.J., Svoboda, M., Westerhoff, R., 2013. Toward global drought early warning capability: Expanding international cooperation for the development of a framework for monitoring and forecasting. Bull. Am. Meteorol. Soc. 94, 776–785.
Preisendorfer, R.W., 1986. Secchi disk science: Visual optics of natural waters 1. Limnol. Oceanogr. 31, 909–926.
Prigent, C., Matthews, E., Aires, F., Rossow, W.B., 2001. Remote sensing of global wetland dynamics with multiple satellite data sets. Geophys. Res. Lett. 28, 4631–4634.
Prigent, C., Matthews, E., Lettenmaier, D., Aires, F., Papa, F., 2016. Toward a high resolution monitoring of continental surface water extent and dynamics, at global scale: From GIEMS (Global Inundation Extent from Multi-Satellites) to SWOT (Surface Water Ocean Topography). Surv. Geophys 37, 339–355.
Pulvirenti, L., Pierdicca, N., Chini, M., Guerriero, L., 2011. An algorithm for operational flood mapping from synthetic aperture radar (SAR) data based on the fuzzy logic. Natural Hazard Earth Syst. Sci.
Qi, L., Hu, C., Duan, H., Barnes, B., Ma, R., 2014. An EOF-based algorithm to estimate chlorophyll a concentrations in Taihu Lake from MODIS land-band measurements: Implications for near real-time applications and forecasting models. Remote Sensing 6, 10694–10715.
Quiring, S.M., Ganesh, S., 2010. Evaluating the utility of the Vegetation Condition Index (VCI) for monitoring meteorological drought in Texas. Agric. For. Meteorol. 150, 330–339.
Rajaram, T., Das, A., 2008. Water pollution by industrial effluents in India: Discharge scenarios and case for participatory ecosystem specific local regulation. Futures 40, 56–69.
Rajinikanth, V., Fernandes, S.L., Bhushan, B., Sunder, N.R., 2018. Segmentation and analysis of brain tumor using Tsallis entropy and regularised level set. In: Proceedings of 2nd International Conference on Micro-Electronics, Electromagnetics and Telecommunications. Springer, pp. 313–321.
Rajsekhar, D., Singh, V.P., Mishra, A.K., 2015. Multivariate drought index: An information theory based approach for integrated drought assessment. J. Hydrol. 526, 164–182.
Ramesh, N., Yoo, J.-H., Sethi, I., 1995. Thresholding based on histogram approximation. IEE Proc.-Vision, Image Signal Process. 142, 271–279.
Rateb, A., Kuo, C.-Y., 2019. Quantifying Vertical Deformation in the Tigris-Euphrates Basin Due to the Groundwater Abstraction: Insights from GRACE and Sentinel-1 Satellites. Water 11, 1658.
Reager, J., Famiglietti, J., 2009. Global terrestrial water storage capacity and flood potential using GRACE. Geophys. Res. Lett. 36.
Reichle, R.H., Liu, Q., Koster, R.D., Crow, W.T., De Lannoy, G.J., Kimball, J.S., Kolassa, J., 2019. Version 4 of the SMAP Level-4 Soil Moisture Algorithm and Data. Product. 10, 3106–3130.
Reichle, R.H., De Lannoy, G.J., Liu, Q., Ardizzone, J.V., Colliander, A., Conaty, A., Koster, R.D., 2017. Assessment of the SMAP level-4 surface and root-zone soil moisture product using in situ measurements. J. Hydrometeorol. 18 (10), 2621–2645.
Rhee, J., Im, J., 2017. Meteorological drought forecasting for ungauged areas based on machine learning: Using long-range climate forecast and remote sensing data. Agric. For. Meteorol. 237, 105–122.
Rhee, J., Im, J., Carbone, G.J., 2010. Monitoring agricultural drought for arid and humid regions using multi-sensor remote sensing data. Remote Sens. Environ. 114, 2875–2887.
Richey, A.S., Thomas, B.F., Lo, M.H., Reager, J.T., Famiglietti, J.S., Voss, K., Swenson, S., Rodell, M., 2015. Quantifying renewable groundwater stress with GRACE. Water Resour. Res. 51, 5217–5238.
Ridler, T., Calvard, S., 1978. Picture thresholding using an iterative selection method. IEEE Trans. Syst., Man Cybern. 8, 630–632.
Ritchie, J., Schiebe, F., McHenry, J., 1976. Remote sensing of suspended sediments in surface waters. Photogramm. Eng. Remote Sens. 42, 1539–1545.
Ritchie, J.C., Cooper, C.M., 1988. Comparison of measured suspended sediment concentrations with suspended sediment concentrations estimated from Landsat MSS data. Remote Sensing 9, 379–387.
Ritchie, J.C., Cooper, C.M., Schiebe, F.R., 1990. The relationship of MSS and TM digital data with suspended sediments, chlorophyll, and temperature in Moon Lake, Mississippi. Remote Sens. Environ. 33, 137–148.
Ritchie, J.C., Zimba, P.V., Everitt, J.H., 2003. Remote sensing techniques to assess water quality. Photogramm. Eng. Remote Sens. 69, 695–704.
Rodda, J.C., Pieyns, S.A., Sehmi, N.S., Matthews, G., 1993. Towards a world hydrological cycle observing system. Hydrol. Sci. J. 38 (5), 373–378.
Rodell, M., Famiglietti, J., 2002. The potential for satellite-based monitoring of groundwater storage changes using GRACE: the High Plains aquifer, Central US. J. Hydrol. 263, 245–256.
Rodell, M., Chen, J., Kato, H., Famiglietti, J.S., Nigro, J., Wilson, C.R., 2007. Estimating groundwater storage changes in the Mississippi River basin (USA) using GRACE. Hydrogeol. J. 15, 159–166.
Rodell, M., Velicogna, I., Famiglietti, J.S., 2009. Satellite-based estimates of groundwater depletion in India. Nature 460, 999.
Rodríguez-Fernández, N.J., Anterrieu, E., Rougé, B., Boutin, J., Picard, G., Pellarin, T., Escorihuela, M.J., Al Bitar, A., Richaume, P., Mialon, A., 2019. SMOS-HR: A high resolution L-band passive radiometer for Earth science and applications. In: IGARSS 2019-2019 IEEE International Geoscience and Remote Sensing Symposium. IEEE, pp. 8392–8395.
Rosenfeld, A., De La Torre, P., 1983. Histogram concavity analysis as an aid in threshold selection. IEEE Trans. Syst., Man, Cybern. 231–235.

Rosenzweig, C., Tubiello, F.N., Goldberg, R., Mills, E., Bloomfield, J., 2002. Increased crop damage in the US from excess precipitation under climate change. Global Environ. Change 12, 197–202.
Rouault, M., Richard, Y., 2003. Intensity and spatial extension of drought in South Africa at different time scales. *water*. SA 29, 489–500.
Roy, P., Sharma, S., Gairola, R.M., 2015. Detection of Rain/Cloud Pixels by Ka-band AltiKa Altimeter over the Tropical Region: Development of a Rain/Cloud Flag Algorithm and its Validation. Mar. Geod. 38, 86–106.
Rügner, H., Schwientek, M., Beckingham, B., Kuch, B., Grathwohl, P., 2013. Turbidity as a proxy for total suspended solids (TSS) and particle facilitated pollutant transport in catchments. Environ. Earth Sci. 69, 373–380.
Rundquist, D.C., Han, L., Schalles, J.F., Peake, J.S., 1996. Remote measurement of algal chlorophyll in surface waters: the case for the first derivative of reflectance near 690 nm. Photogramm. Eng. Remote Sens. 62, 195–200.
Sahoo, P., Wilkins, C., Yeager, J., 1997. Threshold selection using Renyi's entropy. Pattern Recogn. 30, 71–84.
Sahoo, P.K., Soltani, S., Wong, A.K., 1988. A survey of thresholding techniques. Computer Vision, Graphics, Image Process. 41, 233–260.
Sánchez, N., González-Zamora, Á., Martínez-Fernández, J., Piles, M., Pablos, M., 2018. Integrated remote sensing approach to global agricultural drought monitoring. Agric. For. Meteorol. 259, 141–153.
Sánchez, N., González-Zamora, Á., Piles, M., Martínez-Fernández, J., 2016. A new Soil Moisture Agricultural Drought Index (SMADI) integrating MODIS and SMOS products: a case of study over the Iberian Peninsula. Remote Sensing 8, 287.
Sanyal, J., Lu, X., 2004. Application of remote sensing in flood management with special reference to monsoon Asia: a review. Nat. Hazards 33, 283–301.
Sarkar, S., Das, S., Chaudhuri, S.S., 2016. Hyper-spectral image segmentation using Rényi entropy based multi-level thresholding aided with differential evolution. Expert Syst. Appl. 50, 120–129.
Sawaya, K.E., Olmanson, L.G., Heinert, N.J., Brezonik, P.L., Bauer, M.E., 2003. Extending satellite remote sensing to local scales: land and water resource monitoring using high-resolution imagery. Remote Sens. Environ. 88, 144–156.
Schiebe, F., Harrington Jr, J., Ritchie, J., 1992. Remote sensing of suspended sediments: the Lake Chicot, Arkansas project. Int. J. Remote Sens. 13, 1487–1509.
Schmidt, R., Schwintzer, P., Flechtner, F., Reigber, C., Güntner, A., Döll, P., Ramillien, G., Cazenave, A., Petrovic, S., Jochmann, H., 2006. GRACE observations of changes in continental water storage. Global Planet. Change 50, 112–126.
Schmugge, T., 1987. Remote sensing applications in hydrology. Rev. Geophys. 25, 148–152.
Schneider, R., Tarpanelli, A., Nielsen, K., Madsen, H., Bauer-Gottwein, P., 2018. Evaluation of multi-mode CryoSat-2 altimetry data over the Po River against in situ data and a hydrodynamic model. Adv. Water Resour. 112, 17–26.
Schroeder, R., McDonald, K., Chapman, B., Jensen, K., Podest, E., Tessler, Z., Bohn, T., Zimmermann, R., 2015. Development and evaluation of a multi-year fractional surface water data set derived from active/passive microwave remote sensing data. Remote Sensing 7, 16688–16732.
Schumacher, M., Forootan, E., van Dijk, A., Schmied, H.M., Crosbie, R., Kusche, J., Döll, P., 2018. Improving drought simulations within the Murray-Darling Basin by combined calibration/assimilation of GRACE data into the WaterGAP Global Hydrology Model. Remote Sens. Environ. 204, 212–228.
Schumann, G., Bates, P.D., Horritt, M.S., Matgen, P., Pappenberger, F., 2009. Progress in integration of remote sensing–derived flood extent and stage data and hydraulic models. Rev. Geophys. 47.
Schumann, G., Di Baldassarre, G., Alsdorf, D., Bates, P., 2010. Near real-time flood wave approximation on large rivers from space: Application to the River Po, Italy. Water Resour. Res. 46.
Schumann, G.J.P., Bates, P.D., Di Baldassarre, G., Mason, D.C., 2012. The use of radar imagery in riverine flood inundation studies. Fluvial Remote Sensing Sci. Manage. 115–140.
Seyhan, E., Dekker, A., 1986. Application of remote sensing techniques for water quality monitoring. Hydrobiol. Bull. 20, 41–50.
Sezan, M.I., 1990. A peak detection algorithm and its application to histogram-based image data reduction. Computer Vision, Graphics, Image Process. 49, 36–51.
Sezgin, M., Sankur, B., 2004. Survey over image thresholding techniques and quantitative performance evaluation. J. Electron. Imaging 13, 146–166.
Shah, A., Mathur, N., 2019. Contestations around water allocation during a climate crisis in India: The case of ‘IPL vs. drought’. Global Environ. Change 57, 101927.
Sheard, B., Heinzel, G., Danzmann, K., Shaddock, D., Klipstein, W., Folkner, W., 2012. Intersatellite laser ranging instrument for the GRACE follow-on mission. J. Geod. 86, 1083–1095.
Sheffield, J., Wood, E.F., 2007. Characteristics of global and regional drought, 1950–2000: Analysis of soil moisture data from off-line simulation of the terrestrial hydrologic cycle. J. Geophys. Res.: Atmos. 12.
Sheffield, J., Wood, E.F., Roderick, M.L., 2012. Little change in global drought over the past 60 years. Nature 491, 435.
Sheffield, J., Wood, E.F., Chaney, N., Guan, K., Sadri, S., Yuan, X., Olang, L., Amani, A., Ali, A., Demuth, S., 2014. A drought monitoring and forecasting system for sub-Sahara African water resources and food security. Bull. Am. Meteorol. Soc. 95, 861–882.
Sheffield, J., Wood, E.F., Pan, M., Beck, H., Coccia, G., Serrat-Capdevila, A., Verbist, K., 2018. Satellite Remote Sensing for Water Resources Management: Potential for Supporting Sustainable Development in Data-Poor Regions. Water Resour. Res. 54, 9724–9758.
Shiklomanov, A.I., Lammers, R.B., Vörösmarty, C.J., 2002. Widespread decline in hydrological monitoring threatens pan-Arctic research. Eos, Trans. Am. Geophys. Union 83, 13–17.
Shrestha, N.K., Qamer, F.M., Pedreros, D., Murthy, M., Wahid, S.M., Shrestha, M., 2017. Evaluating the accuracy of Climate Hazard Group (CHG) satellite rainfall estimates for precipitation based drought monitoring in Koshi basin, Nepal. J. Hydrol.: Regional Stud. 13, 138–151.
Shukla, S., Wood, A.W., 2008. Use of a standardized runoff index for characterizing hydrologic drought. Geophys. Res. Lett. 35.
Sichangi, A.W., Wang, L., Yang, K., Chen, D., Wang, Z., Li, X., Zhou, J., Liu, W., Kuria, D., 2016. Estimating continental river basin discharges using multiple remote sensing data sets. Remote Sens. Environ. 179, 36–53.
Siegel, D., Maritorena, S., Nelson, N., Hansell, D.A., Lorenzi-Kayser, M., 2002. Global distribution and dynamics of colored dissolved and detrital organic materials. J. Geophys. Res.: Oceans 107 21-21-21-14.
Sinha, D., Syed, T.H., Famiglietti, J.S., Reager, J.T., Thomas, R.C., 2017. Characterizing drought in India using GRACE observations of terrestrial water storage deficit. J. Hydrometeorol. 18, 381–396.
Sirajul Islam, M., Brooks, A., Kabir, M., Jahid, I., Shafiqul Islam, M., Goswami, D., Nair, G., Larson, C., Yukiko, W., Luby, S., 2007. Faecal contamination of drinking water sources of Dhaka city during the 2004 flood in Bangladesh and use of disinfectants for water treatment. J. Appl. Microbiol. 103, 80–87.
Smith, L.C., 1997. Satellite remote sensing of river inundation area, stage, and discharge: A review. Hydrol. Process. 11, 1427–1439.
Smith, L.C., Pavelsky, T.M., 2008. Estimation of river discharge, propagation speed, and hydraulic geometry from space: Lena River, Siberia. Water Resour. Res. 44.
Smith, L.C., Isacks, B.L., Bloom, A.L., Murray, A.B., 1996. Estimation of discharge from three braided rivers using synthetic aperture radar satellite imagery: Potential application to ungaged basins. Water Resour. Res. 32, 2021–2034.
Smith, L.C., Isacks, B.L., Forster, R.R., Bloom, A.L., Preuss, I., 1995. Estimation of discharge from braided glacial rivers using ERS 1 synthetic aperture radar: First results. Water Resour. Res. 31, 1325–1329.
Somvanshi, S., Kunwar, P., Singh, N., Shukla, S., Pathak, V., 2012. Integrated remote sensing and GIS approach for water quality analysis of Gomti river, Uttar Pradesh. Int. J. Environ. Sci. 3, 62.
Sòria-Perpinyà, X., Vicente, E., Urrego, P., Pereira-Sandoval, M., Ruíz-Verdú, A., Delegido, J., Soria, J.M., Moreno, J., 2020. Remote sensing of cyanobacterial blooms in a hypertrophic lagoon (Albufera of València, Eastern Iberian Peninsula) using multitemporal Sentinel-2 images. Sci. Total Environ. 698, 134305.
Sridhar, V., Hubbard, K.G., You, J., Hunt, E.D., 2008. Development of the soil moisture index to quantify agricultural drought and its “user friendliness” in severity-area-duration assessment. J. Hydrometeorol. 9, 660–676.
Stadelmann, T.H., Brezonik, P.L., Kloiber, S., 2001. Seasonal patterns of chlorophyll a and Secchi disk transparency in lakes of East-Central Minnesota: Implications for design of ground-and satellite-based monitoring programs. Lake Reservoir Manage. 17, 299–314.
Stedmon, C., Amon, R., Rinehart, A., Walker, S., 2011. The supply and characteristics of colored dissolved organic matter (CDOM) in the Arctic Ocean: Pan Arctic trends and differences. Mar. Chem. 124, 108–118.
Sulistioadi, Y., Tseng, K.-H., Shum, C., Hidayat, H., Sumaryono, M., Suhardiman, A., Setiawan, F., Sunarso, S., 2015. Satellite radar altimetry for monitoring small rivers and lakes in Indonesia. Hydrol. Earth Syst. Sci. 19, 341–359.
Svoboda, M., Hayes, M., Wood, D., 2012. Standardized precipitation index user guide. World Meteorological Organization Geneva, Switzerland.
Swain, R., Sahoo, B., 2017. Mapping of heavy metal pollution in river water at daily time-scale using spatio-temporal fusion of MODIS-aqua and Landsat satellite imageries. J. Environ. Manage. 192, 1–14.
Syed, T.H., Famiglietti, J.S., Chambers, D.P., 2009. GRACE-based estimates of terrestrial freshwater discharge from basin to continental scales. J. Hydrometeorol. 10, 22–40.
Syed, T.H., Famiglietti, J.S., Chambers, D.P., Willis, J.K., Hilburn, K., 2010. Satellite-based global-ocean mass balance estimates of interannual variability and emerging trends in continental freshwater discharge. Proc. Natl. Acad. Sci. 107, 17916–17921.
Syed, T.H., Famiglietti, J.S., Rodell, M., Chen, J., Wilson, C.R., 2008. Analysis of terrestrial water storage changes from GRACE and GLDAS. Water Resour. Res. 44.
Tadesse, T., Demisse, G.B., Zaitchik, B., Dinku, T., 2014. Satellite-based hybrid drought monitoring tool for prediction of vegetation condition in Eastern Africa: A case study for Ethiopia. Water Resour. Res. 50, 2176–2190.
Tang, Q., Gao, H., Lu, H., Lettenmaier, D.P., 2009. Remote sensing: hydrology. Prog. Phys. Geogr. 33, 490–509.
Tapley, B.D., Bettadpur, S., Ries, J.C., Thompson, P.F., Watkins, M.M., 2004a. GRACE measurements of mass variability in the Earth system. Science 305, 503–505.
Tapley, B.D., Bettadpur, S., Watkins, M., Reigber, C., 2004b. The gravity recovery and climate experiment: Mission overview and early results. Geophys. Res. Lett. 31.
Tarpanelli, A., Brocca, L., Barbetta, S., Faruolo, M., Lacava, T., Moramarco, T., 2014. Coupling MODIS and radar altimetry data for discharge estimation in poorly gauged river basins. IEEE J. Sel. Top. Appl. Earth Obs. Remote Sens. 8, 141–148.
Tarpanelli, A., Camici, S., Nielsen, K., Brocca, L., Moramarco, T., Benveniste, J., 2019. Potentials and limitations of Sentinel-3 for river discharge assessment. Adv. Space Res.
Tase, N., 1976. Area-deficit-intensity characteristics of droughts. *Hydrology Paper No. 87, Colorado*. State University, Fort Collins CO.
Taufik, M., Torfs, P.J., Uijlenhoet, R., Jones, P.D., Murdiyarso, D., Van Lanen, H.A., 2017. Amplification of wildfire area burnt by hydrological drought in the humid tropics. Nat. Clim. Change 7, 428.
Tehrani, N., D'Sa, E., Osburn, C., Bianchi, T., Schaeffer, B., 2013. Chromophoric dissolved organic matter and dissolved organic carbon from sea-viewing wide field-of-view sensor (SeaWiFS), Moderate Resolution Imaging Spectroradiometer (MODIS) and MERIS Sensors: case study for the Northern Gulf of Mexico. Remote Sensing 5, 1439–1464.

Thiemann, S., Kaufmann, H., 2002. Lake water quality monitoring using hyperspectral airborne data—a semiempirical multisensor and multitemporal approach for the Mecklenburg Lake District, Germany. Remote Sens. Environ. 81, 228–237.
Thomas, A.C., Reager, J.T., Famiglietti, J.S., Rodell, M., 2014. A GRACE-based water storage deficit approach for hydrological drought characterization. Geophys. Res. Lett. 41, 1537–1545.
Thomas, B.F., Famiglietti, J.S., Landerer, F.W., Wiese, D.N., Molotch, N.P., Argus, D.F., 2017. GRACE groundwater drought index: Evaluation of California Central Valley groundwater drought. Remote Sens. Environ. 198, 384–392.
Thornthwaite, C.W., Mather, J.R., 1955. The water balance. Climatology 9, 1–104.
Tian, S., Tregoning, P., Renzullo, L.J., van Dijk, A.I., Walker, J.P., Pauwels, V.R., Allgeyer, S., 2017. Improved water balance component estimates through joint assimilation of GRACE water storage and SMOS soil moisture retrievals. Water Resour. Res. 53, 1820–1840.
Tiwari, V., Wahr, J., Swenson, S., 2009. Dwindling groundwater resources in northern India, from satellite gravity observations. Geophys. Res Lett. 36.
Torres, R., Snoeij, P., Geudtner, D., Bibby, D., Davidson, M., Attema, E., Potin, P., Rommen, B., Floury, N., Brown, M., 2012. GMES Sentinel-1 mission. Remote Sens. Environ. 120, 9–24.
Tourian, M., Sneeuw, N., Bárdossy, A., 2013. A quantile function approach to discharge estimation from satellite altimetry (ENVISAT). Water Resour. Res. 49, 4174–4186.
Tsakiris, G., Pangalou, D., Vangelis, H., 2007. Regional drought assessment based on the Reconnaissance Drought Index (RDI). Water Resour. Manage. 21, 821–833.
Tucker, C.J., 1979. Red and photographic infrared linear combinations for monitoring vegetation. Remote Sens. Environ. 8, 127–150.
Twardowski, M.S., Donaghay, P.L., 2001. Separating in situ and terrigenous sources of absorption by dissolved materials in coastal waters. J. Geophys. Res. Oceans 106, 2545–2560.
Twele, A., Cao, W., Plank, S., Martinis, S., 2016. Sentinel-1-based flood mapping: a fully automated processing chain. Int. J. Remote Sens. 37, 2990–3004.
Tyler, J.E., 1968. The Secchi disc. Limnol. Oceanogr. 13, 1–6.
Ulaby, F.T., Moore, R.K., Fung, A.K., 1982. Microwave remote sensing: Active and passive. Volume 2-Radar remote sensing and surface scattering and emission theory.
USGS, 2014. Estimation of Secchi Depth from turbidity Data in the Willamette River at Portland. http://or.water.usgs.gov/will_morrison/secchi_depth_model.
Van Dijk, A., Renzullo, L.J., 2011. Water resource monitoring systems and the role of satellite observations.
Van Dijk, A., Renzullo, L.J., Rodell, M., 2011. Use of Gravity Recovery and Climate Experiment terrestrial water storage retrievals to evaluate model estimates by the Australian water resources assessment system. Water Resour. Res. 47.
Van Loon, A.F., Gleeson, T., Clark, J., Van Dijk, A.I., Stahl, K., Hannaford, J., Di Baldassarre, G., Teuling, A.J., Tallaksen, L.M., Uijlenhoet, R., 2016. Drought in the Anthropocene. Nat. Geosci. 9, 89.
Van Loon, A.F., Kumar, R., Mishra, V., 2017. Testing the use of standardised indices and GRACE satellite data to estimate the European 2015 groundwater drought in near-real time. Hydrol. Earth Syst. Sci. 21, 1947.
Vicente-Serrano, S.M., Beguería, S., López-Moreno, J.I., 2010. A multiscalar drought index sensitive to global warming: the standardized precipitation evapotranspiration index. J. Clim. 23, 1696–1718.
Vicente-Serrano, S.M., Miralles, D.G., Domínguez-Castro, F., Azorin-Molina, C., El Kenawy, A., McVicar, T.R., Tomás-Burguera, M., Beguería, S., Maneta, M., Peña-Gallardo, M., 2018. Global assessment of the Standardized Evapotranspiration Deficit Index (SEDI) for drought analysis and monitoring. J. Clim. 31, 5371–5393.
Villadsen, H., Andersen, O.B., Stenseng, L., Nielsen, K., Knudsen, P., 2015. CryoSat-2 altimetry for river level monitoring—Evaluation in the Ganges-Brahmaputra River basin. Remote Sens. Environ. 168, 80–89.
Vitousek, P.M., Aber, J.D., Howarth, R.W., Likens, G.E., Matson, P.A., Schindler, D.W., Schlesinger, W.H., Tilman, D.G., 1997. Human alteration of the global nitrogen cycle: sources and consequences. Ecol. Appl. 7, 737–750.
Volpe, V., Silvestri, S., Marani, M., 2011. Remote sensing retrieval of suspended sediment concentration in shallow waters. Remote Sens. Environ. 115, 44–54.
Vörösmarty, C.J., McIntyre, P.B., Gessner, M.O., Dudgeon, D., Prusevich, A., Green, P., Glidden, S., Bunn, S.E., Sullivan, C.A., Liermann, C.R., 2010. Global threats to human water security and river biodiversity. Nature 467, 555.
Vos, R., Hakvoort, J., Jordans, R., Ibelings, B.W., 2003. Multiplatform optical monitoring of eutrophication in temporally and spatially variable lakes. Sci. Total Environ. 312, 221–243.
Voss, K.A., Famiglietti, J.S., Lo, M., De Linage, C., Rodell, M., Swenson, S.C., 2013. Groundwater depletion in the Middle East from GRACE with implications for transboundary water management in the Tigris-Euphrates-Western Iran region. Water Resour. Res. 49, 904–914.
Vyas, S.S., Bhattacharya, B.K., Nigam, R., Guhathakurta, P., Ghosh, K., Chattopadhyay, N., Gairola, R.M., 2015. A combined deficit index for regional agricultural drought assessment over semi-arid tract of India using geostationary meteorological satellite data. Int. J. Appl. Earth Obs. Geoinf. 39, 28–39.
Wahr, J., Swenson, S., Zlotnicki, V., Velicogna, I., 2004. Time-variable gravity from GRACE: First results. Geophys. Res. Lett. 31.
Wan, L., Liu, M., Wang, F., Zhang, T., You, H., 2019. Automatic extraction of flood inundation areas from SAR images: a case study of Jilin, China during the 2017 flood disaster. Int. J. Remote Sens. 40, 5050–5077.
Wang, H., Yang, Z., Saito, Y., Liu, J.P., Sun, X., 2006. Interannual and seasonal variation of the Huanghe (Yellow River) water discharge over the past 50 years: connections to impacts from ENSO events and dams. Global Planet. Change 50, 212–225.
Wang, L., Qu, J.J., 2007. NMDI: A normalized multi-band drought index for monitoring soil and vegetation moisture with satellite remote sensing. Geophys. Res. Lett. 34.
Wang, X., de Linage, C., Famiglietti, J., Zender, C.S., 2011. Gravity Recovery and Climate Experiment (GRACE) detection of water storage changes in the Three Gorges Reservoir of China and comparison with in situ measurements. Water Resour. Res. 47.
Wass, P., Marks, S., Finch, J., Leeks, G.J.L., Ingram, J., 1997. Monitoring and preliminary interpretation of in-river turbidity and remote sensed imagery for suspended sediment transport studies in the Humber catchment. Sci. Total Environ. 194, 263–283.
Wells, N., Goddard, S., Hayes, M.J., 2004. A self-calibrating Palmer drought severity index. J. Clim. 17, 2335–2351.
West, H., Quinn, N., Horswell, M., 2019. Remote sensing for drought monitoring & impact assessment: Progress, past challenges and future opportunities. Remote Sens. Environ. 232, 111291.
Wing, O.E., Bates, P.D., Smith, A.M., Sampson, C.C., Johnson, K.A., Fargione, J., Morefield, P., 2018. Estimates of present and future flood risk in the conterminous United States. Environ. Res. Lett. 13, 034023.
Woodhouse, I.H., 2017. Introduction to Microwave Remote Sensing. CRC Press.
Woodruff, D.L., Stumpf, R.P., Scope, J.A., Paerl, H.W., 1999. Remote estimation of water clarity in optically complex estuarine waters. Remote Sens. Environ. 68, 41–52.
World Population Prospects. (2019). https://www.un.org/development/desa/en/news/population/world-population-prospects-2019.html.
Wu, G., De Leeuw, J., Skidmore, A.K., Prins, H.H., Liu, Y., 2008. Comparison of MODIS and Landsat TM5 images for mapping tempo–spatial dynamics of Secchi disk depths in Poyang Lake National Nature Reserve, China. Int. J. Remote Sens. 29, 2183–2198.
Xu, H., 2006. Modification of normalised difference water index (NDWI) to enhance open water features in remotely sensed imagery. Int. J. Remote Sens. 27, 3025–3033.
Xu, K., Zhang, J., Watanabe, M., Sun, C., 2004. Estimating river discharge from very high-resolution satellite data: a case study in the Yangtze River, China. Hydrol. Process. 18, 1927–1939.
Yan, H., Moradkhani, H., Zarekarizi, M., 2017. A probabilistic drought forecasting framework: A combined dynamical and statistical approach. J. Hydrol. 548, 291–304.
Yan, H., Wang, S.Q., Lu, H.Q., Yu, Q., Zhu, Z.C., Myneni, R.B., Liu, Q., Shugart, H.H., 2014. Development of a remotely sensing seasonal vegetation-based Palmer Drought Severity Index and its application of global drought monitoring over 1982–2011. J. Geophys. Res: Atmos. 119, 9419–9440.
Yirdaw, S.Z., Snelgrove, K.R., Agboma, C.O., 2008. GRACE satellite observations of terrestrial moisture changes for drought characterization in the Canadian Prairie. J. Hydrol. 356, 84–92.
Yoon, Y., Durand, M., Merry, C.J., Clark, E.A., Andreadis, K.M., Alsdorf, D.E., 2012. Estimating river bathymetry from data assimilation of synthetic SWOT measurements. J. Hydrol. 464, 363–375.
Zaitchik, B.F., Rodell, M., Reichle, R.H., 2008. Assimilation of GRACE terrestrial water storage data into a land surface model: Results for the Mississippi River basin. J. Hydrometeorol. 9, 535–548.
Zambrano, F., Lillo-Saavedra, M., Verbist, K., Lagos, O., 2016. Sixteen years of agricultural drought assessment of the BioBío region in Chile using a 250 m resolution Vegetation Condition Index (VCI). Remote Sensing 8, 530.
Zargar, A., Sadiq, R., Naser, B., Khan, F.I., 2011. A review of drought indices. Environ. Rev. 19, 333–349.
Zhang, A., Jia, G., 2013. Monitoring meteorological drought in semiarid regions using multi-sensor microwave remote sensing data. Remote Sens. Environ. 134, 12–23.
Zhang, A., Jia, G., Wang, H., 2019a. Improving meteorological drought monitoring capability over tropical and subtropical water-limited ecosystems: evaluation and ensemble of the Microwave Integrated Drought Index. Environ. Res. Lett. 14, 044025.
Zhang, B., AghaKouchak, A., Yang, Y., Wei, J., Wang, G., 2019b. A water-energy balance approach for multi-category drought assessment across globally diverse hydrological basins. Agric. For. Meteorol. 264, 247–265.
Zhang, D., Liu, X., Bai, P., 2019c. Assessment of hydrological drought and its recovery time for eight tributaries of the Yangtze River (China) based on downscaled GRACE data. J. Hydrol. 568, 592–603.
Zhang, D., Zhang, Q., Werner, A.D., Liu, X., 2016. GRACE-based hydrological drought evaluation of the Yangtze River Basin, China. J. Hydrometeorol. 17, 811–828.
Zhang, J., Xu, K., Watanabe, M., Yang, Y., Chen, X., 2004. Estimation of river discharge from non-trapezoidal open channel using QuickBird-2 satellite imagery/Utilisation des images satellites de Quickbird-2 pour le calcul des débits fluviaux en chenaux ouverts non-trapézoidaux. Hydrolog. Sci. J. 49.
Zhang, L., Liu, Y., Ren, L., Jiang, S., Yang, X., Yuan, F., Wang, M., Wei, L., 2019d. Drought Monitoring and Evaluation by ESA CCI Soil Moisture Products Over the Yellow River Basin. IEEE J. Sel. Top. Appl. Earth Obs. Remote Sens.
Zhang, S., Gao, H., Naz, B.S., 2014. Monitoring reservoir storage in South Asia from multisatellite remote sensing. Water Resour. Res. 50, 8927–8943.
Zhang, Y., Pulliainen, J., Koponen, S., Hallikainen, M., 2002. Application of an empirical neural network to surface water quality estimation in the Gulf of Finland using combined optical data and microwave data. Remote Sens. Environ. 81, 327–336.
Zhang, Y., Pulliainen, J., Koponen, S., Hallikainen, M., 2003a. Empirical algorithms for Secchi disk depth using optical and microwave remote sensing data from the Gulf of Finland and the Archipelago Sea. Boreal Environ. Res. 8, 251–261.
Zhang, Y., Pulliainen, J.T., Koponen, S.S., Hallikainen, M.T., 2003b. Water quality retrievals from combined Landsat TM data and ERS-2 SAR data in the Gulf of Finland. IEEE Trans. Geosci. Remote Sens. 41, 622–629.
Zhao, D., Xing, X., Liu, Y., Yang, J., Wang, L., 2010. The relation of chlorophyll-a concentration with the reflectance peak near 700 nm in algae-dominated waters and sensitivity of fluorescence algorithms for detecting algal bloom. Int. J. Remote Sens. 31, 39–48.
Zhao, H., Ma, Y., 2019. Evaluating the Drought-Monitoring Utility of Four Satellite-Based Quantitative Precipitation Estimation Products at Global Scale. Remote Sensing 11, 2010.
Zhao, Q., Zhang, B., Yao, Y., Wu, W., Meng, G., Chen, Q., 2019. Geodetic and hydrological

measurements reveal the recent acceleration of groundwater depletion in North China Plain. J. Hydrol.
Zhou, Y., Dong, J., Xiao, X., Xiao, T., Yang, Z., Zhao, G., Zou, Z., Qin, Y., 2017. Open surface water mapping algorithms: a comparison of water-related spectral indices and sensors. Water 9, 256.
Zhu, W., Yu, Q., Tian, Y.Q., Chen, R.F., Gardner, G.B., 2011. Estimation of chromophoric dissolved organic matter in the Mississippi and Atchafalaya river plume regions using above-surface hyperspectral remote sensing. J. Geophys. Res.: Oceans 116, 116.
Zou, Z., Dong, J., Menarguez, M.A., Xiao, X., Qin, Y., Doughty, R.B., Hooker, K.V., Hambright, K.D., 2017. Continued decrease of open surface water body area in Oklahoma during 1984–2015. Sci. Total Environ. 595, 451–460.
Zuo, D., Cai, S., Xu, Z., Peng, D., Kan, G., Sun, W., Pang, B., Yang, H., 2019. Assessment of meteorological and agricultural droughts using in-situ observations and remote sensing data. Agric. Water Manag. 222, 125–138.